Dielectric and mechanical properties of polymers at macro and nanoscale

Clément Riedel

Université Montpellier 2

— Sciences et techniques du Languedoc —

Thesis

presented to obtain the grade of

Doctor of the Université Montpellier 2

Doctoral school and speciality: Information Système Structures, Electronique

also realized at the

Universidad del Pais Vasco / Euskal Herriko Unibertsitateko

Dielectric and mechanical properties of polymers at macro and nanoscale

by Clément Riedel

defended the 14 of October 2010, in front of a jury composed by :

President:	M. Gérard Lévêque	Professor	Université Montpellier 2
Referees :	M. Juan José Sáenz	Professor	Universidad Autónoma de Madrid
	M. Jean-Pierre Aimé	Professor	Université Bordeaux 1
Examinators :	M. Angel Alegría	Professor	Universidad del Pais Vasco
	M. Richard Arinero	Associate Prof.	Université Montpellier 2
	M. Nathan Israeloff	Associate Prof.	Northeastern University
Thesis directors :	M. Philippe Tordjeman	Professor	INP Toulouse
	M. Juan Colmenero	Professor	Universidad del Pais Vasco
Invited member:	M. Gustavo A. Schwartz	Researcher	Universidad del Pais Vasco

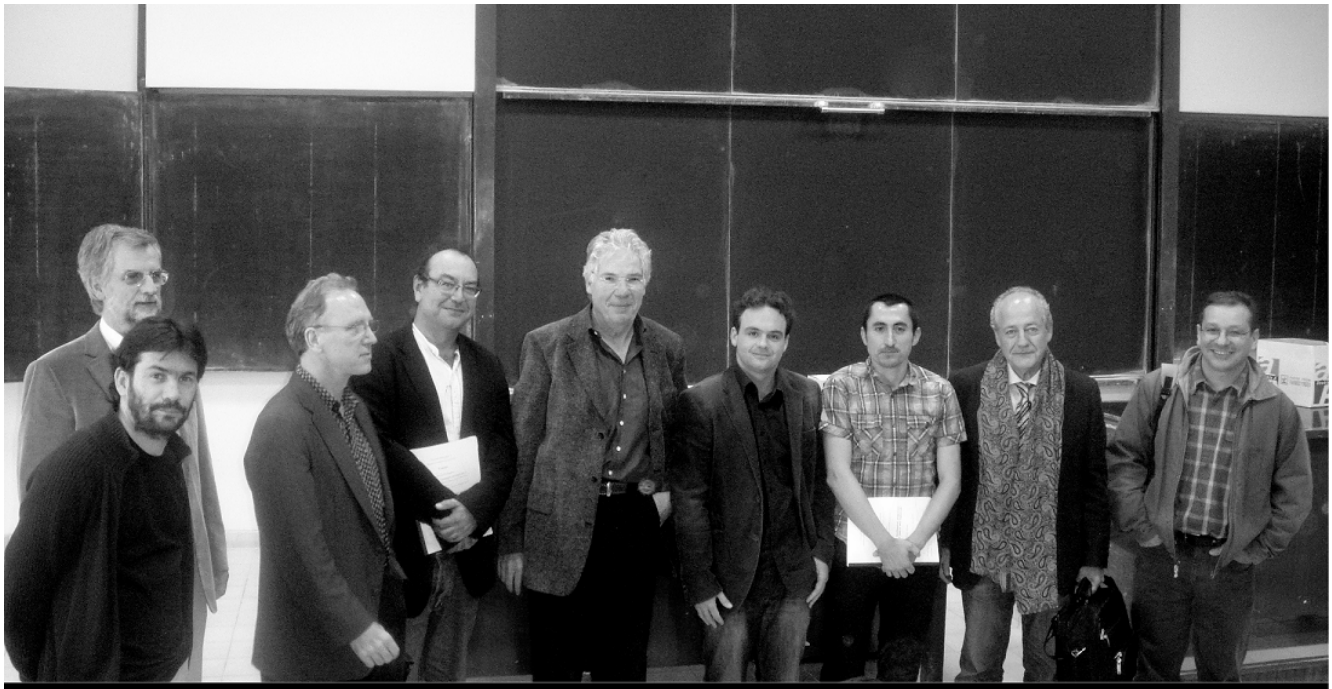

Montpellier, France, 14 of October 2010

"Science is like sex: sometimes something useful comes out, but that is not the reason we are doing it."

Richard P. Feynman. Joker, bongo player, Nobel prize winner

Acknowledgements

I realize that I have met a lot of interesting people during these last three years. Thanking them all nominatively would take a non reasonable time, and I am sure that they will know how to read between the lines. Therefore I will try to keep this section short.

Juan Colmenero de León, Philippe Tordjeman, Angel Alegría Loinaz, Richard Arinero, Nathan Israeloff, Gérard Lévêque, Gustavo Ariel Schwartz and Michel Ramonda are fully acknowledged (see Context section). I won't detail all their individual qualities but I would like to let them know that I am aware of the chance that I had to work with them. It has been a pleasure to wake up every day to meet them. Above raw scientific knowledge, they taught me how to conduct research and behave as a human being.

In the Institut d'Electronique du Sud, I have been working in the group MIRA created under the impulsion of Jacques Attal and directed by Gilles Despaux. I would like to thank them and all the researchers, students of this group for having received and supported me. In the Donostia International Physics Center I got a lot of help from all the people that I have met. First I would like to thank the secretaries: Ana López de Goicoechea, María del Mar Álvarez and Elixabete Mandizabal. They showed me that administrative tasks can be simple, fast and efficient. Dimas, Reidar, Luis, Lourdes and Silvia for all the advised and tips that helped me during my thesis. All the other students of this great laboratories (Dusan, Martin, Christine, Musthafa, Lourdes, Fabienne, Marco, Virginie, Daniele, Remi, Sandra, Sara...). The full financial support of the DIPC is acknowledged. In Northeastern University I worked in the best mood with Ryan Sweeney whom introduced me to its friends and family. All the people that I have met in Massachusetts and New England warmly opened me their harms and homes. Finally my past directors and master: Gilbert Moultaka, Eric Nuss Yves Gallant and Daniel Formichi are acknowledged.

To close this section, I would like to sincerely thank my parents (*pour l'intégralité de leur oeuvre*), my sister and Claire. Maxime, Bruno, Hugues, Le Mat, Garhed, Olivier, Flo, Amandine, Shova, Coralie, with whom I have been living during these last three years.

Context

A non averted reader may wonder why three Atomic Force Microscopes (AFM) have been used during this work. This thesis has been realized between three laboratories and it involves different researchers, experimental techniques and skills. I will summarize the research facilities used in each laboratory and the role of the persons that have participated to this work.

The thesis has first been defined by *Juan Colmenero de León* (Donostia International Physics Center [DIPC], San Sebastian-Donostia, Spain) and *Philippe Tordjeman* (Institut de Mecanique des Fluides de Toulouse [IMFT], France) as a bilateral partnership between the Institut d'Electronique du Sud (IES, Université Montpellier 2, France) and the DIPC. I think that their idea was to couple the knowledge in Electrostatic Force Microscopy (IES) and polymer science (DIPC) in order to develop new techniques to study the local dielectric dynamics of polymers. When they proposed me this thesis, we were not aware about the very recent contributions of Nathan Israeloff (Department of Physics of Northeastern University, Boston, MA, USA) to this field and this project seemed challenging. Results obtained during these three years are first due to their global vision and way to manage research and people.

In the DIPC, I had the chance to work with *Angel Alegría Loinaz*. We used Broadband Dielectric Spectroscopy and rheology (among the wide range of experimental techniques proposed by this laboratory) to study macroscopic properties of polymers. Results of the first chapter of this thesis have mainly been obtained in San Sebastian. I also would like to thanks *Gustavo Ariel Schwartz* for the implementation of EFM based methods in the Amplitude Modulation mode and measurements realized in the corresponding section of this manuscript.

In the IES, *Richard Arinero* showed me how to use an AFM and develop EFM based methods. He has been strongly involved in this thesis and helped me further than the scientific plan. *Gérard Lévêque* developed the numerical scripts based on the Equivalent Charge Method and taught me how to use and modify them.

Finally *Nathan Israeloff* received me for two months in Northeastern University. He has been the first to develop local dielectric spectroscopy methods under Ultra High Vacuum in the Frequency Modulation mode. Measurements in this mode (Chapter 5) have been realized in Northeastern University. He shared its knowledge without apprehension, and gave me a great freedom while working with *Ryan Sweeney*, an interested and interesting undergraduate student.

This work has been realized over a three year period starting September 2007. I have never stayed more than 5 consecutive months in one laboratory.

List of publications

[7] C. Riedel, R. Sweeney, N. E. Israeloff, R. Arinero, G. A. Schwartz, A. Alegria, Ph. Tordjeman and J. Colmenero: "Imaging dielectric relaxation in nanostructured polymers by frequency modulation electrostatic force microscopy" *Applied Physics Letters* **96**(21) p. 213110 (2010).

[6] C. Riedel, G. A. Schwartz, R. Arinero, Ph. Tordjeman, G. Lévêque, A. Alegria and J. Colmenero. "Nanoscale dielectric properties of insulating thin films: From single point measurements to quantitative images." *Ultramicroscopy* **110**(6): 634-638 (2010).

[5] C. Riedel, A. Alegria, Ph. Tordjeman and J. Colmenero: "High and low molecular weight crossovers in the longest relaxation time dependence of linear cis-1,4 polyisoprene by dielectric relaxations" *Rheologica Acta* **49**(5) p. 507-512 (2010).

[4] C. Riedel, R. Arinero, Ph. Tordjeman, G. Lévêque, G. A. Schwartz, A. Alegria and J. Colmenero: "Nanodielectric mapping of a model polystyrene-poly(vinyl acetate) blend by electrostatic force microscopy" *Physical Review E - Rapid communication* **81**(1) p. 010801 (2010).

[3] C. Riedel, R. Arinero, Ph. Tordjeman, M. Ramonda, G. Lévêque, G. A. Schwartz, D. G. de Oteyza, A. Alegria and J. Colmenero: "Dielectric properties of thin insulating layers measured by electrostatic force microscopy" *European Physical Journal Applied Physics* **50**(1) p. 10501 (2010).

[2] C. Riedel, R. Arinero, Ph. Tordjeman, M. Ramonda, G. Lévêque, G. A. Schwartz, D. G. d. Oteyza, A. Alegria and J. Colmenero: "Determination of the nanoscale dielectric constant by means of a double pass method using electrostatic force microscopy" *Journal of Applied Physics* **106**(2) p. 024315 (2009).

[1] C. Riedel, A. Alegria, Ph. Tordjeman and J. Colmenero: "Rouse-model-based description of the dielectric relaxation of nonentangled linear 1,4-cis-polyisoprene" *Macromolecules* **42**(21) p. 8492-8499 (2009).

Table of contents

Introduction

Why should physicists be interested in nanoscience?

because there's plenty of room at the bottom...

This famous talk given by Richard P. Feynman in 1959 (30 years before the invention of the Atomic Force Microscope [AFM] by Binnig *et al* [1]) clearly states about the importance of studying what happens at the nanoscale. One of the important point emphasized was the interdisciplinarity of nanoscience (Physics, Chemistry, Biology). It is particulary interesting to look at the questions asked by Prof. Feynman: "Why cannot we write the entire 24 volumes of the Encyclopaedia Britannica on the head of a pin? Is there a physical way to synthesize any chemical substance? What is the sequence of bases in the DNA and how proteins are synthesized? How is the structure of RNA related in its order of bases to the DNA?" This questions are interesting in the sense that answering them may get you a Nobel Prize. In 1962, Crick, Watson and Wilkins received one for their discoveries concerning the molecular structure of nucleic acids and its significance for information transfer in living material. In 1975, it has been awarded to Baltimore, Dulbecco, and Temin for the discovery of reverse transcriptase that permits to transcribes single-stranded RNA into double-stranded DNA.

It is interesting to note that the research of Watson and Crick are based on X-ray diffraction images of DNA obtained by Rosalind Franklin. Above the problem of intellectual property, this story is a good example of how a physical technique has been used to obtain a fundamental result in an other field. In this context, the AFM is remarkable because it permits to measure a wide range of properties in almost all nanoscience's field. Notably, it has been recently used to analyze the structure of Escherichia coli RNA polymerase [2] or to chemically identify [3] and manipulate [4] single atoms. At the end of its talk, Feynman, fully aware of the potentiality and the economic importance of nanoscience, finally conclude: "I know that the reason that you would do it might be just for fun." We will now focuss on the aim of this thesis: the study of dielectric and mechanical properties of polymers at macro and nanoscale.

Introduction

The title of this thesis: "Dielectric and mechanical properties of polymers at macro and nanoscale" is broad. The idea of this work was first to understand the main physical theories that describe the dynamics of linear polymers at the macroscopic scale using Broadband Dielectric Spectroscopy (BDS) and rheology. These techniques are commonly used to measure dielectric and mechanical properties, respectively. However, they have no spatial resolution and the study of the local dynamics or the dynamics of heterogeneous systems is always model dependent. Therefore, we would have liked to develop new methods to measure dielectric properties at the nanoscale in order to check how the local dynamics can be described by theories currently applied for macroscopic system.

The first chapter of this thesis is a general overview on polymers. We will define and detail what are polymers, their structures, types and conformations. Then we will introduce the Rouse model and reptational tube theory that describe the dynamics of non entangled and entangled polymers, respectively. Finally we will give the basis of thermodynamic polymer mixing.

In the second chapter, we will introduce the samples used all along in this work. We have chosen to study the dynamics of poly(vynil acetate) (PVAc) and polyisoprene (PI). PVAc exhibits a strong segmental relaxation (the so-called α-relaxation, $\Delta\epsilon \sim 5$) related with dipole moments perpendicular to the chain backbone slightly above room temperature. Therefore it is a convenient candidate to develop methods to measure dielectric properties at the nanoscale. PI has a weaker relaxation ($\Delta\epsilon \sim 0.05$, around 100 times weaker than the relaxation of PVAc), but due to dipolar moments parallel to the chain backbone, it also exhibits a whole chain dielectric relaxation (large scale dynamics). This so-called normal mode can either be described by the reptational tube theory or the Rouse model if the polymer is entangled or not. After having detailed the experimental techniques that permit to measure dielectric and mechanical properties at the macroscale, we will study these two relaxations and the two theories that describe the large scale dynamics [5, 6].

The third chapter is of the up most importance because it introduces notions needed to understand chapter 4 and 5. We have developed EFM based method to measure dielectric properties at the nanoscale . After having defined the electrostatic force and force gradient between an AFM tip and a dielectric sample, we will explain how these quantities can be measured using EFM. Then, we will detailed the numerical simulation of the Equivalent Charge Method (ECM) that permits to quantify the value of the relative dielectric constant ϵ_r from the quantities measured experimentally. The influence of each parameters of our system, the sensitivity of our experiment and the depth penetration of the electric field will also be discussed quantitatively [7]. Finally, we will reference in a non exhaustive way the different experimental methods found in literature to measure locally dielectric properties.

In chapter 4, we will describe how the static dielectric permittivity of a thin insulating film can be obtained at the nanoscale by measuring the force gradient created by a V_{DC} potential between a tip and a grounded dielectric. This method has first been developed to measure ϵ_r in one point before being extended to obtain quantitative maps the of the dielectric constant. Values of ϵ_r measured in one point will be presented for different systems (silicon dioxide, PVAc, and polystyrene (PS)) and we will detail how we have been able to quantitatively map the dielectric constant of a model nano-structured blend of PVAc in a matrix of PS [8, 9].

Finally, in chapter 5, we will present Local Dielectric Spectroscopy (LDS) that permits to measure the temperature-frequency dependence of the dielectric losses, related with the polymer dynamics. This method has first been developed under Ultra High Vacuum in the Frequency-Modulation (FM) mode by measuring the force gradient by Crider *et al* in 2007 [10, 11]. We will show how we have been able to extend this method in order to obtain a local mapping of the dielectric losses [12] appearing in the same kind of PVAc/PS thin film previously introduced. Then, we will demonstrate that LDS can be achieved in ambient condition, in the Amplitude-Modulation (AM) mode and by measuring the force of the interaction. The two methods based on the measurement of the force or force gradient will be compared based on first results. The timescale measured by LDS at the nanoscale will be compared to macroscopic ones measured by BDS. The influence of the parameters of the experiment will be discussed qualitatively.

Chapter 1

Overview on polymers

Summary

1 Introduction

"There is probably no other inert substance which so excites the mind." Charles Goodyear.

Much of human history has been influenced by the availability of materials. In fact, history is divided into eras named after the primary materials used; the Stone Age, the Bronze Age, and the Iron Age. Similarly, we can assert that we have entered the Polymer Age. Polymer have been first properly synthesized by Charles Goodyear using the process of vulcanization in the middle of the 19^{th} century. Today polymers are widely used in industry and quotidian life, well known examples include plastics, DNA and proteins.

A polymer is composed of molecules with large molecular mass, themselves constituted of repeating structural units (or monomers) connected by covalent chemical bonds. The word is derived from the Greek, poly, "many"; and meros, "part". Since 'monomer' can mean anything that repeats along the chain, it is by definition ambiguous. In this thesis, two types of monomers are important. Chemical monomers are the repeating unit that corresponds to the small molecules that were linked together to make the polymer chain. The Kuhn monomer involves a longer section of the chain (typically few chemical monomers) and will be defined and disused later. The entire structure of a polymer is generated during polymerization, the process by which chemical monomers are covalently bonded together. The number of monomers in a polymer molecule is called its degree of polymerization. The chemical identity of monomers is one of the main factors determining the properties of polymeric systems. Another major factor is the polymer's microstructure, which is the organization of atoms along the chain that is fixed during the polymerization process. Three process are mainly used to synthesize macromolecules: radical, anionic and cationic polymerization.

Macromolecules that contain monomers of only one type are called homopolymers. Homopolymers are made from the same monomer, but may differ by their microstructure, degree of polymerization or architecture. The degree of polymerization of macromolecules is a major factor determining many properties of polymeric systems. If a molecule consists of only a small number of monomers (generally, less than 20) it is called an oligomer. Linear polymers contain between 20 and 10 billion (for the longest known chromosome) monomers.

Combining several different types of monomers into a single chain leads to new macromolecules, called heteropolymers, with unique properties. The properties of heteropolymers depend both on composition (the fraction of each type of monomers present) and on the sequence in which these different monomers are combined into the chain. Macromolecules containing two different monomers are called copolymers. Copolymers can be alternating, random, block, or graft depending on the sequence in which their monomers are bonded together. Polymers containing two blocks are called diblock copolymers. Chains with three blocks are called triblock copolymers. Polymers with many alternating blocks are called multiblock copolymers. Many biopolymers are heteropolymers. DNA is a heteropolymer consisting of four different types of monomers (nucleotides), while natural proteins are heteropolymers commonly consisting of 20 different types of monomers (amino acids).

1.1 Isomerism

An example of double bond polymerization is shown in Fig. 1.1. A variety of different isomers are possible for the repeating units along the chain. Sequence isomerism are shown in

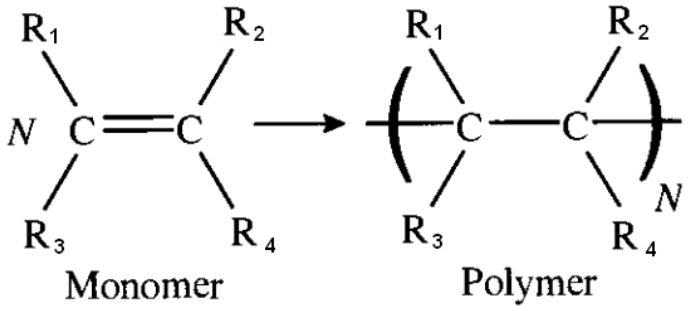

Figure 1.1 : *C-C double bond polymerization*

Fig. 1.2a for polypropylene. In the head-to-head isomer, two adjacent monomers have their CH_3 groups attached to adjacent carbons along the chain's backbone, whereas the head-to-tail isomer has a CH_2 in the backbone between the CH_3 groups of adjacent monomers. Head-to-tail is the more common microstructure, but the properties change significantly with the fraction of head-to-head isomers present. Polymers that contain a double bond in their backbone (that cannot rotate) can exhibit structural isomerism. Such polymers have distinct structural isomers, such as cis-, trans-, and vinyl-polybutadiene shown in Fig. 1.2b. These isomers result from the different ways that dienes, such as butadiene, can polymerize and many synthetic polymers have mixtures of cis and trans structural isomers along their chains.

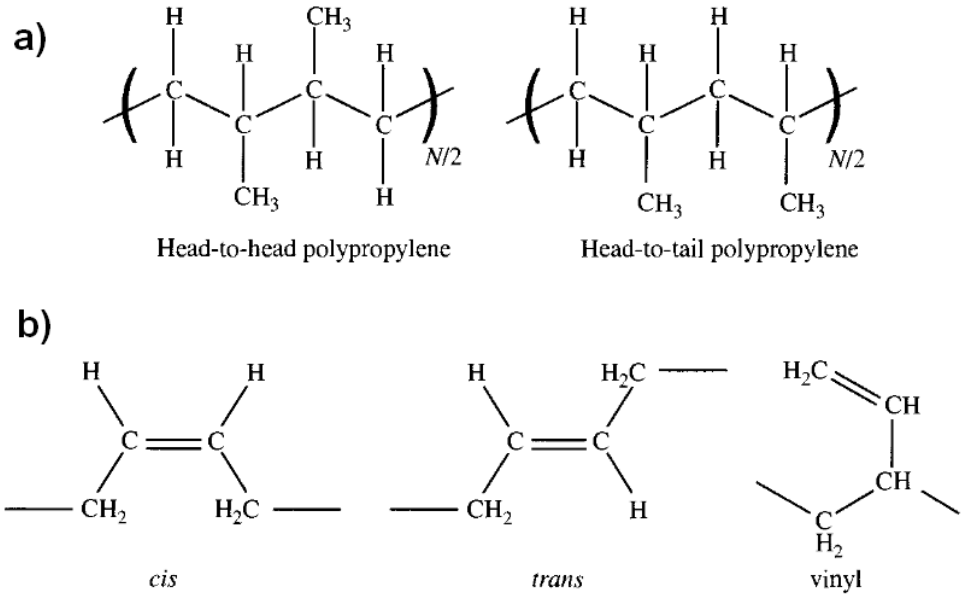

Figure 1.2 : *Sequential and structural isomers [13]*

Another isomeric variation that is locked-in during polymerization is stereoisomerism. The four single bonds, emanating from a carbon atom, have a tetragonal structure. The place-

ment of the different group on this tetragonal structure leads to different tacticity (isotactic, syndiotactic, atactic).

1.2 Architecture

Architecture is an important feature controlling the properties of polymeric systems. Types of polymer architectures include linear, ring, star-branched, H-branched, comb, ladder, dendrimer, or randomly branched as sketched in Fig. 1.3. Random branching that leads to structures like

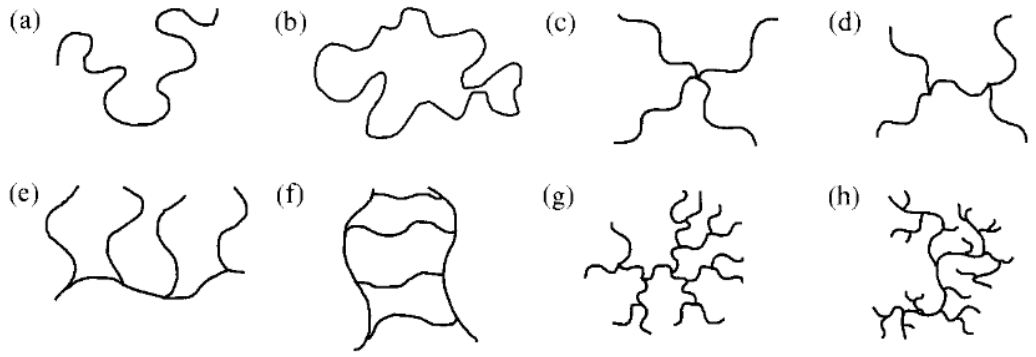

Figure 1.3 : *Examples of polymer architectures: (a) linear; (b) ring; (c) star; (d) H; (e) comb: (f) ladder; (g) dendrimer; (h) randomly branched. [13]*

Fig. 1.3h has particular industrial importance, for example in bottles and film for packaging. A high degree of crosslinking can lead to a macroscopic molecule, called a polymer network.

1.3 Types of polymeric substances

— **Polymer liquid**

There are two types of polymer liquids: polymer melts and polymer solutions. Polymer solutions can be obtained by dissolving a polymer in a solvent. Examples of polymer solutions are wood protectants (varnish and polyurethane coatings) and floor shines. Polymer solutions are classified as dilute or semidilute depending on the polymer mass concentration, the ratio of the total mass of polymer dissolved in a solution and the volume of the solution. In the absence of solvent, macromolecules can form a bulk liquid state, called a polymer melt. Polymer melts are neat polymeric liquids above their glass transition and melting temperatures. A macroscopic piece of a polymer melt remembers its shape and has elasticity on short time scales, but exhibits liquid flow (with a high viscosity) at long times. Such time dependent mechanical properties are termed viscoelastic because of the combination of viscous flow at long times and elastic response at short times. A familiar example of a polymer melt is Silly Putty®. On short time scales (of order seconds), a sphere of Silly Putty resembles a soft elastic solid that bounces when dropped on the floor. However, if left on a table top for an hour, Silly Putty flows into a puddle like a liquid.

— **Polymer solid**

There are several different types of polymeric solids. If a polymer melt is cooled, it can either transform into a semicrystalline solid below its melting temperature T_m or into a polymeric glass below its glass transition temperature T_g. Semicrystalline solids consist of crystalline regions, called lamellae, in which sections of chains are packed parallel to each other, and of amorphous regions between these lamellae. This multiphase nature makes semicrystalline polymers opaque,

but also deformable and tough, when used at temperatures above the T_g of the amorphous phase (such as for polyethylene and polypropylene at room temperature). Macromolecules with regular configurations, such as isotactic and syn- diotactic homopolymers often crystallize easily. Macromolecules with more random configurations, such as atactic homopolymers and random copolymers, tend to transform upon cooling into a transparent yet brittle glassy state (such as polymethylmethacrylate and polystyrene). However, there are technologically important exceptions to this rule. Polycarbonate, for example, is a tough glassy polymer at room temperature, making it the polymer of choice for transparent structural applications such as greenhouses and skylights. If the chains of a polymer melt are reacted with each other to form covalent crosslinks between chains, a polymer network can be formed. Polymer networks are solids and have a preferred shape determined during their preparation by crosslinking. Above their T_g, the chains between crosslinks in a polymer network can move locally, but not globally. Therefore, polymer networks above T_g are called soft solids. Rubbers or elastomers are crosslinked polymer networks with T_g below room temperature. Examples are vulcanized natural rubber (crosslinked polyisoprene) and silicone caulks (crosslinked polydimethylsiloxane). A polymer gel is a polymer network that is swollen in a solvent. The gel becomes progressively softer as more solvent is added, but always remains a solid owing to the permanent bonds that connect the chains. Examples of common polymer gels are Jello®, which is a mixture of water and gelatin (a denatured form of the protein collagen collagen), and superabsorbers derived from poly (acrylic acid) used in disposable diapers.

— Liquid Crystal

A variety of states with order intermediate between crystalline solids and amorphous liquids are also possible for polymers that contain sufficiently rigid rodlike monomers, known as mesogens. These mesogens can be attached to chemical monomers as a side group or they may be incorporated within the backbone of the polymer. Polymers with exclusively rigid rod-like mesogens as their monomers are usually intractable because they start to decompose below their crystalline melting points. However, alternating copolymers of rigid rodlike mesogens and flexible segments often are able to be melt processed and have interesting properties. In particular, in a temperature range between their melting point and the temperature at which they become isotropic liquids, these polymers can exhibit any of a number of phases with intermediate order.

A nematic phase, where the mesogens preferentially align in the same direction locally, is the least ordered and most common liquid crystalline phase. Often the alignment of the mesogens allows the molecules to slide past one another more easily, making the viscosity of the nematic phase lower than the isotropic liquid viscosity. A variety of smectic phases are also possible, where the mesogens form layered structures. These anisotropic liquid crystalline phases can occur in melts, solutions and networks. The physical properties of liquid crystal polymers are anisotropic as a result of the order. Additionally, electric fields, magnetic fields, and flow fields can be used to align this class of materials.

1.4 Molecular mass distribution

One distinguishing feature of most synthetic polymers is that they are polydisperse. The entire polymer sample is made up of individual molecules that have a distribution of degrees of polymerization, determined by the particular synthesis method used. If all polymers in a given sample have the same number of monomers, the sample is monodisperse. There are many examples of natural polymers (such as proteins) that are perfectly monodisperse, but such perfection is very rare in synthetic polymers. The polydispersity of a sample is described by its molecular mass distribution. Given a distribution of molecular sizes (N_i molecules of mass

M_i), the number-averaged molecular weight M_n is defined as the first moment of distribution (Eq. 1.1) and the mass-averaged molecular weight M_w as the ratio between the second and first moments of the distribution (Eq. 1.2).

$$M_n = \sum_i \frac{N_i M_i}{N_i} \tag{1.1}$$

$$M_w = \sum_i \frac{N_i M_i^2}{N_i M_i} \tag{1.2}$$

The polydispersity I_p is the ratio M_w/M_n .

1.5 Static conformation of an ideal chain

We consider the conformations of an ideal chains with no interactions between monomers that are far apart along the chain, even if they approach each other in space. This model is an essential starting point in most models in polymer physics. In order to understand the multitude of conformations available for a polymer chain, consider an example of a polyethylene molecule. The distance between carbon atoms in the molecule is almost constant l = 1.54 Å. The fluctuations in the bond length (typically ± 0.05 Å) do not affect chain conformations. The angle between neighbouring bonds, called the tetra- hedral angle $\theta = 68°$ is also almost constant. The main source of polymer flexibility is the variation of torsion angles (see Fig. 1.4a). In order to describe these variations, consider a plane defined by three neighbouring carbon atoms C_{i-2}, C_{i-1}, C_i. The bond vector $\overrightarrow{C_{i-1}C_i}$ defines the axis of rotation for the bond vector $\overrightarrow{C_iC_{i+1}}$ at constant bond angle θ_i. The zero value of the torsion angle ϕ_i corresponds to the bond vector $\overrightarrow{C_iC_{i+1}}$ being colinear to the bond vector $\overrightarrow{C_{i-2}C_{i-1}}$ and is called the trans state (t) of the torsion angle ϕ_i (Fig. 1.4b). The trans state of the torsion angle ϕ_i is the lowest energy conformation

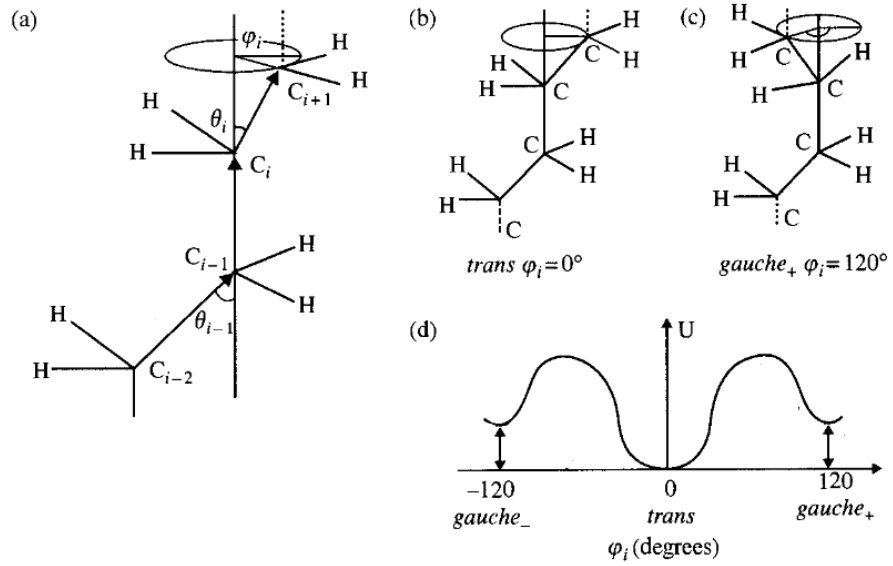

Figure 1.4 : *(a) Torsion angle ϕ_i for a sequence of three main-chain bonds, (b) Trans state, (c) Gauche-p]us state, (d) Torsion angle dependence of energy. [13]*

of the four consecutive CH_2 groups. The changes of the torsion angle ϕ_i lead to the energy variations shown in Fig. Fig. 1.4d. These energy variations are due to changes in distances and therefore interactions between carbon atoms and hydrogen atoms of this sequence of four CH_2

groups. The two secondary minima corresponding to torsion angles ϕ_i, $= \pm 120°$ are called gauche plus (g+) and gauche minus (g-) (Fig. 1.4c). The energy difference between gauche and trans minima determines the relative probability of a torsion angle being in a gauche state in thermal equilibrium.

Any section of the chain with consecutive trans states of torsion angles is in a rod-like zig-zag conformation. If all torsion angles of the whole chain are in the trans state, the chain has the largest possible value of its end-to-end distance R_{Max}. This largest end-to-end distance is determined by the product of the number of chemical skeleton bonds n and their projected length along the contour, and is referred to as the contour length of the chain:

$$R_{Max} = nl \cos\left(\frac{\theta}{2}\right) \tag{1.3}$$

A qualitatively different mechanism of flexibility of many polymers, such as double-helix DNA is uniform flexibility over the whole polymer length. These chains are well described by the so-called worm-like chain model.

— **The random walk**

The random walk is an extremely simple model that accounts quantitatively for many properties of chains and provides the starting point for much of the physics of polymer (see the Rouse model below). In this model, we consider an ideal freely joined chain, made up of N links, each define by a vector $\overrightarrow{r}_i$ and b the average length between the links (Fig. 1.5). The different links have independent orientations. Thus the path of the polymer in space is a random walk. It is important to note that the bond here considered, the so-called Kunh monomers, are different from the chemical bond defined previously.

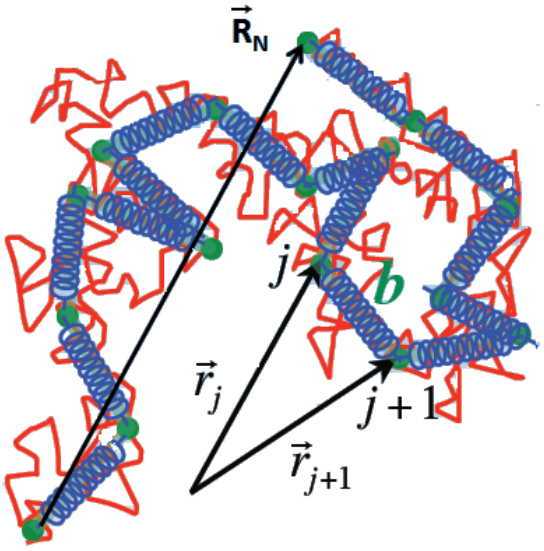

Figure 1.5 : *Schematic representation of the spring model for polymer chain*

The end-to-end vector $\overrightarrow{R}_N(t)$ is the sum of the N jump vectors $\overrightarrow{r}_{i+1} - \overrightarrow{r}_i$ which represent the direction and size of each link in the chain:

$$\overrightarrow{R}_N(t) = \sum_{i=1}^{N-1} \overrightarrow{r}_{i+1} - \overrightarrow{r}_i \tag{1.4}$$

The mean end-to-end distance is

$$\langle \overrightarrow{R}_N(t) \cdot \overrightarrow{R}_N(t) \rangle = \langle \sum_{i=1}^{N-1} (\overrightarrow{r}_{i+1} - \overrightarrow{r}_i) \cdot (\sum_{i=1}^{N} \overrightarrow{r}_{i+1} - \overrightarrow{r}_i) \rangle \tag{1.5}$$

$$\langle \overrightarrow{R}_N(t)^2 \rangle = \langle \sum_i \sum_j (\overrightarrow{r}_{i+1} - \overrightarrow{r}_i) \cdot (\overrightarrow{r}_{j+1} - \overrightarrow{r}_j) \rangle \tag{1.6}$$

If we extract from the sum the case $i = j$

$$\langle \overrightarrow{R}_N(t)^2 \rangle = N\, b^2 + \langle \sum_{i \neq j} (\overrightarrow{r}_{i+1} - \overrightarrow{r}_i) \cdot (\overrightarrow{r}_{j+1} - \overrightarrow{j}_i) \rangle \tag{1.7}$$

As the chain is freely joined, the directions of different links are completely uncorrelated and the cross term disappear when the average is taken. We obtain the random walk result :

$$\langle \overrightarrow{R}_N(t)^2 \rangle = N\, b^2 \tag{1.8}$$

The contour length of this equivalent freely jointed chain is simply:

$$R_{Max} = Nb \tag{1.9}$$

It is interesting to note that the Kunh length can be related with the number and size of chemical monomers (n and l respectively) using the Flory's Characteristic ratio C_n. This coefficient is the average value of the sum of the angle between all vectors ($\theta_{i,j}$):

$$C_n = \frac{1}{n} \sum_{i=1}^{n} \sum_{j=1}^{n} \langle \cos(\theta_{i,j}) \rangle \tag{1.10}$$

The physical origins of these local correlations between bond vectors are restricted bond angles and steric hindrance. All models of ideal polymers ignore steric hindrance between monomers separated by many bonds and result in characteristic ratios saturating at a finite value C_∞ for large numbers of main-chain bonds (n $\rightarrow \infty$). Thus, thinking in terms of chemical monomers, the mean- square end-to-end distance can be approximated for long chains:

$$\langle \overrightarrow{R}_N(t)^2 \rangle = C_\infty n l^2 \tag{1.11}$$

and the relation between the Kunh and chemical monomer size is given by:

$$b = \frac{\langle \overrightarrow{R}_N(t)^2 \rangle}{R_{Max}} = \frac{C_\infty n l^2}{R_{Max}} \tag{1.12}$$

2 Polymer dynamics

2.1 Overview on polymer dynamics

Before detailing the models describing the dynamics, it is interesting to have a global point-of-view on all different regimes followed by a modulus (describing a property) and their molecular origin. The Fig. 1.6 describes schematically the variation of the elastic part of the young modulus (related with the elasticity of the polymer) as a function of temperature for a given frequency. We will see that the same kind of plot can be obtained as a function of the

time for a given temperature. As it is well explained in reference [14]:

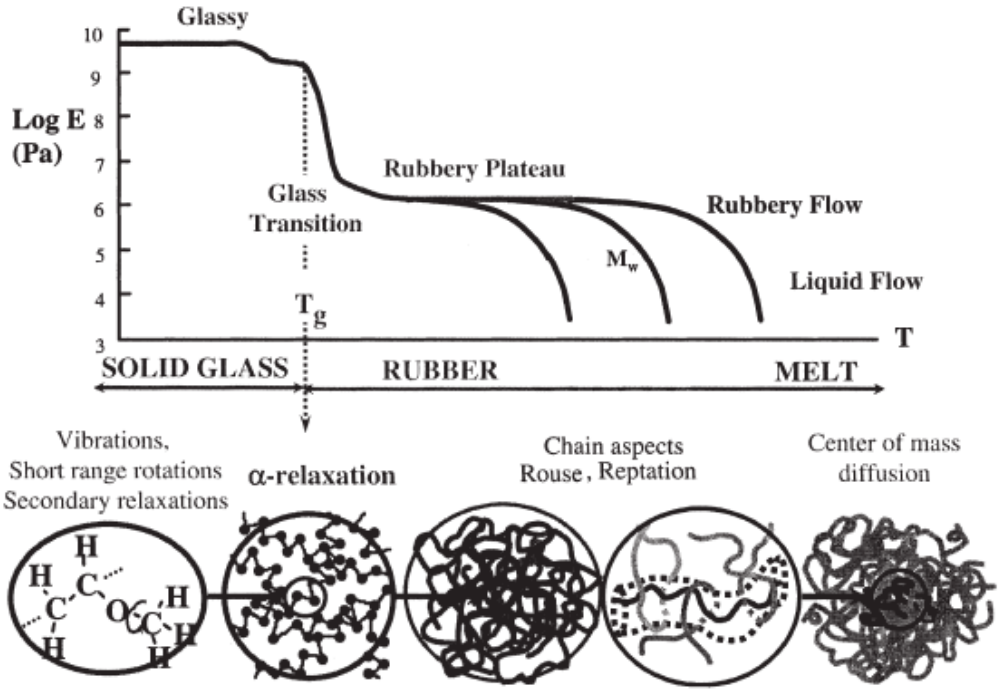

Figure 1.6 : *Richness of dynamic modulus in a bulk polymer and its molecular origin. [14]*

At low temperature (or short time) the material is in the glassy state and only small amplitude motions like vibrations, short range rotations or secondary relaxations are possible. Below the glass transition temperature T_g the secondary β-relaxation and the methyl group rotations may be observed. In addition, at high frequencies the vibrational dynamics, in particular the so called Boson peak, characterizes the dynamic behavior of amorphous polyisoprene. The secondary relaxations cause the first small step in the dynamic modulus of such a polymer system.

At the glass transition temperature T_g the primary relaxation (α-relaxation), related to segmental motion of the chain, becomes active allowing the system to flow. In the dynamic modulus, the α-relaxation causes a huge step of typically three orders of magnitude in strength.

The following rubbery plateau in the modulus relates to large scale motions within a polymer chain. Two aspects stand out. When the sample has a molecular weight below the molecular weight of entanglement, relaxations of fluctuations out of equilibrium are entropy-driven and qualitatively described by the Rouse model and no plateau is detected since no transient network are formed. Secondly, for samples having a molecular weight superior to the molecular weight of entanglement, these relaxations are limited by confinement effects caused by the mutually interpenetrating chains. This confinement is modeled most successfully in terms of the reptation model by de Gennes [15] and Doi and Edwards [16]. There, the confinement effects are described in terms of a tube following the coarse grained chain profile. The final diffusive motion is only allowed along the tube profile leading to the reptation process the snake-like motion of a polymer chain.

When a chain has lost the memory of its initial state, rubbery flow sets in. Then we enter into the liquid flow, which is characterized by the translational diffusion coefficient of the chain. Depending on the molecular weight, the characteristic length scales from the motion of a single bond to the overall chain diffusion may cover about three orders of magnitude,while the associated time scales easily may be stretched over ten or more orders.

2.2 Rouse model

The Rouse model is based on the static conformation of an ideal chain described by a random walk (see above). The overall size of a random walk is proportional to the square root of the number of steps. The distribution of possible end-to-end vectors is well known in statical mechanics to be gaussian. Specifically, the probability distribution function $P(\overrightarrow{R}, N)$ is given by:

$$P(\overrightarrow{R}_N(t), N) = \left(\frac{3}{2\,\pi\,b^2}\right)^{3/2} \exp\left(-\frac{3\,\overrightarrow{R}_N^2}{2\,N\,b^2}\right) \tag{1.13}$$

This expression is important because it allows us to reach the configurational entropy $S(\overrightarrow{R}_N)$ of a polymer chain as a function of its elongation (k_b is the Boltzman constant):

$$S(\overrightarrow{R}_N) = -\frac{3\,k_b\,\overrightarrow{R}_N^2}{2\,b^2} \tag{1.14}$$

Thus, when we stretch a polymer chain its entropy is lowered. This results in an increase in the free energy $\Delta F(\overrightarrow{R}_N)$ (T is the temperature and as the chain is freely joined, there is no interactions and the potential energy U is negligible):

$$\Delta F(\overrightarrow{R}_N) = \frac{3\,k_b\,T\,\overrightarrow{R}_N^2}{2\,b^2} \tag{1.15}$$

And so we can calculate the spring like force:

$$\overrightarrow{F}^S = \frac{3\,k_b\,T\,\overrightarrow{R}_N}{b^2} \tag{1.16}$$

A polymer chain behave like a mass spring system; if it is stretched beyond its ideal random walk value there is a restoring force proportional to the extension. However, this restoring force does not arise from an increase of internal energy of the polymer as it would for the spring. Instead the origin of the force is entirely entopic. There are fewer possible configurations of the polymer chain when it stretched than when it is in its unperturbed random walk state.

The force of all the other chains can be represented by introducing a friction coefficient ξ. As this parameter describe short range interactions it is somehow related with the α-relaxation.

$$\overrightarrow{F}^F = -\xi\frac{d\,\overrightarrow{r}}{dt} \tag{1.17}$$

Finally, the random forces $\overrightarrow{f}$, that represents the sum of the forces due to the interaction of the molecules with Brownian particles, are defined as:

$$\langle\,\overrightarrow{f}\,(t)\rangle = 0 \tag{1.18}$$

$$\langle\,\overrightarrow{f}_i(t)\,\overrightarrow{f}_j(t')\rangle = 2\,\xi\;k_b\;T\,\delta_{ij}\,\delta(t-t') \tag{1.19}$$

As you can see on Eq. 1.19 there is no (either spatial or time) correlation between random forces.

Once we have introduced all the static properties we can develop the Rouse model in order to get the equation of movement. This model has first been thought for polymers in solution in a theta solvent [17] and does not take into account:
1: Rapid relaxation process involving segments shorter than the submolecule (α-relaxation).
2: Obstruction of the motion of a segment by other segments with which it could be in contact.

This implies that the Rouse theory only works for molecular weight under the entanglement molecular weight M_e which correspond to the average mass between to chains crossover.

Let's now apply the fundamental principle of dynamics for one mass between two springs: (Fig. 1.7):

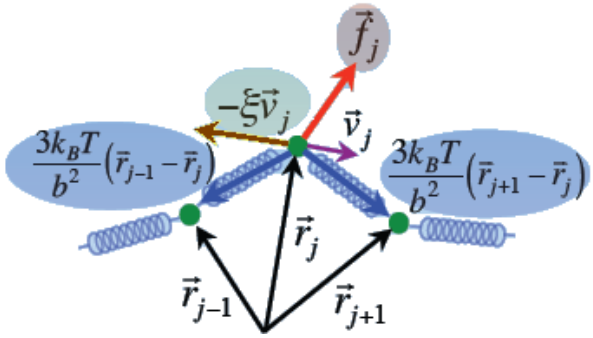

Figure 1.7 : *Schematic representation of the forces in the Rouse model*

$$m\frac{d^2\overrightarrow{r}_j}{dt^2} = \overrightarrow{F}_j^S + \overrightarrow{F}_j^F + \overrightarrow{f}_j \tag{1.20}$$

$$\overrightarrow{F}_j^S = \frac{3\,k_bT}{b^2}(\overrightarrow{r}_{j+1} + \overrightarrow{r}_{j-1} - 2\,\overrightarrow{r}_j) \qquad for\ j \neq 1, N \tag{1.21}$$

$$\overrightarrow{F}_j^F = -\xi\frac{d\overrightarrow{r}_j}{dt} \tag{1.22}$$

As experimental results shown that the inertial term $m\frac{d^2\overrightarrow{r}_j}{dt^2}$ is negligible for $t \gg m/\xi \sim 10^{-12}s$ we obtain the equation of the Brownian motion of coupled oscillators:

$$\xi\frac{d\overrightarrow{r}_j}{dt} = \frac{3\,k_bT}{b^2}(\overrightarrow{r}_{j+1} + \overrightarrow{r}_{j-1} - 2\,\overrightarrow{r}_j) + \overrightarrow{f}_j \tag{1.23}$$

This set of equations is coupled. To solve this system, we need to use normal coordinate (Rouse modes) to get independent equations of motion. A complete derivation of the normal modes coordinate in the continuous limit, for long chains, is given in ref [16]. Here as we are working with small chains, we will follow the approach of reference [18] :

$$\overrightarrow{X}_p(t) = \frac{1}{N}\sum_{j=1}^{N} A_{pj}\overrightarrow{r}_j(t) \qquad p = 0, 1, ..., N-1 \tag{1.24}$$

where

$$A_{pj} = cos\left(\frac{p\,\pi}{N}(j - \frac{1}{2})\right) \tag{1.25}$$

$\overrightarrow{X}_p(t)$ describes the motion of a subchain of "wavelength" $\simeq \frac{N}{P}$ and lentgth-scale $\simeq \sqrt{\frac{N\,b^2}{p}}$. The inverse transformation of Eq. 1.24 gives:

$$\overrightarrow{r}_j(t) = \overrightarrow{X}_0(t) + 2\sum_{p=1}^{N-1} A_{pj}\,\overrightarrow{X}_p(t) \tag{1.26}$$

where $\overrightarrow{X}_0(t) = \frac{1}{N}\sum \overrightarrow{r}_j(t)$ is the center of mass of the chain.

The equation 1.23 can be written with the Rouse modes as a set of independent equations:

$$\xi_p \frac{d\,\overrightarrow{X}_p(t)}{dt} = -\frac{12 k_b T \xi_p}{b^2} sin\left(\frac{p\,\pi}{2\,N}\right)^2 \overrightarrow{X}_p(t) + \overrightarrow{g}_p \tag{1.27}$$

with:

$$\xi_p = (2-\delta_{op})\,N\,\xi \tag{1.28}$$

$$\overrightarrow{g}_p = \frac{\xi_p}{N\,\xi}\sum_{j=1}^{N} A_{pj}\,\overrightarrow{f}_i(t) \tag{1.29}$$

Within the Rouse model, according to Eq. 1.27, the Rouse modes are mutually orthogonal and the correlation functions for p > 0 are exponentially decaying:

$$\langle \overrightarrow{X}_p(t)\overrightarrow{X}_{p(0)}\rangle = \langle X_p^2\rangle \exp\left(\frac{-t}{\tau_p}\right) \tag{1.30}$$

with the distribution of the relaxation times

$$\tau_p = \frac{\xi b^2}{12\,k_b\,T\,sin^2\left(\frac{p\,\pi}{2N}\right)} \tag{1.31}$$

for p$\pi \ll$2N, and as $N \propto M_w$

$$\tau_p \cong \frac{\xi b^2}{3\,k_b\,T\,(\pi p)^2} N^2 \tag{1.32}$$

$$\tau_p \propto {M_w}^2 \tag{1.33}$$

The slowest time τ_1 is called the Rouse time

$$\tau_1 = \tau_p/p^2 = \frac{\xi b^2}{3\,k_b\,T\pi^2} N^2 \tag{1.34}$$

The Rouse characteristic frequency is defined as:

$$W = 3k_bT/(\xi b^2) \tag{1.35}$$

The amplitude of the Rouse modes can be calculated from Eq. 1.27 [18]

$$\langle X_p^2\rangle = \frac{b^2}{8N sin^2\left(\frac{p\,\pi}{2N}\right)} \tag{1.36}$$

Finally we can calculate the dynamic of the end-to-end vector $\overrightarrow{R}_N(t) = \overrightarrow{r}_N(t) - \overrightarrow{r}_1(t)$:

$$\overrightarrow{R}_N(t) = 2\sum_{p:1}^{N-1} \overrightarrow{X}_p(t) cos\left(\frac{p\pi}{2N}\right)(cos(p\pi) - 1) \tag{1.37}$$

$$= -4\sum_{p:odd}^{N-1} \overrightarrow{X}_p(t) cos\left(\frac{p\pi}{2N}\right) \tag{1.38}$$

and the correlation function of $\overrightarrow{R}_N(t)$

$$\langle \overrightarrow{R}_N(t)\overrightarrow{R}_N(0)\rangle = 16\sum_{p:odd}^{N-1} \langle X_p^2\rangle cos^2\left(\frac{p\pi}{2N}\right)\exp\left(\frac{-t}{\tau_p}\right) \tag{1.39}$$

$$= \frac{2b^2}{N}\sum_{p:odd}^{N-1} cot^2\left(\frac{p\pi}{2N}\right)\exp\left(\frac{-t}{\tau_p}\right) \tag{1.40}$$

In the limit of the long chains, for pπ<2N, we obtain the well known expression of the end-to-end vector:

$$\langle \overrightarrow{R}_N(t)\overrightarrow{R}_N(0)\rangle \cong \frac{8\,b^2N}{\pi^2}\sum_{p:odd}\frac{1}{p^2}\exp\left(-\frac{t}{\tau_p}\right) \tag{1.41}$$

Due to the factor $1/p^2$ the correlation function of the end-to-end vector is dominated by the Rouse time (slowest mode) and as $\tau_p = \frac{\tau_1}{p^2}$ the higher modes are shifted to higher frequencies.

For small deformation, the chain can be approximatively described using a gaussian configuration and the expression of the xy component of the microscopic shear stress is given by [16]:

$$\sigma_{xy} = \frac{3\,\nu\,k_bT}{Nb^2}\sum_{i=1}^{N}\langle(\overrightarrow{r}_{i+1} - \overrightarrow{r}_i)_x(\overrightarrow{r}_{i+1} - \overrightarrow{r}_i)_y\rangle \tag{1.42}$$

where ν is the number of chain per volume unit V. This expression can be written in term of normal coordinates [18]:

$$\sigma_{xy}(t) = \frac{3\,k_bT}{V}\sum_{i=1}^{N}\frac{X_{i,x}(t)X_{i,y}(t)}{\langle X_i^2\rangle} \tag{1.43}$$

In the next chapter, the Rouse model will be invesigated by Broadband Dielectric Spectroscopy (BDS) and rheology. Therefore it is important to obtain the expressions of the dielectric permittivity $\underline{\epsilon}(\omega)$ and shear modulus $\underline{G}(\omega)$ in the frame of this model.

— Expression of $\underline{\epsilon}(\omega)$ in the frame of the Rouse Model

BDS measure the time fluctuation of the polarization. Polymers can have dipole moments parallel to the chain backbone, leading to a net "end-to-end" vector. The part of the polarization related with these dipole moments is proportional to the time fluctuation of the end-to-end vector: $\phi(t) = [\overrightarrow{P}(t)\cdot\overrightarrow{P}(0)] \propto [\overrightarrow{R_N}(t)\cdot\overrightarrow{R_N}(0)]$. Using the expression of the end-to-end vector (Eq. 1.40) in the phenomenological theory of the dielectric relaxation (Eq. 2.6) we obtain an expression of the frequency dependance of the dielectric permittivity in the frame of the Rouse model:

$$\epsilon'(\omega) \propto \frac{2b^2}{N}\sum_{p:odd}^{N-1} cot^2\left(\frac{p\pi}{2N}\right)\frac{1}{1+\omega^2\tau_p^2} \tag{1.44}$$

$$\epsilon''(\omega) \propto \frac{2b^2}{N}\sum_{p:odd}^{N-1} cot^2\left(\frac{p\pi}{2N}\right)\frac{\omega\tau_p}{1+\omega^2\tau_p^2} \tag{1.45}$$

Only the odds (step from equation 1.37 to 1.38 contribute to the dielectric permittivity. Moreover, the factor $cot^2(p)$ (which can be developed in $1/p^2$ when p<N) strongly suppress the contribution of high p modes. Therefore, the dielectric permittivity is sensitive to slow (low p modes) and facilitates resolving normal mode and segmental relaxation contributions.

— **Expression of $\underline{G}(\omega)$ in the frame of the Rouse Model**

We can calculate the expression of the shear modulus in the time domain from Eq.1.43, and using a Fourier transform, we obtain:

$$G'(\omega) \propto \sum_{p=1}^{N-1}\frac{\omega^2\tau_p^2/4}{1+\omega^2\tau_p^2/4} \tag{1.46}$$

$$G''(\omega) \propto \sum_{p=1}^{N-1}\frac{\omega\tau_p/2}{1+\omega^2\tau_p^2/4} \tag{1.47}$$

All the modes are contributing in the expression of the shear modulus. Therefore, for the case of small chains, rheology is not a convenient experimental technique to resolve the chain modes from the segmental dynamics.

2.3 Reptational tube model

The reptational tube model was first introduced by de Gennes [15] and developed by Doi and Edwards [16] to described the phenomena of entanglement. This model is valid when the molecular weight of the sample is superior to the molecular weight of entanglement M_e. Many corrections (as Contour Length Fluctuation or Constraints Release) have been added to the pure reptation in order to reach a totally predictive theory [19, 20].

In the reptational tube model, an entangled chain diffuses along its confining tube in a way analogous to the motion of a snake or a worm. This notion of the chain consists of diffusion of small loops, along the contour of the primitive path. The lateral restrictions are modelled by a tube with a diameter d parallel to the chain profile.

For short times,when the chain segment has not yet realized the topological constraints, i.e. for distances smaller than the tube diameter ($r < d$), we expect unrestricted Rouse motion. The corresponding relaxation time τ_e, is defined as [16] :

$$\tau_e = \frac{\xi d^4}{k_b T b^2} \tag{1.48}$$

where b is the Kunh length previously defined. Another important relaxation time is the disanglement time τ_d which correspond to the time needed for the primitive chain to disengage from the tube it was confined to [16].

$$\tau_d = \frac{\xi b^4 N^3}{\pi k_b T d^2} \tag{1.49}$$

When $\tau_e < t < \tau_d$ the chain reptates along the tube. This phenomena can be visualized as a non-interacting defect running along like the arch in a caterpillar (see Fig. 1.8a). As a result of such motion, the tube itself changes with time (Fig. 1.8b): for example if the chain moves right, the part B_0B can choose a random direction, and create a new part of the tube which will be a constraint for the rest of the chain, while the part of the previous tube A_0A becomes empty and disappears.

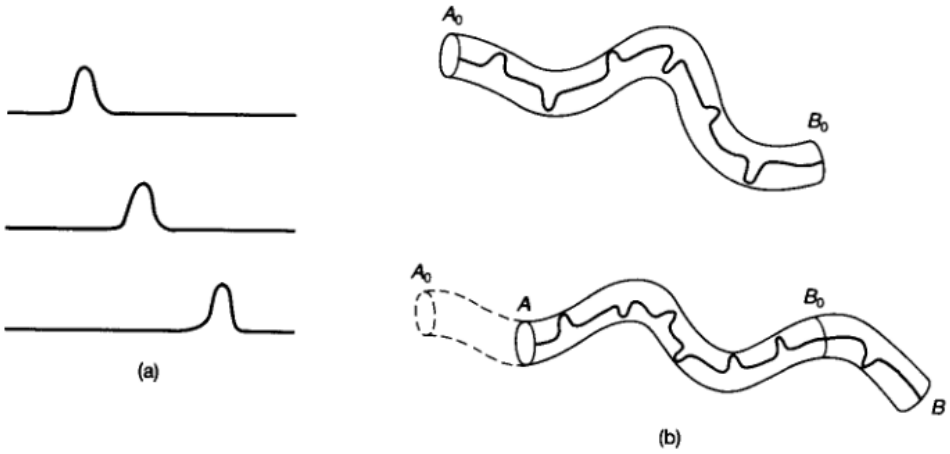

Figure 1.8 : *Schematic representation of reptation: (a) Motion of a single defect (b) Motion of the tube. [16].*

2.4 Segmental dynamics and glass transition temperature

Polymeric solids can be found the amorphous state or in the partially crystalline state. The glass transition is "*probably the deepest and most interesting unsolved problem in solid state theory*", in the words of the Nobel Prize winner P.W. Anderson. The aim of this subsection is to present basic properties needed to understand qualitatively this phenomena in the frame of our study. For further information, the lector should read [14] and references associated.

A glass is a noncrystalline solid obtained by cooling the material from a temperature above the melting point T_M. While cooling, a system can either crystallize or stay in a liquid-like state. This supercooled metastable state is viscoelastic in the case of polymers. When the structural rearrangements characteristic for the supercooled state cannot follow the cooling rate, the system falls out of equilibrium and transforms into a glassy solid - a "frozen" liquid - within the experimental observation time. This phenomenon, known as the glass transition, takes place in a temperature range that depends in general on the experimental cooling/heating conditions. Usually this temperature range is represented by only one temperature, the glass transition temperature T_g. Above T_g, the glassy state is unstable with respect not only to the supercooled liquid, but also to the crystalline solid. However, some degrees below T_g polymer glasses can be considered as "stable" from a practical point of view, i.e. their physical properties do not change much over time scales of several years although small changes, referred to as physical aging, are detectable.

There is some differences between melting and the glass transition. When you heat a crystalline polymer at a constant heat transfer rate, the temperature will increase at a constant rate until T_M. At this point, the temperature hold and all the energy is added in the melting process, (none of it goes into raising the temperature). This heat is called the latent heat of melting. This change in the heat capacity is a first order transition. Once the polymer has melted, the temperature begins to rise again, but at a slower rate. The molten polymer has a higher heat capacity than the solid crystalline polymer, so it can absorb more heat with the same increase in temperature. For the glass transition, the temperature keeps going up but at a different rate. The polymer undergoes an increase in its heat capacity when it undergoes the glass transition. Because the glass transition involves change in heat capacity, but it does not involve a latent heat, this transition is similar to a second order transition.

Glasses show a series of universal features:
They are characterized by long range structural disorder and some average short-range order. Their static structure factors S(Q) (obtained by neutron scattering or X-Ray, see ref. [14]) shows broad diffraction peaks revealing inter and intra molecular correlations. Another general finding is the occurrence of a series of dynamical processes, the so called α and β relaxations. Let us

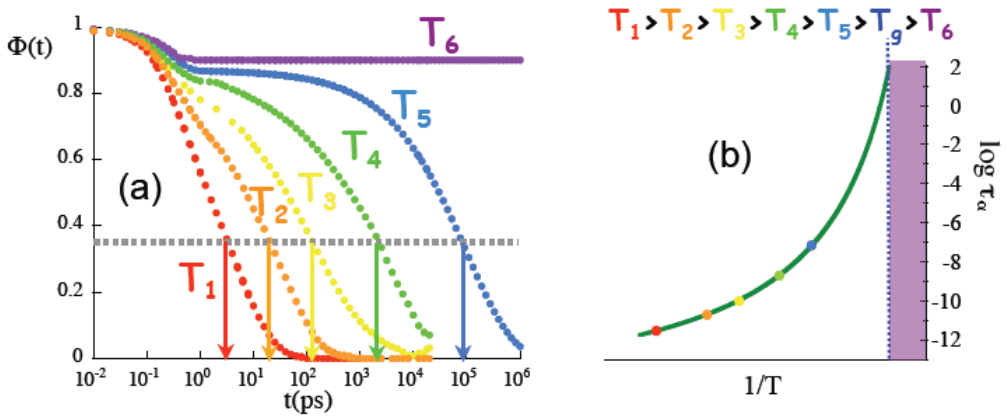

Figure 1.9 : *(a) Cartoon of the thermal evolution of a correlation function. (b) The characteristic time defined in (a) by the arrows displays a non-Arrhenius behavior. [14]*

follow the time evolution of a given correlation function $\Phi(t)$ of a glass former for different temperatures, as it is schematically shown in Fig. 1.9. At a high temperature (e.g., above the T_M), like T1 in the figure, $\Phi(t)$ decays in a single step at short times, of the order of picoseconds a behavior expected for a simple liquid. If the system is cooled down without crystallizing, there is a temperature range, which we will call T^*, where a second step in $\Phi(t)$ develops, slowing down the decay of the correlations at long times ($T^* \approx T2$ in the figure). This second step becomes more and more important when the temperature of the system decreases. The state of the system in this temperature region $T < T^*$ is what it is known as supercooled liquid state. In the neighborhood of T_g the correlations of the system are finally frozen and the obtained state is glassy (T6 in Fig. 1.9). The characteristic feature of the supercooled liquid in contraposition to the simple liquid state is thus the presence of the second slow step in $\Phi(t)$. This step is called the α-relaxation independently of the correlation observed or the experimental technique used. The characteristic time of this process (time where the correlation function decays to 1/e of the initial value in the time domain) follows a dramatic increase with decreasing temperature. This is schematically represented in Fig. 1.9b. In the neighborhood of T_g, this time reaches values of the order of minutes, and the system looks frozen at the timescale of observation. Below T_g, in the glassy state, the correlations do not decay anymore. Since the α-process is a universal feature of the dynamics of supercooled liquids, it is nowadays generally accepted that it origins

from a structural relaxation at the intermolecular level. Thereby, the features of the α-relaxation observed by different techniques are different projections of the actual structural α-relaxation. As the glass transition occurs when this relaxation freezes, the investigation of the dynamics of this process is of crucial interest, in order to understand the intriguing phenomenon of the glass transition. Below T_g the movements in matter are due principally to the dynamic of side groups, secondary relaxation ($\beta\,\gamma$) and the so-called boson peak. Up to date there have been several theoretical attempts to give account for these phenomenons. The approach by Adam and Gibbs is one of the most successful ones since it provides an explanation for the unusual thermal dependence of the timescale. However, the only microscopic theory available is the so-called Mode Coupling Theory (MCT); recently, landscape models have also been proposed to give account for some of its features.

In this work we will focuse on the study of the α-relaxation by BDS. We will now summarize the main experimental features needed to understand the BDS α-relaxation (see reference [21,22] for more details). The decay of the correlation function $\Phi(t)$ can be descried in the time domain by a stretched exponentially or Kohlraush-Williams-Watts (KWW) function [23, 24]:

$$\phi(t) \propto \exp\left[-\left(\frac{t}{\tau_{KWW}}\right)^{\beta_{KWW}}\right] \tag{1.50}$$

where τ_{KWW} is a characteristic time, β_{KWW} is the stretching parameter ($0 \leq \beta_{KWW} \leq 1$). All the experiments here reported will be made in te frequency domains where the process is characterized by a peak in the losses. The characteristic time of the relaxation, τ_α, is defined as the inverse of this maximum ($\tau_\alpha = 2\pi/f_{max}$). We can describe the shape of the dielectric spectrum in the frequency domain using an Havriliak Negami function [25, 26]:

$$\underline{\epsilon}(\omega) = \epsilon_\infty + \frac{\epsilon_s - \epsilon_\infty}{(1 + (i\,\omega\,\tau_{HN})^\alpha)^\gamma} \tag{1.51}$$

where τ_{HN} is a characteristic relaxation time, α and γ are shape parameters ($0 < \alpha, \gamma \leq 1$) describing respectively the symmetric and the asymmetric broadening of the equivalent relaxation time distribution function. The major drawback of the HN equation is the lack of justification of HN parameters in terms of a physical model. Following the approach of reference [27], we can correlate the HN equation to the KWW correlation relaxation by restricted the parameters as follow:

$$\gamma \;=\; 1 - 0.812(1-\alpha)^{0.387} \tag{1.52}$$

With the following relationships, we can define:

$$log(\tau_{KWW}) \;=\; log(\tau_{HN}) - 2.6(1-\beta_{KWW})^{0.5} exp(3\beta_{KWW}) \tag{1.53}$$

$$\beta_{KWW} \;=\; (\alpha\,\gamma)^{0.813} \tag{1.54}$$

in such way that the HN function can be considered as a good description of the Fourier Transform of the KWW one.

The temperature dependence of the relaxation time shows a dramatic increase when the glass transition temperature is approached. This non-Arrhenius dependance is usually well described in terms of the Vogel-Fulcher temperature dependance [28, 29]:

$$\tau(T) \;=\; \tau_0 \exp\left(\frac{B}{T - T_0}\right) \tag{1.55}$$

T_0 is known as the Vogel-Fulcher temperature and is usally located 30K to 50K below T_g. τ_0 is the asymptotic value of the relaxation time of the correlator Φ for $T \to \infty$. Note that introducing the shift factor $a_t = \tau(T)/\tau(T_{ref})$, this expression can be related with the one developed by William, Landel and Ferry [30]:

$$\log(a_t) = \frac{B}{T - T_0} - \frac{B}{T_{ref} - T_0} \tag{1.56}$$

$$\log(a_t) = \frac{C_1(T - T_{ref})}{T - T_{ref} + C_2} \tag{1.57}$$

with:

$$C_1 = \frac{B}{(T_{ref} - T_0)} \tag{1.58}$$

$$C_2 = T_{ref} - T_0 \tag{1.59}$$

3 Thermodynamic of mixing

Mixtures are systems consisting of two or more different chemical species. Binary mixtures consist of only two different species. An example of a binary mixture is a blend of polystyrene and poly(vinyl acetate). Mixtures with three components are called ternary. An example of a ternary mixture is a solution of polystyrene and poly(vinyl acetate) in toluene. If the mixture is uniform and all components of the mixture are intermixed on a molecular scale, the mixture is called homogeneous. An example of a homogeneous mixture is a polymer solution in a good solvent. If the mixture consists of several different phases (regions with different compositions), it is called heterogeneous. An example of a heterogeneous mixture is that of oil and water. Whether an equilibrium state of a given mixture is homogeneous or heterogeneous is determined by the composition dependence of the entropy and energy changes on mixing. Entropy always favours mixing, but energetic interactions between species can either promote or inhibit mixing. We will treat the case of a binary mixing, in the frame of a lattice model with no volume change.

3.1 Entropic contribution

We consider two species A and B and we assume that there is no volume change during mixing: volume V_A of species A is mixed with volume V_B of species B to make a mixture of volume $V_A + V_B$. The calculation assumes that the conformational entropy of a polymer is identical in the mixed and pure states. The mixture is macroscopically uniform and the two components are randomly mixed to fill the entire lattice. The volume fractions of the two components in the binary mixture are ϕ_A and ϕ_B:

$$\phi_A = \frac{V_A}{V_A + V_B} \tag{1.60}$$

$$\phi_B = \frac{V_B}{V_A + V_B} = 1 - \phi_A \tag{1.61}$$

We define the lattice site volume v_0 as the the smallest units occupied by one consisting unit as solvent molecules or monomers. Larger molecules like polymers occupy multiple connected

lattice sites. A molecule of species A has a molecular volume:

$$V_A = N_A v_0 \tag{1.62}$$

where N_A is the number of lattice site occupied by the species A. Regular solutions are mixtures of low molar mass species with $N_A = N_B = 1$. Polymer solutions are mixtures of macromolecules ($N_A = \mathrm{N} \gg 1$) with the low molar mass solvent defining the lattice ($N_B = 1$). Polymer blends are mixtures of macromolecules of different chemical species (N_A and $N_B \gg 1$). The combined system of volume $V_A + V_B$ occupies

$$n = \frac{V_A + V_B}{v_0} \tag{1.63}$$

lattice sites, while all molecules of species A occupy $V_A/v_0 = \mathrm{n}\ \phi_A$ sites. The number of molecules of species A is:

$$n_A = \frac{n\phi_A}{N_A} \tag{1.64}$$

The entropy S is determined as the product of the Boltzmann constant k and the natural logarithm of the number of ways Ω to arrange molecules on the lattice (the number of states).

$$S = k \ln(\Omega) \tag{1.65}$$

The number of translational states of a given single molecule is simply the number of independent positions that a molecule can have on the lattice, which is equal to the number of lattice sites. In a homogeneous mixture of A and B, each molecule has

$$\Omega_{AB} = n \tag{1.66}$$

The number of states Ω_A of each molecule of species A before mixing (in a pure A state) is equal to the number of lattice sites occupied by species A: $\Omega_A = \mathrm{n}\ \phi_A$. For a single molecule of species A, the entropy change on mixing is

$$\Delta S_A = k \ln(\Omega_{AB}) - k \ln(\Omega_A) = -k \ln(\phi_A) \tag{1.67}$$

Since the volume fraction is less than unity ($\phi_A < 1$), the entropy change upon mixing is always positive. Equation 1.67 holds for the entropy contribution of each molecule of species A, with a similar relation for species B. To calculate the total entropy of mixing, the entropy contributions from each molecule in the system are summed:

$$\Delta S_{mix} = n_A \Delta S_A + n_B \Delta S_B \tag{1.68}$$

$$= -k \left[n_A \ln(\phi_A) + n_B \ln(\phi_B) \right] \tag{1.69}$$

The entropy of mixing per lattice site $\Delta \overline{S}_{mix} = \Delta S_{mix}/v_0$ is an intrinsic thermodynamic quantity:

$$\Delta \overline{S}_{mix} = -k \left[\frac{\phi_A}{N_A} \ln(\phi_A) + \frac{\phi_B}{N_B} \ln(\phi_B) \right]. \tag{1.70}$$

3.2 Energetic contribution

The energy of mixing can be either negative (promoting mixing) or positive (opposing mixing). Regular solution theory can be applied for both possibilities, using the lattice model. To estimate the energy of mixing this theory places species into lattice sites randomly, ignoring any correlations. Thus, for all mixtures, favourable or unfavourable interactions between monomers are assumed to be small enough that they do not affect the random placement. Worse still, the regular solution approach effectively cuts the polymer chain into pieces that are the size of the solvent molecules (the lattice size) and distributes these pieces randomly. Such a mean-field approach ignores the correlations between monomers along the chain (the chain connectivity). Here, for simplicity, it is assumed that in polymer blends the monomer volumes of species A and B are identical. Regular solution theory writes the energy of mixing in terms of three pairwise interaction energies (u_{AA}, u_{BB}, and u_{AB}) between adjacent lattice sites occupied by the two species. A mean field is used to determine the average pairwise interaction U_A of a monomer of species A occupying one lattice site with a neighbouring monomer on one of the adjacent sites. For simplicity in the index notation we will use: $\phi_A = \phi$ and $\phi_B = 1 - \phi$. The probability of this neighbour being a monomer of species A is assumed to be the volume fraction ϕ of these molecules (ignoring the effect of interactions on this probability). The probability of this neighbour being a monomer of species B is $1 - \phi$. The average pairwise interaction of an A-monomer with one of its neighbouring monomers is a volume fraction weighted sum of interaction energies:

$$U_A = u_{AA}\phi + u_{AB}(1 - \phi) \tag{1.71}$$

Each lattice site of a regular lattice has z nearest neighbours, where z is the coordination number of the lattice. For example, z = 4 for a square lattice and z = 6 for a cubic lattice. Therefore, the average interaction energy of an A monomer with all of its z neighbours is zU_A. The average energy per monomer is half of this energy $zU_A/2$ due to the fact that every pairwise interaction is counted twice (once for the monomer in question and once for its neighbour). The number of sites occupied by species A (the number of monomers of species A) is $n\phi$, where n is the total number of sites in the combined system. Summing all the interactions gives the total interaction energy of the mixture:

$$U = \frac{zn}{2}\left[U_A\phi + U_B(1 - \phi)\right], \tag{1.72}$$

$$= \frac{zn}{2}\left[u_{AA}\phi^2 + 2u_{AB}\phi(1 - \phi) + u_{BB}(1 - \phi)^2\right]. \tag{1.73}$$

The total energy of both species before mixing is the sum of the energies of the two pure components:

$$U_0 = \frac{zn}{2}\left[u_{AA}\phi + u_{BB}(1 - \phi)\right]. \tag{1.74}$$

We can now define another intrinsic properties, the energy change on mixing per site:

$$\Delta\overline{U}_{mix} = \frac{U - U_0}{n} = \frac{z}{2}\phi(1 - \phi)(2u_{AB} - u_{AA} - u_{BB}). \tag{1.75}$$

The Flory interaction parameter χ is defined to characterize the difference of interaction energies in the mixture:

$$\chi = \frac{z}{2kT}(2u_{AB} - u_{AA} - u_{BB}). \tag{1.76}$$

χ is a dimensionless measure of the differences in the strength of pairwise interaction energies between species in a mixture (compared with the same species in their pure component states). Using this definition, we write the energy of mixing per lattice site as

$$\Delta\overline{U}_{mix} = \chi\phi(1-\phi)kT. \tag{1.77}$$

χ is an important parameter in the study of polymer mixture. Most of these interaction parameters have been tabulated, see reference [13] and reference there-in. For miscible polymer blends χ can be measured using small-angle neutron scattering, usually involving deuterium labelling of one blend component. For non-polar mixtures with species interacting mainly by dispersion forces, the Flory interaction parameter can be estimated by a method based on the solubility parameter δ related to the energy of of a molecule:

$$\chi \simeq \frac{v_0}{kT}(\delta_A - \delta_B)^2. \tag{1.78}$$

One of the major assumptions of the Flory-Huggins theory is that there is no volume change on mixing and that monomers of both species can fit on the sites of the same lattice. In most real polymer blends, the volume per monomer changes upon mixing. Some monomers may pack together better with certain other monomers. The volume change on mixing and local packing effects lead to a temperature-independent additive constant in the expression of the Flory interaction parameter. In practice, these effects are not fully understood and all deviations from the lattice model are lumped into the interaction parameter which can display non-trivial dependences on composition, chain length, and temperature. Empirically, the temperature dependence of the Flory interaction parameter is often written as the sum of two terms:

$$\chi(T) \simeq A + \frac{B}{T}. \tag{1.79}$$

The temperature-independent term A is referred to as the "entropic part" of ẇhile B/T is called the "enthalpic part". The parameters A and B have been tabulated for many polymer blends [13].

3.3 Equilibrium and phase diagram

Using equations 1.70 and 1.75 we can define the Helmholtz free energy of mixing per lattice site $\Delta\overline{F}_{mix}$:

$$\Delta\overline{F}_{mix} = \Delta\overline{U}_{mix} - T\Delta\overline{S}_{mix}, \tag{1.80}$$

$$= kT\left[\frac{\phi}{N_A}\ln(\phi) + \frac{1-\phi}{N_B}\ln(1-\phi) + \chi\phi(1-\phi)\right]. \tag{1.81}$$

The first two terms in the free energy of mixing have entropic origin and always act to promote mixing, although with blends of long chain polymers these terms are quite small. The last term has energetic origin, and can be positive (opposing mixing), zero (ideal mixtures), or negative (promoting mixing) depending on the sign of the interaction parameter χ. If there is a net attraction between species (i.e. they like each other better than they like themselves), $\chi < 0$ and a single-phase mixture is favourable for all compositions. More often there is a net repulsion between species (they like themselves more than each other) and the Flory interaction parameter is positive $\chi > 0$. In this case the equilibrium state of the mixture depends not on the sign of the free energy of mixing $\Delta\overline{F}_{mix}$ at the particular composition of interest, but on the functional

dependence of this free energy on the composition ϕ for the whole range of compositions. This functional dependence $\Delta\overline{F}_{mix}(\phi)$ depends on the value of the Flory interaction parameter χ as well as on the degrees of polymerization of both molecules N_A and N_B. This function is always convex near the boundaries of the composition range (for ϕ near zero and unity) because the entropic part always dominates there at any practical (non-zero) temperature. If the composition dependence of the free energy of mixing is convex over the whole composition range, the mixture is homogeneous at all compositions. If the free energy is concave in some part of the composition range (due to energetic contribution), the line of common tangent to the free energy curve determines the range of the miscibility gap. This criterium is written as:

$$\left(\frac{\partial\Delta\overline{F}_{mix}}{\partial\phi}\right)_{\phi=\phi'} = \left(\frac{\partial\Delta\overline{F}_{mix}}{\partial\phi}\right)_{\phi=\phi''} \tag{1.82}$$

where ϕ' and ϕ'' are two compositions of the system. This derivative of the free energy of mixing per site with respect to volume fraction of component A is:

$$\frac{\partial\Delta\overline{F}_{mix}}{\partial\phi} = kT\left[\frac{\ln(\phi)}{N_A}\frac{1}{N_A} + \frac{\ln(1-\phi)}{N_B} - \frac{1}{N_B} + \chi(1-2\phi)\right] \tag{1.83}$$

For the simple example of a symmetric polymer blend with $N_A = N_B = \mathrm{N}$. the common tangent line is horizontal.

$$\left(\frac{\partial\Delta\overline{F}_{mix}}{\partial\phi}\right)_{\phi=\phi'} = \left(\frac{\partial\Delta\overline{F}_{mix}}{\partial\phi}\right)_{\phi=\phi''} \tag{1.84}$$

$$= kT\left[\frac{\ln(\phi)}{N} + \frac{\ln(1-\phi)}{N} + \chi(1-2\phi)\right] = 0 \tag{1.85}$$

$$\tag{1.86}$$

The above equation can be solved for the interaction parameter corresponding to the phase boundary: the binodal (solid line in the bottom part of Fig. 1.10) of a symmetric blend:

$$\chi_b = \frac{\ln(\phi/(1-\phi))}{2\phi-1)N} \tag{1.87}$$

The binodal separates the homogeneous (single phase) and heterogeneous (two phase) regions in the phase diagram. For binary mixtures, the binodal line is also the coexistence curve, defined by the common tangent line to the composition dependence of the free energy of mixing curve, and gives the equilibrium compositions of the two phases obtained when the overall composition is inside the miscibility gap.

The local curvature of the free energy as a function of of the phase composition determines local stability. If the composition dependence of the free energy is concave, the system can spontaneously lower its free energy by phase separating into two phases. On the other hand, when the composition dependence of the free energy is convex, any mixed state has lower free energy than any state the blend could phase separate making the mixed state locally stable. Returning to the general case of an asymmetric blend, the criterion for local stability is written

in terms of the second derivative of the free energy:

$$\frac{\partial^2 \Delta \overline{F}_{mix}}{\partial \phi^2} > 0 \qquad Unstalbe, \tag{1.88}$$

$$\frac{\partial^2 \Delta \overline{F}_{mix}}{\partial \phi^2} < 0 \qquad Locally\, stable. \tag{1.89}$$

The spinodal curve defined by:

$$\frac{\partial^2 \Delta \overline{F}_{mix}}{\partial \phi^2} = kT\left[\frac{1}{N_A \phi} + \frac{1}{N_B(1-\phi)} - 2\chi\right] = 0 \tag{1.90}$$

$$\chi_s = \frac{1}{2}\left(\frac{1}{N_A \phi} + \frac{1}{N_B(1-\phi)}\right) \tag{1.91}$$

determines by the inflection points of the composition dependence of the free energy of mixing curve, separates unstable and metastable regions within the miscibility gap (Fig. 1.10).

An example of phase diagram for a symetric blend is shown in Fig. 1.10. For a composition

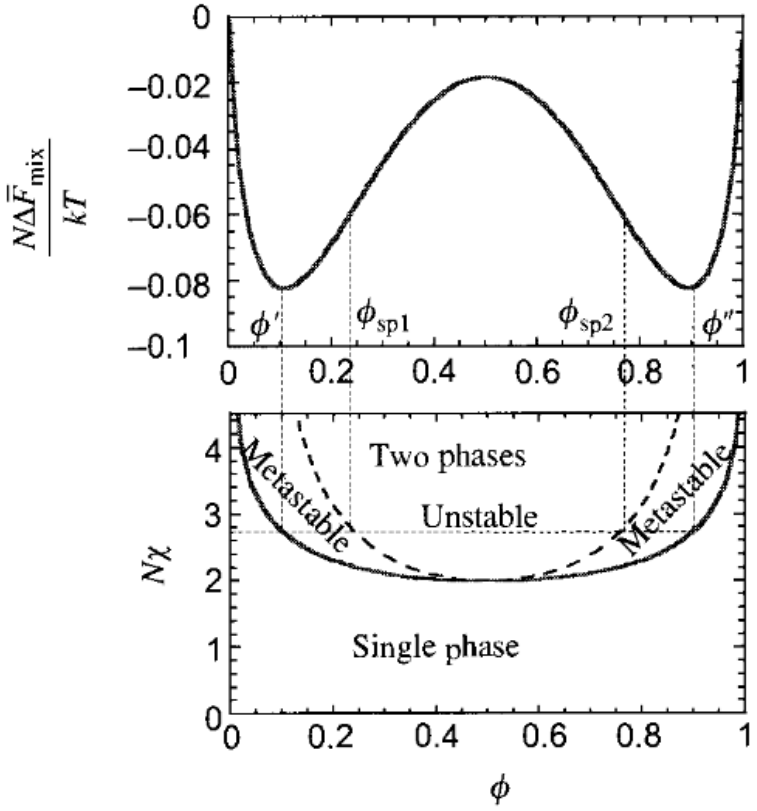

Figure 1.10 : *Composition dependence of the free energy of mixing for a symmetric polymer blend with the product $\chi N = 2.1$ (top figure) and the corresponding phase diagram (bottom figure). Binodal (solid curve) and spinodal (dashed curve) are shown on the phase diagram. [13]*

in the two phase unstable part of the diagram, the system will spontaneously phase separate into two phases with compositions given by the values on the binodal curve. This spontaneous phase separation, called spinodal decomposition, occurs because the mixture is locally unstable. Any small composition fluctuation is sufficient to initiate the phase separation process. The points of the phase diagram between the spinodal and binodal curves correspond to metastable mixtures.

The metastable homogeneous state is stable against small composition fluctuations and requires a larger nucleation event to initiate phase separation into the equilibrium phases given by the coexistence curve. This phase separation process is called nucleation and growth. The point of the phase diagram below the binodal corresponds to stable homogeneous composition.

Experimentally, the interaction parameter is most conveniently changed by varying temperature T (Eq. 1.79). Phase diagrams can be plotted in the temperature - composition plane.

Conclusion on the overview on polymers

Polymers are formed by repetitive covalent bonding of chemical monomers. Some polymer characteristics, such as degree of polymerization, polydispersity, microstructure, architecture and chemical composition are fixed during polymerization. These characteristics control many important properties of polymeric materials. The static conformation of an ideal chain (with no interaction between monomers separated by many bonds along the chain) can be described by the random walk model. It is convenient to define the Kuhn monomer of length b and the number of Kuhn monomers N such that the mean-square end-to-end distance of an ideal linear chain is a freely jointed chain.

The dynamics of polymer can be characterized by a large scale and a segmental motion. At this day no physical theory can relate properly all the aspects of the segmental motion. Rouse theory and the reptational tube model are well known to describe the large scale dynamics of non entangled and entangled polymers, respectively. These theory and model predict an exponent 2 and 3 in the molecular weight dependence of the longest relaxation time, respectively. We have shown that in the frame of the Rouse model, expressions of the frequency dependence of the dielectric permittivity and shear modulus can be written as:

$$\begin{aligned}
\epsilon'(\omega) &\propto \frac{2b^2}{N}\sum_{p:odd}^{N-1} cot^2\left(\frac{p\pi}{2N}\right)\frac{1}{1+\omega^2\tau_p^2} \\
\epsilon''(\omega) &\propto \frac{2b^2}{N}\sum_{p:odd}^{N-1} cot^2\left(\frac{p\pi}{2N}\right)\frac{\omega\tau_p}{1+\omega^2\tau_p^2} \\
G'(\omega) &\propto \sum_{p=1}^{N-1}\frac{\omega^2\tau_p^2/4}{1+\omega^2\tau_p^2/4} \\
G''(\omega) &\propto \sum_{p=1}^{N-1}\frac{\omega\tau_p/2}{1+\omega^2\tau_p^2/4}
\end{aligned}$$

where τ_p are the relaxation times of the Rouse modes.

When different polymers are mixed, they can either form a single phase or phase separated domains. This phenomena can be described by the study of the free Helmholtz energy. The Flory interaction parameter χ plays an important role in the expression of the free Helmholtz energy. If there is a net attraction between species (i.e. they like each other better than they like themselves), $\chi < 0$ and a single phase mixture is favourable for all compositions. More often there is a net repulsion between species (they like themselves more than each other) and the Flory interaction parameter is positive $\chi > 0$. In this case the equilibrium state of the mixture depends on the functional dependence of the free energy on the composition for the whole range of compositions.

Chapter 2

Segmental dynamics, test of the Rouse model and effect of entanglement at the macroscale

Summary

Introduction

The aim of this chapter is to discuss the models describing the polymer dynamics at macroscopic scale and present the different experimental techniques that permit to test these models. We will first focuse our study on the segmental dynamics of poly(vynil acetate) (PVAc) before studying the whole chain motion of polyisoprene (PI).

PVAc has a strong ($\Delta\epsilon \sim 5$) dipolar component perpendicular to the chain backbone leading to the so-called α-relaxation, related with segmental motion. At this day, this relaxation can only be described by semi-phenomenological theories. Even if we are not currently able to test any physical theory to interpret the α-relaxation, the study of PVAc is interesting because it exhibits strong losses slightly above room temperature. Therefore, it is a convenient candidate to develop Electrostatic Force Microscopy based nano-characterization methods; and the dielectric macroscopic response here measured will be then compared to the nanoscopic one in the following chapters of this thesis.

Due to dipolar components both parallel and perpendicular to the chain backbone, PI exhibits a whole chain dielectric relaxation (normal mode) in addition to that associated with segmental motion. The Rouse model [17], has been first developed to describe the dynamics of polymer solution in a theta solvent, i.e. a solvent in which polymer coils act like ideal chains, assuming exactly their random walk coil dimensions. This model is now well known to describe rather correctly the whole chain dynamics of unentangled polymers. In the past, the validity of the Rouse model has ever been instigated by means of different experimental techniques (Broadband Dielectric Spectroscopy (BDS), rheology, neutron scattering) and also by molecular dynamics simulations. However this study is still challenging because in unentangled polymer the segmental dynamics contributions overlap significantly with the whole chain dynamics. In this chapter, we will demonstrate how we have been able to decorelate the effect of the α-relaxation on the normal mode in order to test how the Rouse model can quantitatively describes the normal mode measured by BDS and rheology. The introduction of polydispersity is a key point of this study.

The reptational tube theory, first introduced by de Gennes [15] and developed by Doi and Edwads [16] describes the dynamics of entangled polymers where the Rouse model can not be applied. Many corrections (as Contour Length Fluctuation or Constraints Release) have been added to the pure reptation in order to reach a totally predictive theory [19, 20]. In the last part of this chapter, we will show how the relaxation time of the large chain dynamics depends on molecular weight and discuss the effects of entanglement predicted by de Gennes theory on dielectric spectra. PI is a canonical polymer to study and understand the large chain dynamics. However, due to its very weak relaxation ($\Delta\epsilon \sim 0.05$, around 100 times weaker than the relaxation of PVAc), the measurement of this dynamics at nanoscale is still challenging.

1 Materials and method

1.1 Macroscopic Samples

Polymers can have dipoles in the monomeric unit that can be decomposed in two different components: parallel or perpendicular to the chain backbone. The non canceling dipole moment parallel to the chain backbone giving rise to an "end-to-end" net polarization vector will induce the so-called dielectric normal mode dielectric relaxation that can be studied using theoretical models. The dipole moment perpendicular to the chain backbone will lead to the segmental α-relaxation that can only be described using empirical models, since no definitive theoritical framework exists for this universal process.

We have chosen to study the relaxations of two different samples. The first is 1,4-cis-polyisoprene (PI). This isomer is a A-type polymer in the Stockmayer classification [31]: it carries both local dipole moments parallel and perpendicular to the chain backbone. The chapter on the large scale dynamics will be focused on the study of the dynamics of the normal mode of PI. The second is poly(vinyl acetate) (PVAc), a B-type polymer that does not present a net component along the chain. Therefore it is not possible to test the theoretical theories describing the normal mode on PVAc. However, this canonical polymer has a dipole component perpendicular to the chain backbone leading to a strong segmental relaxation. This so-called α-relaxation appears around 10 Hz slightly above room temperature and makes him a very convenient candidate for the development of nano-dielectric characterization methods. We will study this polymer as a pure component and in a blend with polystyrene (PS). This last polymer is well known for having an extremely weak relaxation only detected above 100°C and will be used as an non-active component in a blend containing 75% of PS and 25 % of PVAc.

a Polyisoprene

The polyisoprene (PI) samples were obtained from anionic polymerization of isoprene (Fig. 2.1). According to the supplier, Polymer Source, the sample is linear (no ramification) and its micro-composition is 80% cis, 15% trans and 5% other 2.1. We are working with the isomer *cis* that have a net end-to-end polarization vector. Before the experiments samples were dried in a vacuum oven at 70 °C for 24 hours to remove any trace of solvent.

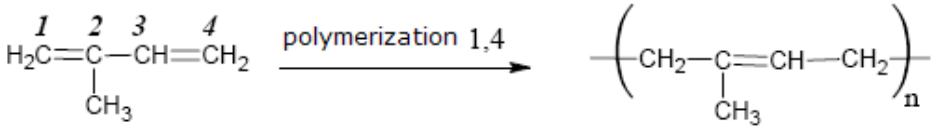

(a) *Polymerization 1,4 of isoprene*

(b) *cis- and trans- isomers of polyisoprene*

Figure 2.1 : *Polymerization of isoprene*

For our study, seven samples have been chosen to cover a large band of molecular weight with low polydispersity (Table 2.1). The polydispersity (determined from size-exclusion chromatography experiments) is given by supplier while the glass transition temperature (T_g) has been measured by dynamic scanning calorimetry. To avoid oxidation, PI samples were stored at -25 ºC.

Sample	M_n [kg/mol]	M_w [kg/mol]	I_p	T_g [K]
PI-1	1.1	1.2	1.11	194
PI-3	2.7	2.9	1.06	203
PI-10	10.1	10.5	1.04	209
PI-33	33.5	34.5	1.04	210
PI-82	76.5	82	1.07	210
PI-145	138	145	1.07	210
PI-320	281	320	1.14	210

Table 2.1 : *Molecular weight, polydispersity and T_g of PI*

b Poly(vinyl acetate)

The molecular formula of Poly(vinyl acetate) (PVAc) is $(C_4H_6O_2)_n$ (Fig. 2.2. The monomer has a molecular weight of 86 g/mol and we will be working with a sample having a molecular weight of M_w = 83 000 g /mol. The sample has been provided by Sigma Aldrich. The T_g has been measured at 38 ºC. Prior to the measurements, samples were kept at 180°C in vacuum for at least 24 h to remove any solvent or moisture content as structural relaxation of PVAc is known to be sensitive to moisture content.

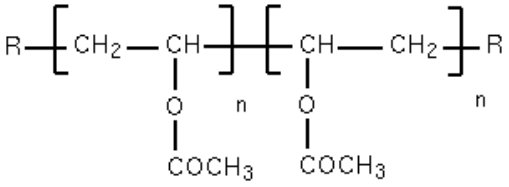

Figure 2.2 : *Schematic representation of the monomer of PVAc*

c Polystyrene

The molecular formula of Polystyrene (PS) is $(C_8H_8)_n$ (Fig. 2.3. The monomer has a molecular weight of 104 g/mol and we will be working with a sample having a molecular weight of M_w = 70 950 g /mol. The sample has been provided by Polymer Laboratories. A drying was performed under vacuum at 180ºC for at least 24 hours before measurements.

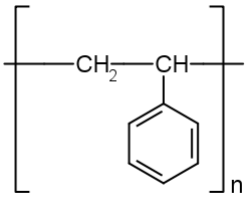

Figure 2.3 : *Schematic representation of the monomer of PS*

1.2 Rheology

RHEOMETER
ARES-LS2, TA Instruments (1mHz - 50 Hz)
Transducers: 2K FRTN1 and 200 FRTN1
LN2 controller (130 - 800 K)
Simultaneous electric impedance analysis (20Hz - 1MHz)

Elasticity is the ability of a material to store deformational energy, and can be viewed as the capacity of a material to regain its original shape after being deformed. Viscosity is a measure of the ability of a material to resist flow, and reflects dissipation of deformational energy through flow. Material will respond to an applied force by exhibiting either elastic or viscous behavior, or more commonly, a combination of both mechanisms. The combined behavior is termed viscoelasticity. In rheological measurements, the deformational force is expressed as the stress, or force per unit area. The degree of deformation applied to a material is called the strain. Strain may also be expressed as sample displacement (after deformation) relative to pre-deformation sample dimensions.

Dynamic mechanical testing involves the application of an oscillatory strain $\gamma(t) = \gamma_0\, cos(\omega t)$ to a sample. The resulting sinusoidal stress $\sigma(t) = \sigma_0\, cos(\omega t + \delta)$ is measured and correlated against the input strain, and the viscous and elastic properties of the sample are simultaneously measured.

If the sample behaves as an ideal elastic solid, then the resulting stress is proportional to the strain amplitude (Hooke's Law), and the stress and strain signals are in phase. The coefficient of proportionality is called the shear modulus G. $\sigma(t) = G\,\gamma_0\, cos(\omega t)$ If the sample behaves as an ideal fluid, then the stress is proportional to the strain rate, or the first derivative of the strain (Newton's Law). In this case, the stress signal is out of phase with the strain, leading it by 90°. The coefficient of proportionality is the viscosity η. $\sigma(t) = \eta\,\omega\,\gamma_0\, cos(\omega t + \pi/2)$

For viscoelastic materials, the phase angle shift (δ) between stress and strain occurs between the elastic and viscous extremes. The stress signal generated by a viscoelastic material can be separated into two components: an elastic stress (σ') that is in phase with strain, and a viscous stress (σ") that is in phase with the strain rate (dγ/dt) but 90° out of phase with strain. The elastic and viscous stresses are sometimes referred to as the in-phase and out-of-phase stresses, respectively. The elastic stress is a measure of the degree to which the material behaves as an elastic solid. The viscous stress is a measure of the degree to which the material behaves as an

ideal fluid. By separating the stress into these components, both strain amplitude and strain rate dependence of a material can be simultaneously measured. We can resume this paragraph by a set of equation:

$$\sigma(t) = \left(\frac{\sigma_0\, cos(\delta)}{\gamma_0}\right)\gamma_0\, cos(\omega\, t) + \left(\frac{\sigma_0\, sin(\delta)}{\gamma_0}\right)\gamma_0\, sin(\omega\, t) \tag{2.1}$$

$$G' = \frac{\sigma_0\, cos(\delta)}{\gamma_0} \quad G'' = \frac{\sigma_0\, cos(\delta)}{\gamma_0} \tag{2.2}$$

$$\underline{G}(\omega) = G' + iG'' \tag{2.3}$$

Concretely, the sample is placed between the two plates represented in Fig. 2.4. A motor apply a strain to the bottom plate and the movement of the upper plate is recorded. The typical value for the gap is 1 mm.

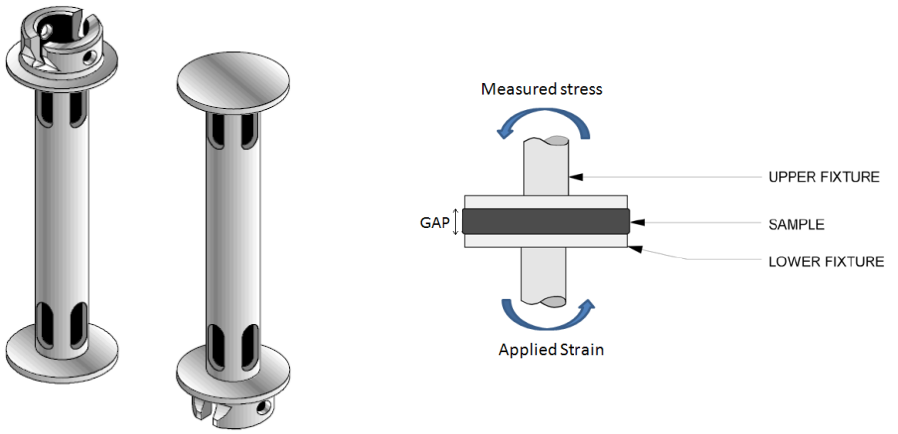

(a) *Parallel plate tool* **(b)** *Sample between plates (the strain is in an horizantal plane)*

Figure 2.4 : *Shematic view of rheological tools*

1.3 Broadband dielectric spectroscopy

BROADBAND DIELECTRIC SPECTROSCOPY
High-resolution dielectric/impedance analyzer
ALPHA-S, Novocontrol
Frequency range: 1e-3 - 1e7 Hz ,
Sensitivity : $tan(\delta) \sim 1e-5$
Temperature Control (100 - 600 K, stability $\pm 0.01K$) :
Nitrogen-jet stream Quatro Cryosystem, Novocontrol

The set-up of a broadband dielectric spectroscopy (BDS) experiment is displayed in Fig. 2.5. The sample is placed between two electrodes of a capacitor and polarized by a sinusoidal voltage $\underline{U}(\omega)$. The result of this phenomena is the orientation of dipoles which will create a capacitive

system. The current $\underline{I}(\omega)$ due to the polarization is then measured between the electrode. The complex capacity $\underline{C}(\omega)$ of this system is describe by the complex dielectric function $\underline{\epsilon}(\omega)$ as:

$$\underline{\epsilon}(\omega) = \epsilon'(\omega) - i\,\epsilon''(\omega) = \frac{\underline{C}(\omega)}{C_0} = \frac{\underline{J}(\omega)}{i\,\omega\,\epsilon_0 \underline{E}(\omega)} = \frac{\underline{I}(\omega)}{i\,\omega\,\underline{U}(\omega)\,C_0} \tag{2.4}$$

where: C_0 is the vacuum capacitance of the arrangement
$\underline{E}(\omega)$ is the sinusoidal electric field applied (within the linear response)
$\underline{J}(\omega)$ is the complex current density
$\epsilon_0 = 8.85\,10^{-12} A\,s\,V^{-1}\,m^{-1}$is the permittivity of vacuum
ϵ' and ϵ'' are proportional to the energy stored and lost in the sample, respectively.

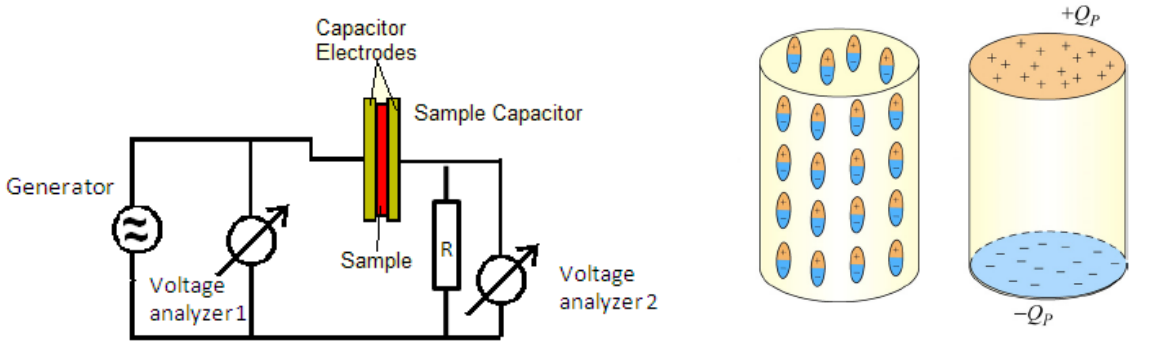

(a) *Schema of the principle of BDS*

(b) *Polarization of matter and resulting capacitive system*

Figure 2.5 : *Schema of the principle of BDS*

In our experiments samples were placed between parallel gold-plated electrodes of 20 mm diameter and the value of the gap (between the electrodes) was fixed to 0.1mm (by a narrow PTFE cross shape piece).

Polarization of matter ($\overrightarrow{P}$) can be describe as damped harmonic oscillator. When the electromagnetic field is sinusoidal the dipole oscillates around its position of equilibrium. This response is characterized by $\underline{\epsilon}(\omega)$:

$$\overrightarrow{P} = \epsilon_0\,(\underline{\epsilon}(\omega) - 1)\,\overrightarrow{E}(\omega) \tag{2.5}$$

The complex dielectric function is the one-sided Fourier or pure imaginary Laplace transform of the correlation function of the polarization fluctuations $\phi(t) = [\overrightarrow{P}(t) \cdot \overrightarrow{P}(0)]$ (phenomological theory of dielectric relaxation [25])

$$\frac{\underline{\epsilon}(\omega) - \epsilon_\infty}{\epsilon_s - \epsilon_\infty} = \int_0^\infty \exp(-i\,\omega\,t)\left(-\frac{d\phi(t)}{dt}\right) dt \tag{2.6}$$

where ϵ_s and ϵ_∞ are are the unrelaxed and relaxed values of the dielectric constant

If we consider a "Debye process" (the dissipation of the fluctuation is exponential: $\phi(t) = \exp(-t/\tau)$) we obtain:

$$\frac{\epsilon'(\omega) - \epsilon_\infty}{\epsilon_s - \epsilon_\infty} = \frac{1}{1 + \omega^2\,\tau^2} \tag{2.7}$$

$$\frac{\epsilon''(\omega)}{\epsilon_s - \epsilon_\infty} = \frac{\omega\,\tau}{1 + \omega^2\,\tau^2} \tag{2.8}$$

1.4 Differential scanning calorimetry

DIFFERENTIAL SCANNING CALORIMETRY
Q2000 TMDSC, TA Instruments
Refrigerated Cooling System RCS90 (100 -700 K)

Differential scanning calorimetry (DSC) permits to measure the glass transition as a change in heat capacity of as the polymer go from the glass state to the rubber state. The sample material, encapsulated in a pan, and an empty reference pan sit on a thermoelectric disk surrounded by a furnace. As the temperature of the furnace is changed by heating at a linear rate, heat is transferred to the sample and reference through the thermoelectric disk. The differential heat flow to the sample and reference is measured by area thermocouples using the thermal equivalent of Ohm's Law:

$$q = \frac{\Delta T}{R} \tag{2.9}$$

where: q is the sample heat flow, ΔT is the temperature difference between sample and reference and R is the resistance of the thermoelectric disk. More elaborate expression exists to take into account extraneous heat flow within the sensor or between the sensor and sample pan. (See reference [32] for more details.)

Polymers have a higher heat capacity above the glass transition temperature than below. Because of this change in heat capacity that occurs at the glass transition, we can use DSC to measure a polymer's glass transition temperature. The change doesn't occur suddenly, but takes place over a temperature range. We conventionally measure T_g by a taking the middle of the linear extrapolation of the curve as it is usual in DSC.

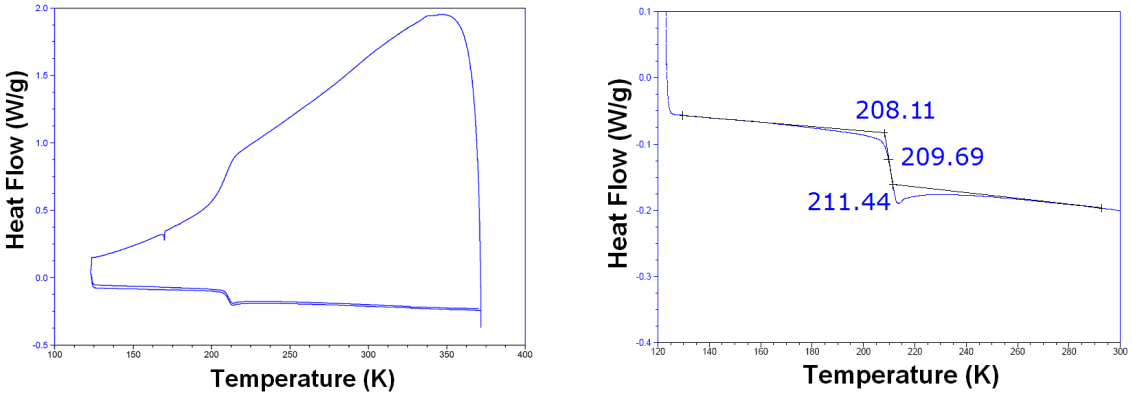

Figure 2.6 : *DSC of PI33. Left: all the cycle ; Right: zoom on the glassy temperature*

Measurements have been made on the Q2000 TMDSC from TA Instruments. Samples have been prepared with hermetic lid and stored for 12 hours in an oven under vacuum at 70°C to remove all traces of impurity and rest of any solvents. The typical mass was of about 5 mg and the rate of heating was 10 K/min. For each sample, we used a linear extrapolation to determine the glassy temperature as it is shown for PI33 on Fig. 2.6. Values of T_g are reported in the section Material.

2 Segmental dynamics

2.1 BDS study of PVAc pure and in a blend of PS

The dynamics of PVAc have been largely studied by BDS (see [22, 27] and reference therein). However, no trace has been found in the literature about the dielectric study of the blend PVAc/PS. In this section we will compare dielectric results of a pure PVAc sample to the one obtained from a blend having a 25% PVAc and 75% PS composition. The Flory interaction of these constituent is given in reference [33]: $\chi_{(PS/PVAc)} = 0.02$. Using this parameter authors constructed a phase diagram where it appears that PS and PVAc are immiscible, and form a phase separated system. This blend is interesting in the frame of this work because BDS allows measuring the average signal of the blend while measurement at the nanoscopic using Electrostatic Force Microscopy permits to differentiate properties of the nano-structured domains.

a Pure PVAc

Fig. 2.7 represents the real and imaginary parts of the α-relaxation as it can be measured by BDS. The first think to note on this graph is that the time temperature superposition is rather well respected although not completely [27]. Even if the half width at middle height of ϵ" is slightly decreasing with temperature, curves are shifted without any important changes in the shape. In the real part, we can observe the characteristic step $\Delta\epsilon$ from the low (ϵ_s) to high

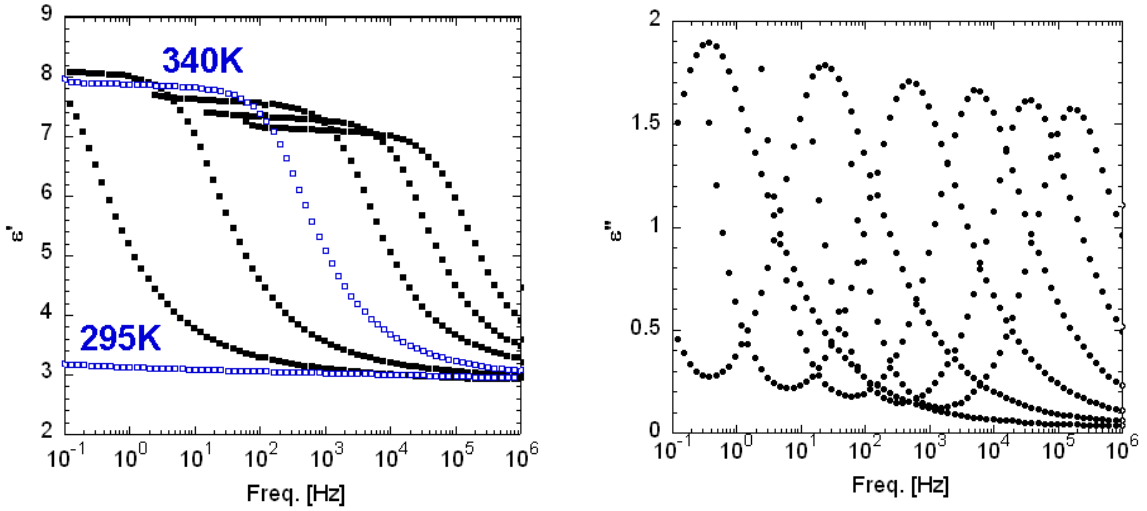

(a) *Real part of the dielectric constant at different temperature (from 320 to 370K, ΔT =10K). Unfilled square represent the temperatures of 295K and 340K that we will be used for the nanoscopic static characterization*

(b) *Imaginary part of the dielectric constant at different temperature (from 320 to 370K, ΔT =10K)*

Figure 2.7 : *Dielectric α-relaxation of PVAc*

(ϵ_∞) frequency value of the relative dielectric permittivity. It is interesting to note the value of ϵ_s at 295K and 340K because these temperatures will be used in the nanoscopic static dielectric characterization using Electrostatic Force Microscopy. As at these temperatures and frequencies $\epsilon' \gg \epsilon''$, the low frequency limit of the the dielectric constant ϵ_r can be approximated by the

value of the real part:

$$\epsilon_r(295\,K) \simeq \epsilon'_s(295\,K) \simeq 3 \tag{2.10}$$
$$\epsilon_r(340\,K) \simeq \epsilon'_s(340\,K) \simeq 8 \tag{2.11}$$

b Blend 25% PVAc 75% PS

The miscibility of PVAc and PS has been investigated by different group, see [34] and reference there-in. It appears that the miscibility depends on synthesis' conditions. Fig. 2.8 represents the frequency dependance of the imaginary part of the dielectric permittivity of the pure PVAc sample and the blend of PVAc-PS. The peak measure in the blend is slightly broadened and faster than the pure PVAc component. The shape parameter β_{KWW} has a value for the pure and the blend:

$$\beta^p_{KWW} = 0.49 \tag{2.12}$$
$$\beta^b_{KWW} = 0.43 \tag{2.13}$$

The facts that both shape and relaxation time are close indicate a non miscibility of the two components with a single phase of PVAc.

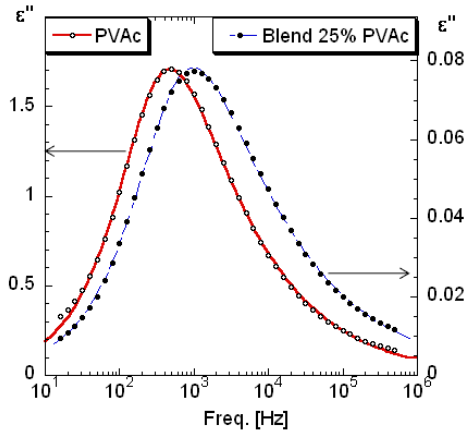

Figure 2.8 : *Comparison of the shape of the losses measured in pure PVAc and in the blend. The dynamics is measured slightly faster and broader in the blend.*

One possible hypothesis to explain this faster dynamics could be related with the fact that BDS measure dielectric properties macroscopically, over the all sample, including the interfaces' regions between PVAc and PS having a different dynamics.

These results are preliminary and further research should be done to verify them (with different concentration of PVAc for instance) and test the other possible hypothesis (like density effects or possible partial miscibility) to explain this change in the dynamics. These data will be later compared to those obtained at the nanoscale.

2.2 Resolving the normal mode from the α-relaxation for low molecular weight polyisoprene

For low molecular weight, the normal mode of PI overlaps at high frequency with the α-relaxation (Fig. 2.9).

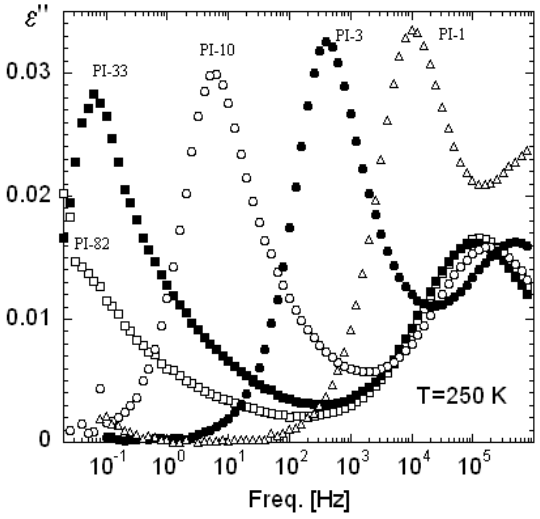

Figure 2.9 : *Dielectric relaxation curves collected at 250 K on PI with different molecular weights.*

This overlapping is an intrinsic problem in checking the Rouse model (that describes the normal mode dynamics, see next section), since its applicability is limited to chains with moderate molecular weight (below the molecular weight between entanglements). In fact, even by microscopic techniques with spatial resolution as neutron scattering, it is rather difficult to distinguish the border between chain and segmental relaxations [14].Because the time scale separation between the two dynamical processes is not complete, a detailed analysis of the validity of the Rouse model predictions at high frequencies requires accounting accurately for the α-relaxation contribution.

The imaginary part of the dielectric α-relaxation can be analyzed by using the phenomenological Havriliak-Negami function (Eq. 1.51). In addition, a power law contribution ($\propto \omega^{-1}$) was used to account for the normal mode contribution at low frequencies, which is the frequency dependence expected from the Rouse model for frequencies larger than the characteristic one of the shortest mode contribution. Thus, we assumed that the high frequency tail of the normal mode follows a C/ω law and superimposes on the low frequency part of the alpha relaxation losses, being C a free fitting parameter at this stage. The α-relaxation time corresponding to the loss peak maximum was obtained from the parameters of the HN function as follows [25]:

$$\tau_\alpha = \tau_{HN} \frac{\left[sin\left(\frac{\alpha\gamma\pi}{2+2\gamma}\right)\right]^{1/\alpha}}{\left[sin\left(\frac{\alpha\pi}{2+2\gamma}\right)\right]^{1/\alpha}} \tag{2.14}$$

The results obtained for samples with different molecular weight at a common temperature of 230 K are shown in Fig. 2.10. It is evident that in the low molecular weight range the

time scale of the segmental dynamics is considerably faster than that corresponding to the high molecular weight limit. This behavior is mainly associated with the plasticizer-like effect of the enchain groups, which are more and more relevant as chain molecular weight decreases. The line in figure 2.10 describing the experimental behavior for the PI samples investigated is given by an empirical function:

$$\tau_\alpha(M) = \frac{\tau_\alpha(\infty)}{(1 + 10000/M)^2} \tag{2.15}$$

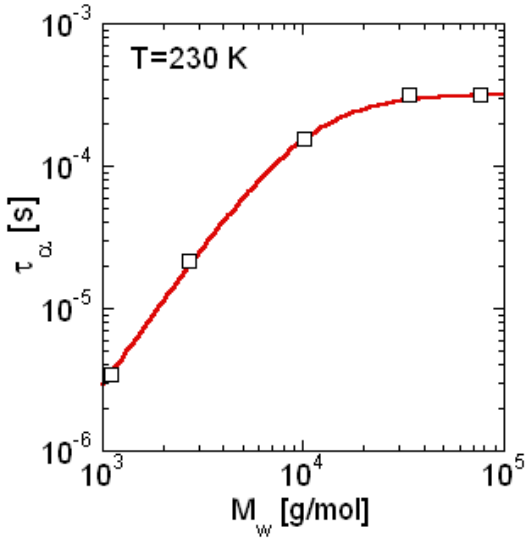

Figure 2.10 : *α-relaxation times of polyisoprene at 230 K as a function of molecular weight. The line corresponds to Eq. 2.15*

As can be seen in Fig. 2.9 and 2.10, the α-relaxation contribution from long chains is nearly independent on molecular mass, but for low molecular masses (c.a. below 20 000 g/mol) it is shifted to higher frequencies and slightly broader. Because the rather small length scale involved in the segmental dynamics (around a nanometer) [35,36] it is expected that for a relatively low molecular weight sample, as PI-3, there would be contributions to the α-relaxation with different time scales originated because the presence of chains of different lengths. This could explain the fact that the α-relaxation peak of the PI-3 sample is slightly broader than that of a high molecular weight one, the PI-82 for instance (see Figure 2.9). Thus, in order to take this small effect into account we decided to describe the α-relaxation of the PI-3 sample as a superposition of different contributions. The contribution to the α-relaxation from a single chain of molecular weight M is assumed to be of the HN type (Eq. 1.51), with intensity proportional to the number of units (segments) in the chain, i.e. proportional to M. Under this assumption, the whole α-relaxation would be given as follows:

$$\epsilon_\alpha(\omega) = \int \frac{\Delta\epsilon(M)}{(1 + (i\,\omega\,\tau_{HN})^\beta)^\gamma} g(M)dM \tag{2.16}$$

$$= \frac{\Delta\epsilon_\alpha}{M_n} \int \frac{M}{(1 + (i\,\omega\,\tau_{HN})^\beta)^\gamma} g(M)dM \tag{2.17}$$

where g(M) is a Gaussian-like distribution introduced to take into account the effects of the actual molecular weight distribution of the sample:

$$g(M) = \frac{1}{\sqrt{2\,\pi\sigma}} \exp\left(-\frac{(M-M_n)^2}{2\sigma^2}\right) \tag{2.18}$$

$$\sigma = M_n\sqrt{\frac{M_w}{M_n} - 1} \tag{2.19}$$

g(M)dM is the number density of chains with molecular weight M, $\Delta\epsilon_\alpha$ is the total dielectric strength associated to the α-relaxation, and $1/M_n$ is just a normalization factor. The parameters β and γ in Eq. 2.17 were taken form the fitting of the α-relaxation losses of a high molecular weight sample, PI-82, ($\beta = 0.71$, $\gamma = 0.50$), i.e. the shape of each component has been assumed to be that obtained from the experiment in a sample with a high molecular weight and a narrow distribution. For such a sample no differences between the contributions of distinct chains are expected (see Figure 2.10).

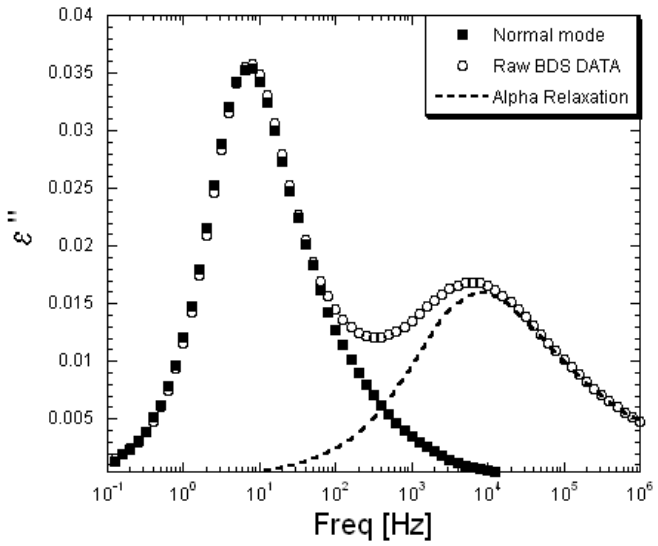

Figure 2.11 : *Resolved normal of PI-3, the dotted line represents the modelled contribution of the α-relaxation.*

Furthermore, we can note that for this sample, the α-relaxation is very well resolved from the normal mode and, therefore, its shape can be accurately characterized. Moreover, according to Eq. 2.15, the following expression for $\tau_{HN}(M)$ was used, $\tau_{HN}(M)/\tau_{HN}(\infty) = [1+(10000/M)^2]^{-1}$, where a value of $\tau_{HN}(\infty) = \tau_{HN}(82000)$ is a good approximation. In order to avoid the unphysical asymptotic behavior ($\epsilon'' \propto \omega^\beta$) given by the HN equation at very low frequencies, the physical asymptotic behavior ($\epsilon'' \propto \omega$) was imposed for frequencies two decades lower than that of the peak loss frequency. This cut-off frequency was chosen because is the highest cut-off frequency allowing a good description of the α-relaxation data from the high molecular weight PI samples.

The resulting curve is depicted in Fig. 2.11 as a dotted line. The value of $\Delta\epsilon_\alpha$ (single adjustable parameter) has been selected to fit the experimental data above f=5*10e4 Hz, where no appreciable contributions from the normal mode would be expected. After calculating the

α-relaxation contribution, the normal mode contribution can be completely resolved by subtracting it from the experimental data. The so obtained results are depicted in Figure 2.11 for PI-3.

3 Large scale Dynamics

The large chain-dynamics of linear polymers is one of the basic and classical problems of polymer physics, and thereby, it has been the subject of intensive investigation, both experimentally and theoretically, over many years [15, 16, 19, 37–41]. Despite of the broad range of models and theoretical approaches existing in the literature there are many aspects of the problem that remain to be understood (see refs. [16, 17, 19, 41] and references therein). Most of the current investigations are devoted to the problem of the dynamics of highly entangled polymer melts with different architectures and topologies, and to the rheology of polymer systems of industrial relevance [16, 42, 43]. Concerning the chain-dynamics of unentangled polymers, it is generally assumed that the well-known Rouse model [17] provides a suitable theoretical description. The Rouse model represents a linear chain as a series of beds and springs subjected to entropic forces in a medium with a constant friction. It has been first developed to describe the dynamics of polymer solution in a theta solvent. Although this simple approach obviously fails in describing the melt dynamics of long chains at longer times, the Rouse model is also used for describing the fastest part of the response of these long chains and thereby it is a common ingredient of all available model and theories. In the past, the validity of the Rouse model has ever been instigated by means of different experimental techniques and also by molecular dynamics simulations. But as already mentioned in the previous section, a full and detailed test of the Rouse model is challenging because in unentangled polymer melts the segmental dynamics (α-relaxation) contributions overlap significantly with the high-frequency components of the chain dynamics. This fact, among others, restricts the use of rheology experiments to test accurately the Rouse model on unentangled polymer chains. It is very hard to obtain rheology data of unentangled polymers in the melt. This is due to the rapid relaxation times of the material and the broad spread of the effect of more local molecular mechanisms that affect the stress relaxation modulus at higher frequencies. After a theoretical introduction, we will show how we have tested in full detail the Rouse model using both rheology and BDS.

3.1 Test of the Rouse model

— **Choice of the sample: Working below M_e**

The Rouse model describe the dynamics of unentangled polymers only. Therefore it is important to characterize its domains of application. As we will see below, the use of the time temperature superposition (TTS, see next paragraph) to create master curves in rheology is questionable. Figure 2.12 represents the master plot obtained for PI-82 from different temperatures T=[40, 20, -15, -30, -50]ºC (each represented by a different color) shifted to the reference temperature of -50ºC. Master curves permits to obtain the full rheology of the polymer. At low frequencies we can see the Maxwell zone ($G' \propto \omega$,$G'' \propto \omega^2$). Then, the elastic plateau, where G'>G", is well defined and the polymer is therefore entangled. After the plateau, the Rouse zone is characterized by $G' \propto G'' \propto \omega^{1/2}$. Rheology allows measuring a value of the molecular weight of entanglement M_e by measuring G_n^0, value of G' at the minimum of $\tan(\delta)$ (around the middle of the elastic plateau) [21]. This measurement is made at one temperature, and therefore no master curve is needed to get the value of G_n^0. According to reference [16]:

$$M_e = \frac{\rho RT}{G_n^0} \tag{2.20}$$

where ρ=0.9 g/cm^3 is the density, R = 8.32 J/K/mol is the ideal gas constant and T is the temperature of measurement. Using the value obtained from Fig. 2.12: $G_n^0 = 2.10^5$ Pa, we obtain a value of M_e=9 kg/mol.

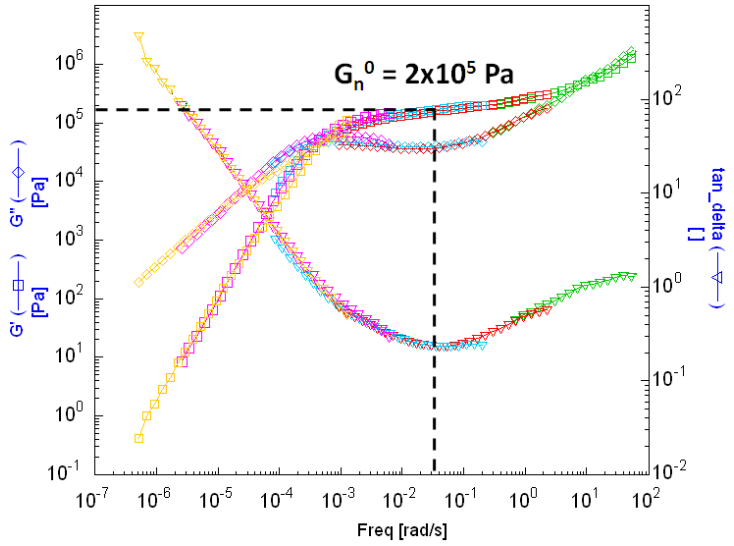

Figure 2.12 : *Master curve of PI-82 at the reference temperature of -50°C*

The dielectric normal mode reflects the fluctuations of the end-to-end vector and is dominated by the slowest chain normal mode. As higher modes are scaled and shifted to higher frequencies, the timescale of the normal mode peak, $\tau_N = \frac{2\pi}{f_N}$ (where f_N is the frequency of the maximum of the peak), measured by BDS provides a rather direct access to the Rouse time τ_1 when Rouse theory is fulfilled. Using these values of τ_N at 230 K we have checked whether below the molecular weight between entanglements the Rouse model predictions concerning the molecular weight dependence of the slowest relaxation times ($\tau_1 \propto M^2$) is verified. In Fig. 2.13 we present the values of the ratio τ_N/τ_α as a function of the molecular mass. The ratio between the longest relaxation time and the value of τ_α obtained at the same temperature in the same experiment is the way used trying to remove the possible variation in τ_N arising from the monomeric friction coefficient, which can be assumed as straightforwardly related with the changes in the glass transition temperature, and hence, with the noticeable effect of end chain groups in the segmental dynamics. Fig. 2.13 shows that below a molecular weight of around 7 000 g/mol the data scales approximately with M^2. This is just the Rouse model prediction, i.e., what is deduced from Eq. 1.34 for low-p values where the following approximation holds. This value is intermediate between that of the molecular mass between entanglements (M_e=9 kg/mol) obtained by rheology and that measured from neutron scattering experiments M_e=5 kg/mol [44].

Once we have confirmed the range of molecular masses where the molecular weight dependence of the longest relaxation time verifies Eq. 1.34, we will test if the whole dielectric normal mode conforms the Rouse model predictions. We have selected the sample PI-3 for this test because, on the one hand, it has a molecular weight sufficiently below of the molecular weight between entanglements (so all the molecular masses of the distribution are below M_e and, on the other hand, it shows a normal mode that is rather well resolved from the segmental α-relaxation contributions to the dielectric losses. Using higher molecular weight samples yield the possibility that the high molecular weight tail of the distribution was above the entanglement molecular weight. On the contrary, for lower molecular weight samples the stronger superposition of the normal mode and the α-relaxation will make the comparison less conclusive (see Fig. 2.9). For the test, we have taken the data recorded at a temperature of 230 K where the normal mode contribution is completely included within the experimental frequency window, being at the same time the α-relaxation contribution also well captured and then subtracted (see previous

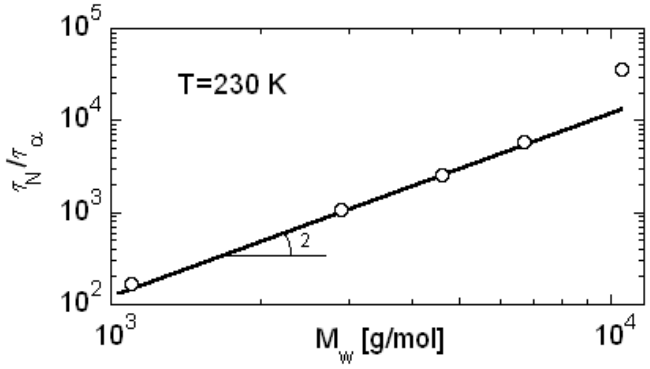

Figure 2.13 : *Ratio τ_N/τ_α , as a function of the molecular weight at 230 K. Solid line represents the behavior predicted by the Rouse model where $\tau_N = \tau_1 \propto M^2$.*

section and Figure 2.11).

— Time temperature superposition (TTS)

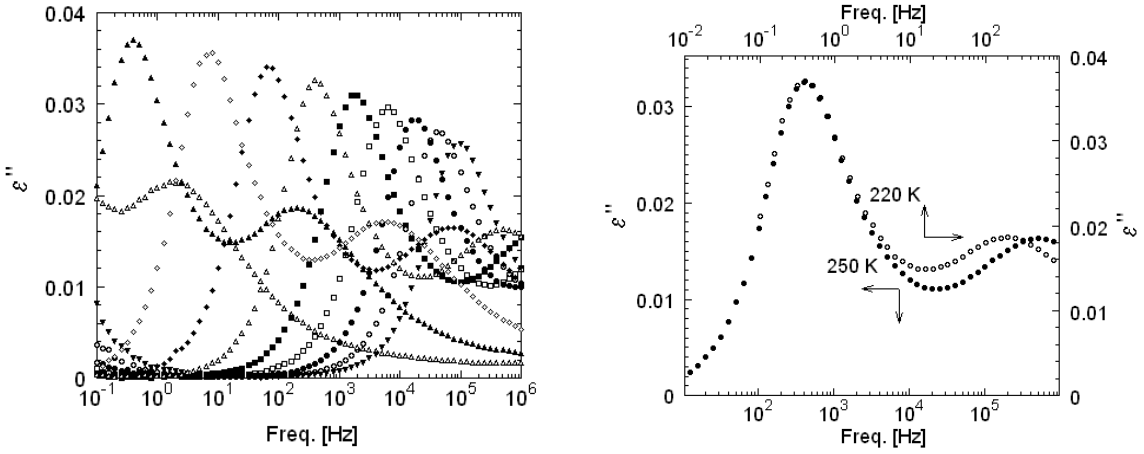

(a) *Dielectric spectra of PI3 from 220K (left) to 300K (right) $\Delta T = 10K$.*

(b) *Comparison of normal mode and α-relaxation frequency shifts for PI3 when temperature is changed from 220 K to 250 K.*

Figure 2.14 : *Shift of the dielectric response of PI-3 with temperature*

Figure 2.14 a shows the high level of accuracy obtained by means of the present BDS experiments when measuring the rather weak dielectric relaxation of a PI-3 sample, for both the normal mode and the α-relaxation. From simple inspection of the data it is apparent that the normal mode peak shifts by changing temperature without any significant change in shape (time temperature superposition is verified for this process), which is one of the predictions of the Rouse model (see eq. 1.40). However, it is also evident that the shift of the normal mode peak is distinct than that of the α-relaxation one, i.e. the TTS fails for the complete response. [45]. This fact is illustrated in Figure 2.14 b where data at two temperatures where both processes are clearly visible in the frequency window are compared. For this comparison the axes were scaled (by a multiplying factor) in such a way that the normal peaks superimpose. Whereas the superposition in the normal mode range is excellent, the same shift makes the alpha

relaxation peak positions to be about half a decade different. The temperature dependance of the normal mode peak can be described by Williams-Landel-Ferry (WLF) [30] equation:

$$log(a_T) = \frac{C_1(T - T_{ref})}{T - T_{ref} + C_2} \tag{2.21}$$

When considering the temperature dependence of the shift factor we found that, whereas for high molecular masses (above that between entanglements) the WLF parameters are the same within uncertainties (WLF parameters with T_g as the reference temperature $C_1 = 30.2 \pm 0.7$ and $C2 = 57.0 \pm 0.2K$), for lower molecular weight samples the value of C_1 remains the same but C_2 becomes noticeably smaller, being 49.2 K for PI-3. This is likely related with the significant variation of Tg in the low molecular range (see Table 2.1).

The data resulting from the rheology experiments performed on a PI-3 sample of 1.3 mm thickness using two parallel plates of 8 mm diameter are shown in Figure 2.15. To produce this plot a master curve at a reference temperature $T_{ref} = 230$ K was built imposing the horizontal shift factor a_T determined from BDS (see above) and a vertical shift factor b_T=T_{ref}/T. Curves have been measured at 215, 220, 225, 230 and 240K, each color represent a temperature. It is apparent that the superposition so obtained is good in the terminal relaxation range, although at the highest frequencies, where the contributions of the segmental dynamics are prominent, the data superposition fails clearly. The use of master curves in rheology experiments is a standard practice because of the rather limited frequency range and the general applicability of the TTS principle to the terminal relaxation range. However, the presence of the segmental dynamics contribution at high frequencies when approaching T_g could make the application of TTS questionable because the different temperature shifts of global and the segmental dynamics (see above). Thus, using rheology data alone the high frequency side of the terminal region could be highly distorted.

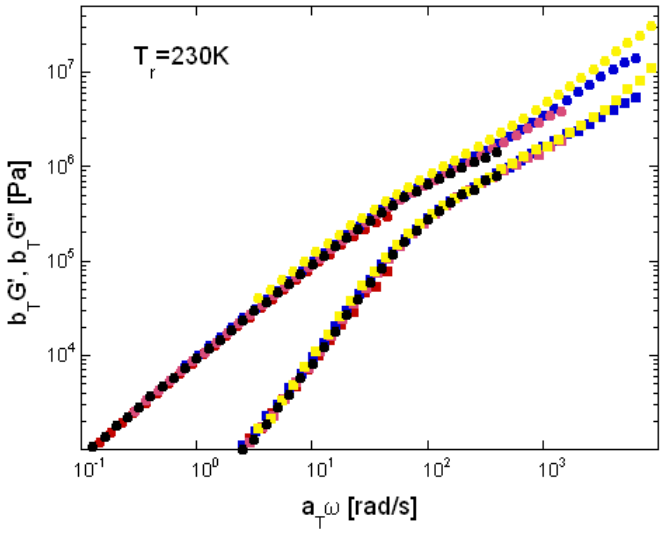

Figure 2.15 : *Rheological master curve of PI-3(reference temperature T_r =230 K) of the real:* ■ *and imaginary:* • *parts of the shear modulus.*

— Determination of the bead size

For using Eq. 1.45 we need the previous determination of N, which is not known a priori, as it requires the estimation of the bead size. Adachi and co-workers [46] estimated the bead size of PI on the basis of an analysis of the segmental relaxation in terms of a distribution

of Debye relaxation times. These authors suggested that a PI bead would contain about 7 monomers. However, a generally accepted approach is to consider that the bead size would be of the order of the Kuhn length, b_k. [47] The literature value of b_k for PI is 0.84 nm, [13] which corresponds to a molecular mass of the Kuhn segment of 120 g/mol. This means that a Kuhn segment would contain about 1.5 monomers, about a factor of about 5 less than Adachi et al. estimated. On the other hand, recent results has evidenced that the α-relaxation in the glass transition range probes the polymer segmental motions in a volume comparable to b_k^3. [35, 48] Thus, we will introduce a "segmental" Rouse time $\tau_S = \tau_{p=N}$, which apparently have not a clear physical meaning (the fastest Rouse time would be p=N-1) but it can be related with the so-called characteristic Rouse frequency ($W = 3k_bT/(\xi b^2)$) as $\tau_S^{-1} = 4W$. Nevertheless, τ_S is here used as a convenient parameter for the further analysis. We can identify τ_S at T_g with the α-relaxation time determined at this same temperature, i.e. $\tau_S(Tg)$=5 s. In this way, by using the WLF equation describing the temperature dependence of the normal mode peak, the obtained value of τ_S at 230 K would be 1.1*10e-4 s. Using this value and that obtained for τ_1 from the normal peak maximum in Eq. 1.34 a value of N=24 results. Note that according with this value the bead mass would be around 121 g/mol in very good agreement with literature results for the Kuhn segment mass, [13] and consequently the corresponding bead size will be nearly identical to b_k.

— **Monodisperse system**

Thus, in order to test the validity of the Rouse model in describing the dielectric normal mode relaxation data we assumed N=24 in Eq. 1.45, which would be completely predictive, except in an amplitude factor, once the slowest relaxation time τ_1 was determined from the loss peak maximum. The so calculated curve is shown as a dashed line in Figure 2.16. It is very clear that the calculated curve is significantly narrower than the experimental data, not only at high frequencies where some overlapping contribution from the α-relaxation could exists, but more importantly also in the low frequency flank of the loss peak. This comparison evidence clearly that the experimental peak is distinctly broader than the calculation of the Rouse model based in Eq. 7, confirming what was already envisaged in Figure 7a of ref. [41]. Nevertheless, an obvious reason for this discrepancy could be the fact that the actual sample has some (small) polydispersity. Despite of the fact that PI samples with a low polydispersity (2.1) were chosen, even samples obtained from a very controlled chemistry contains a narrow distribution of the molecular weights, which was not considered in the previous calculation.

— **Introduction of polydispersity**

Now, we are in a situation where it becomes possible to perform a detailed comparison between the experimental normal mode relaxation and the calculated Rouse model expectation. In order to incorporate the small sample polydispersity, the response expected from the Rouse model has been calculated as a weighted superposition of the responses corresponding to chains with different molecular weights. Since the molecular masses of the chains in the PI-3 sample are all below the molecular weight between entanglements, the molecular weight dependence of τ_p will be that given by Eq. 1.31 for all of the different chains. For calculating $\tau_p(M)$ we have used in Eq. 1.31 a common value τ_s irrespective of the molecular weight of the particular chain. Furthermore, we calculated $\tau_1(Mw)$ as the reciprocal of the peak angular frequency of the experimental normal mode of this sample.

In this way the Rouse model remains completely predictive and the corresponding dielectric response to be compared with normal mode contribution from the actual sample will be given

by:

$$\epsilon''_N(\omega) = \frac{\Delta\epsilon_N}{M_n} \int M \frac{2b^2}{N} \sum_{p:odd}^{N-1} cot^2\left(\frac{p\pi}{2N}\right) g(M) dM \tag{2.22}$$

where the contribution to the normal mode from a given chain is proportional to the chain dipole moment (to the end-to-end vector), and thus again proportional to M.

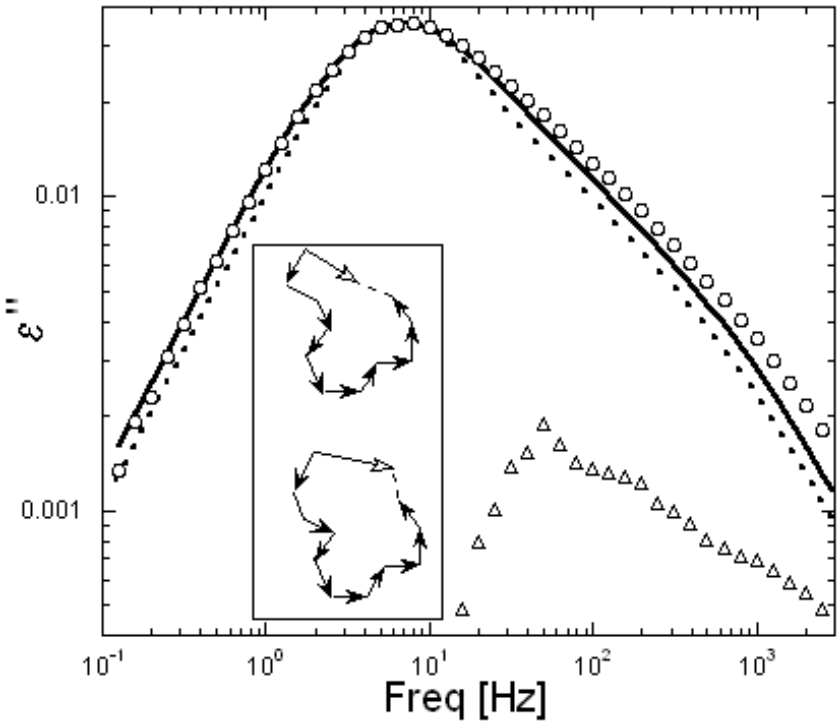

Figure 2.16 : *Resolved normal mode relaxation of PI-3 sample. The lines represent the behaviour predicted by the Rouse model including for the actual sample polydispersity (solid line) and without it (dotted line). Triangles correspond to the difference between the experimental losses and the Rouse model predictions. The inset shows schematically how the presence of configuration defects allows fluctuations of the whole chain dipole moment without variation of the end-to-end vector.*

As can be seen in Figure 2.16 (solid line), the sum over all the modes and all the molecular weight provides a satisfactory description of the experimental dielectric losses, namely at frequencies around and above the peak. The excellent agreement evidences that taking into account the (small) polydispersity of the sample under investigation is necessary to provide a good description of the dielectric normal mode contribution by means of the Rouse model, without any adjustable parameter other than the Rouse time, which (for the average molecular mass) is essentially determined from the reciprocal of the maximum loss angular frequency.

— BDS and rheology in the same experiment

Once we have found that the Rouse model can account accurately for the chain dynamics as observed by dielectric spectroscopy, the question that arise is if using the very same approach it would be possible to account also for other independent experiments, namely rheology. A key point to perform such a test is to be sure that all the environmental sample conditions remains the same. To be sure about this, we performed simultaneous dielectric and rheology experiments at 230 K. The sample thickness was smaller to balance the data quality of both dielectric and rheological results. We found that a thickness of 0.9 mm using two parallel plates

of 25 mm diameter provides a rather good compromise. The output of these experiments at 230 K is shown in Figure 2.17. Despite of the very different geometry used, the rheological

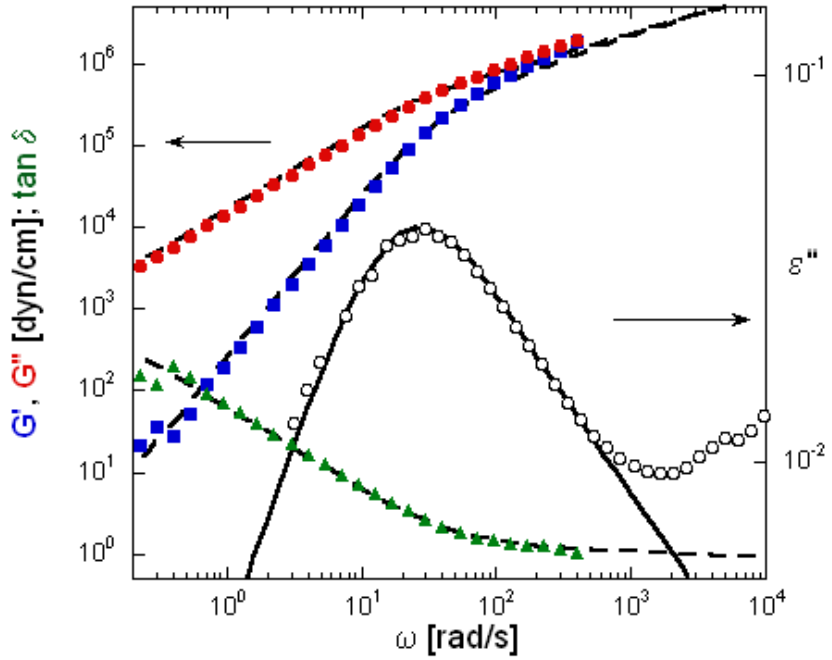

Figure 2.17 : *Simultaneous rheology (G': ■, G": •, tan(δ) : ▲) and BDS experiments (ϵ": ○) on PI-3 at 230 K. Lines correspond to the description obtained using the Rouse model, with a single set of parameters, for all the data sets.*

results are in close agreement with those obtained before. In this simultaneous experiment, the dielectric normal mode is clearly resolved so the peak position defining the time scale can be determined with low uncertainty, although again the accuracy of the dielectric relaxation data is not so good as that obtained in the data presented before. Nevertheless, this experiment will be essential in testing the ability of the Rouse model in accounting simultaneously for both the dielectric and rheology signatures of the whole chain dynamics. The approach used was to determine τ_1 from the dielectric losses, according with the description used above that is able to accurately account for the complete dielectric relaxation spectrum, and to use a similar approach to generate the corresponding rheology behavior. Thus, the only unknown parameter needed to perform the comparison with the experimental G'(ω) and G"(ω) data will be G_∞ (the high frequency limit of the modulus in terminal zone), which in fact it is not needed for calculating tan (δ)= G"(ω)/G'(ω). The equations used were obtained from Eq. 1.46 and 1.47 following the same procedure that the one from BDS:

$$G'(\omega) = \int \frac{G_\infty}{M_n} \sum_{p=1}^{N-1} \frac{\omega^2\tau_p^2/4}{1+\omega^2\tau_p^2/4} g(M)dM \tag{2.23}$$

$$G''(\omega) = \int \frac{G_\infty}{M_n} \sum_{p=1}^{N-1} \frac{\omega\tau_p/2}{1+\omega^2\tau_p^2/4} g(M)dM \tag{2.24}$$

The results of the comparison between the calculated responses and the experimental data are shown in Fig. 2.17. A satisfactory description is obtained for G'(ω) and G"(ω) by means of the same Rouse model parameters used in describing the dielectric normal mode. More interestingly, the description of tan(δ) is also rather good, for which the previous calculation is

compared with the experimental data without any arbitrary scaling. Despite the good agreement obtained, it is worthy of remark that the ability of rheology experiments for checking the Rouse model in full detail is much more limited than the dielectric one because both the narrower frequency range accessible and the stronger overlapping of the segmental dynamics contributions.

— **Discussion**

Despite the overall good agreement, Figure 2.16 evidences that the experimental losses are slightly larger (maximum difference about 10%) than the Rouse model prediction in the high frequency side. Although one could consider that this is simply due to the contribution of the overlapping α-relaxation that has not been properly subtracted, the fact that the maximum of these extra losses intensity occurs at frequencies two decades above the segmental relaxation peak (see triangle in Figure 2.16) seems to point out to other origin. In agreement with this idea, that the frequency distance above the NM peak where the Rouse model description starts underestimating the experimental losses does not depend much on temperature. Thus, extra contributions from some chain-modes are detected in the dielectric normal mode. In fact the peak intensity of the extra losses occurs at the position of the p=3 mode (see triangles in Fig. 2.16), i.e. the second mode contributing to the dielectric normal mode. All this might evidence the fact that the Rouse model approach ignores several aspects of the actual chain properties as that of the chain stiffness [49] or the lower friction expected to occur at the chain ends [50]. In this context it is noticeable that the contribution from the α-relaxation extended considerably towards the frequency range where the normal mode is more prominent. In fact the cut-off frequency used for describing the α-relaxation in Fig. 2.11 was close to 100 Hz, i.e, where the differences between the normal mode response and the Rouse model are more pronounced. This result indicates that for most of the high-p chain modes the segmental relaxation is not completed. This is in contrast to the assumptions of the Rouse model where it is considered that all the internal motions in the chain segment are so fast that their effect can be included in the effective friction coefficient. It is noteworthy that a higher frequency cut-off would be not compatible with the experimental data of the high molecular weight PI samples, and would produce a more prominent underestimation of the dielectric normal mode losses. On the contrary, a lower frequency cut-off would improve slightly the agreement between the normal mode data and the Rouse model prediction but would imply and higher coupling between the segmental dynamics and the whole chain motion. Small deviations from the Rouse model predictions have also been reported from numerical simulations, molecular dynamics calculations and detected by neutron scattering experiments, [41,49,51,52] although these deviations become evident only for relatively high p-values. Note, that dielectric experiments being mainly sensitive to the low-p modes can hardly detect such deviations. On the other hand, experiments in solution have also evidenced differences between the experimental data and the predictions of the Rouse model, [53] which were tentatively attributed to chain overlapping effects since the deviations occur above a given concentration. Nonetheless, there are also possible experimental sources for the small extra high frequency contributions to the dielectric losses as it would be the presence in the actual polymer of a fraction of monomeric units others than the 1,4-cis ones (up to 20%). The motion of such units, having a much smaller component of the dipole moment parallel to the chain contour, would produce small amplitude fluctuations of the whole dipole moment uncorrelated with the fluctuations of the end-to-end vector (see inset in Figure 2.16). The chain motions around these 'configuration defects' would generate a relatively weak and fast contribution to the dielectric normal mode that could explain the experimental data. Unfortunately, the actual sample microstructure prevents to definitively address whether the deviations from the Rouse model predictions are actually indicative of its limitations.

3.2 Dynamics regimes as a function of the molecular weight and effects of entanglement

As shown in the previous section, the polymer dynamics follows different regimes as a function of the molecular weight and molecular weight distribution. Abdel-Goad et al [54], using rheology measurements coupled with an empirical Winter-relaxation BSW-model obtained three different exponents (1, 3.4 and 3) in the molecular weight dependence of the zero shear viscosity. Previous BDS studies on the molecular weight dependence of the normal mode relaxation time showed a crossover from the unentangled dynamics to the entanglement regime [37–39, 39, 55]. However, none of BDS experiment has been able to access the crossover to exponent 3 expected by the pure reptation theory which, as aforementioned, has been detected for the viscosity. In this section, we will detail how careful BDS experiments allow detecting the two different crossovers from the Rouse up to the pure reptation regime. Entanglement effects in BDS spectra will be also analyzed. Finally, the possible influence of the narrow molecular weight distribution of the samples on the dielectric loss shape will be discussed.

— **Low molecular weight**

As can be seen in Fig. 2.9 the fast variation of the normal mode relaxation peak prevents detecting it in the frequency window at 250 K for molecular weight higher than 80 kg/mol. Thus, we will first focus the analysis on the samples with lower molecular weight. As already mentioned, for low molecular masses the changes in the local friction coefficient (arising because the significant changes in the end chain groups accompanying the changes in molecular weight) influences the relaxation time. Therefore, just as in Fig. 2.13, the ratio of the normal mode time scale to that of the α-relaxation was evaluated (Fig. 2.18). To increase the plot sensitivity

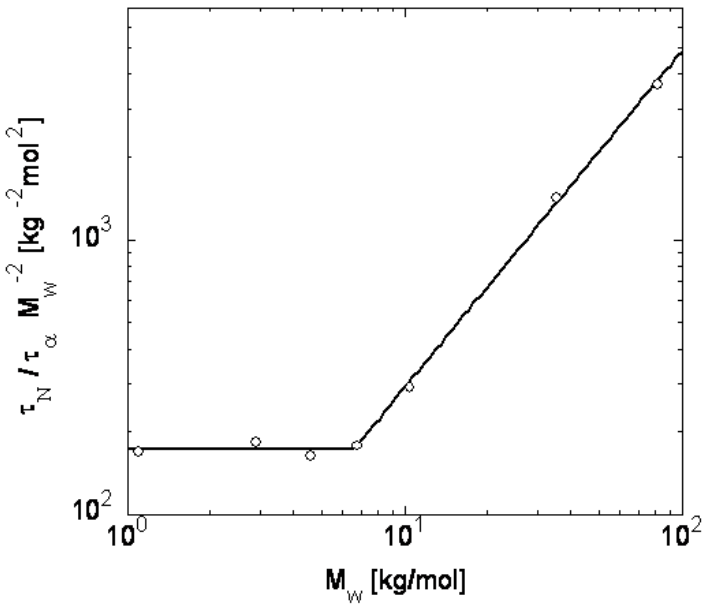

Figure 2.18 : *Longest and segmental relaxation time ratio as a function of the molecular weight at 250 K. The vertical axis is scaled by M^2 to emphasize the transition from the Rouse to the intermediate regime. The solid line corresponds to the description of the data with a sharp crossover between two power law regimes with different exponents.*

to changes between the different regimes a factor of M_w^{-2} has been applied to the ratio between the characteristic times (reciprocal of the peak angular frequency) of the two relaxation processes. As already mentioned, the M_w^2 dependence expected for unentangled polymers on

the basis of the Rouse theory is fulfilled for samples with molecular weight below 7 kg/mol. The exponent describing the higher molecular mass range considered in this plot was 3.2 ± 0.1 which is distinctly lower, but close, to the 3.4 usually found in rheological experiments [21]. It is noteworthy that imposing this exponent to fit our data will result in a higher value of the crossover molecular weight, thus increasing the discrepancy with the reported/admitted value of $M_e = 5$ kg/mol measured by neutron scattering [44]. It is noteworthy that, as it is well know, the ratio τ_N/τ_α will change with temperature [56]. Nevertheless, the previous results will not change significantly using data at other temperatures because the changes in the value τ_N/τ_α will be very similar for all the samples having different molecular weights and, consequently, the resulting molecular weight dependence would be unaltered.

— **High molecular weight**

After analyzing the molecular weight dependence of the end-to-end fluctuations in the low and moderate molecular weight range, now we will focus the attention in the highest accessible molecular weights. In the high molecular weight range, the comparison among the different samples has to be performed at a significantly higher temperature due to the dramatic slowing down of the chain dynamics. The more suitable temperatures are those where the normal mode loss peak of the sample with the highest molecular weight occurs in the low frequency range of the experimental window. An additional factor that have to be taken into account is the fact that by increasing temperature the conductivity contribution to the dielectric losses becomes more prominent. The conductivity contribution appears as a ω^{-1} increasing of the dielectric losses and is due to impurity in the sample. This is an important issue even for high quality samples when the experiments require accessing to the low frequencies at temperatures far above T_g. This situation is illustrated in Fig. 2.19 for the raw data of the PI sample having the highest investigated molecular weight. It is apparent that at 340 K the normal mode peak can

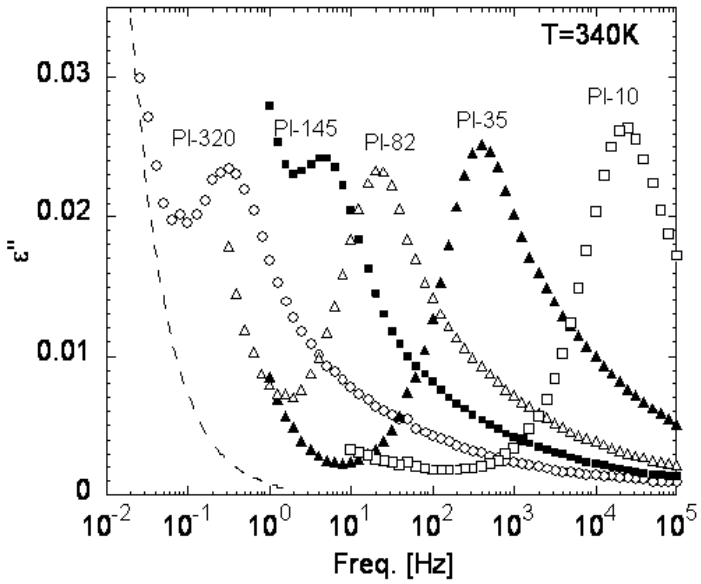

Figure 2.19 : *Normal mode of the high molecular weight PI samples. Dashed line represents the calculated conductivity contribution to the dielectric losses for the PI-320 sample*

be well resolved from conductivity for this sample but it would be hard to resolve the normal mode relaxation at this temperature for a sample with a significantly higher molecular weight. Furthermore, increasing temperature would not improve the situation since the overlapping of the conductivity contribution with the normal mode relaxation will also increase. This is

a serious limitation of the dielectric methods for investigating the slowest chain dynamics in highly entangled systems. Nevertheless, as shown in Fig. 2.19, resolving the normal mode peak was possible for all the samples investigated although the contribution from conductivity will increase the uncertainty in the peak position for the samples with very high molecular weight. Figure 2.20 shows the molecular weight dependence of the slowest relaxation time for the high molecular weight regime obtained from the data presented in Fig. 2.19. Trying to increase

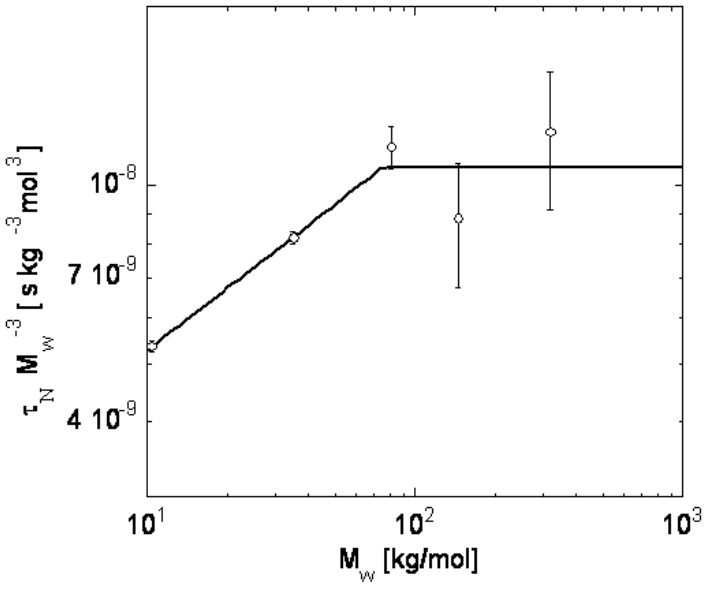

Figure 2.20 : *Longest relaxation time from the higher molecular weight PI samples. The graph is scaled to M^3 to emphasize the crossover from the intermediate to the reptation regime. The solid line corresponds to the description of the data with a sharp crossover between to power law regimes with different exponents.*

the sensitivity of the plot to possible changes in behavior the data have been multiplied by M_w^{-3}, which would produce a molecular weight independent result for a pure reptation regime. Despite of the uncertainties involved, our results evidence that for the highest molecular weight samples the molecular mass dependence approach the pure reptation regime expectation. The line in Fig. 2.20 corresponds to a crossover from and exponent 3.35 to a pure reptation-like regime. The small difference between this exponent and that obtained above from Figure 2 is more likely due to the fact that the sample with the lower molecular weight considered in Fig. 4 have a significantly lower glass transition temperature, an effect not been considered in Fig. 2.20 . The crossover molecular weight obtained from Fig. 2.20 is 75 ± 10 kg/mol, i.e. it corresponds to about 15 times M_e. This value is slightly lower than that determined from viscosity data [54].

— **Discussion**

The results previously described showed three different regimes for the molecular weight dependence of the chain longest relaxation time in PI, one below 7 kg/mol following the Rouse model prediction as expected for a non-entangled polymer melts, other above 75 kg/mol where the reptation theory provides a good description and an intermediate one, where the polymer is entangled but other mechanisms (like contour length fluctuations or constraints release) in addition to reptation would control the whole chain dynamics. In the rheological experiments above referred [54] it was shown that the viscosity of high molecular weight PI samples conforms well the reptation theory predictions. Thus, we decided to test up to what extent the pure reptation theory is able to describe the normal mode relaxation spectrum of the highly

entangled PI samples. This test can evidence the ability of the reptation theory to capture the main features of the slowest chain dynamics, despite the well documented failure of the reptation theory in accounting for the whole chain dynamics, even in the high molecular weight range. This is clearly evidenced by the reported mismatching of the normalized dielectric and rheological spectra [57]. To this end, we compared our experimental data on the high molecular mass samples with the corresponding reptation theory predictions for the dielectric permittivity. This relation is similar to the one obtained in the frame of the Rouse model (Eq. 1.45. As the chain are long, N>p and the cot^2 can be developed in $1/p^2$. By analogy, the value of $\tau_p = \tau_1/p^2$ is replaced by τ_d/p^2 where τ_d is the disentanglement time (reptation time), which would correspond in good approximation to τ_N.

$$\epsilon''(\omega) \quad \propto \quad \sum_{p:odd}^{N-1} \frac{1}{p^2} \frac{\omega\,\tau_d/p^2}{1+(\omega^2\,\tau_d/p^2)^2} \tag{2.25}$$

Figure 2.21 shows the direct comparison between the experimental data for some of the samples investigated (symbols) having all of them the lowest available polydispersity index (1.05) and the pure reptation theory prediction (solid line). Both vertical and horizontal scaling factors have been applied to obtain a good matching of the peaks. It should be noted that the possible conductivity contributions to the normal mode relaxation were subtracted. The inset shows separately the data of the highest molecular weight sample because it has a markedly broader molecular weight distribution (polydispersity index 1.14). From Fig. 2.21 it becomes apparent

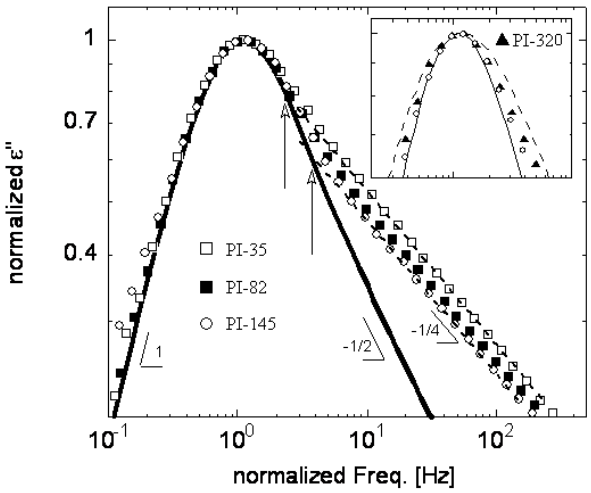

Figure 2.21 : *Comparison of the BDS data of high molecular weight (symbols) with pure reptation theory (solid line). Dashed straight line showing the ¼ power law behavior of the samples with PI-33 and PI-145 are also shown. The vertical arrows indicate the crossover frequency between both regimes. The inset presents for comparison the highest molecular weight data (PI-320) with a high polydispersity (1.14) with that of smaller polydispersity (1.04). The dashed line represents what would be the reptation theory expectation when a very crude approximation is used to account the effect of the molecular weight.*

that in the high frequency side of the loss peak deviations from the reptation predictions on the end-to-end vector fluctuations persist even for the highest molecular weight investigated. Whereas the high frequency behavior expected from the reptation theory is a power law with exponent -1/2, the experimental data present and exponent -1/4 (see Figure 2.21), which would be a signature of the relevance of chain contour length fluctuations at least in this high frequency side of the normal mode relaxation. Nevertheless, it is also clear that the range of these deviations reduce when increasing molecular weight. The vertical arrows in Fig. 2.21 shows that

a factor of 5 increasing in molecular weight makes the crossover frequency to increase in a factor of about 2. By inspection of the rheological data reported by Abdel-Goad et al, [54] it is also apparent that in the very high molecular weight range where the viscosity scales as predicted by reptation theory the terminal relaxation is far from being properly described by this theory. Eventually the normal mode description by the pure reptation theory could be obtained only at extremely higher molecular weights, for which, as aforementioned, the dielectric experiments will not be suitable for investigating the extremely slow chain dynamics. Concerning this, it has been shown [19] that for polyethylene the frequency dependence of the loss shear modulus verifies the reptation prediction only for a molecular weight as high as of 800 kg/mol, which for this polymer corresponds to about 400 times M_e, i.e., it would correspond to about 3000 kg/mol for PI. Taking the above-calculated shift of the crossover frequency into account, for this limiting molecular weight the crossover frequency would occur at around 20 Hz and the failure of the repetition theory description would be hardly detectable by using the same scale as in Fig. 2.21. This figure also shows that both the maximum and the low frequency side of the loss peak is well accounted by the reptation theory without any evident deviation, except for the sample having a broader distribution of molecular weight, which shows a distinctly broader normal mode peak (see inset of Fig. 2.21). This comparison evidences that the molecular weight distribution have a noticeable effect on the normal mode spectrum shape. We remind that the effect of the molecular weight distribution on the normal mode was properly accounted for in an unentangled PI sample by assuming that the contributions from chains in the sample with distinct molecular weight simply superimpose (see previous section on the Rouse model). When we tried the same approach with the higher molecular weight samples (dashed line in the inset of Fig. 2.21) it becomes evident that the situation for well-entangled polymers is different. Even by using the smallest polydispersity (1.04) the calculated response overestimates by far the broadening of the peak for the sample with highest polydispersity (1.14). Thus, for highly entangled polymers the effect of the molecular weight distribution on the normal mode is less evident than that observed in the unentangled polymer case. In fact, the complete disentanglement of a chain involves also the motions of the chains around, which would have a different molecular weight, being therefore the resulting time scale some kind of average of those corresponding to the ideally monodisperse melts. As a result the longest relaxation time in highly entangled melts should not dependent greatly on the molecular weight distribution provided it is not very broad.

Conclusion on the macroscopic properties

The aim of the macroscopic studies of polymer was to understand the main theories that describe the polymer dynamics before developing EFM based nano-characterization methods in order to test if these theories still holds at the nanosclae. We have studied two polymers: polyisoprene and poly(vinyl acetate).

Due to dipolar moment parallel to the chain backbone, PI exhibit a whole chain dielectric relaxation. This so-called normal mode can either be described by the Rouse or reptational tube theory for unantengled and entangled polymers respectively. We have chosen to work with PI samples having a molecular weight variating between 1 and 320 kg/mol in order to cover the range of applications of these two regimes. The first step of the work on PI was to study the Rouse model, well known since the fifties to describe rather correctly the whole chain dynamics of unentangled polymers. Using rheology, we have measured the molecular weight of entanglement M_e=9 kg/mol and chosen to study how the Rouse model could describe the normal mode response of a sample having a molecular weight of 2700 g/mol. Even if the Rouse model has been intensively investigated by different experimental techniques this study is still challenging because for unentangled polymer, contributions of the α-relaxation (a fast segmental relaxation related to dipolar component perpendicular to the chain backbone) overlap significantly with the whole chain dynamics. By decorelating the effect of the α-relaxation on the normal mode and introducing polydispersity, we showed that the Rouse model permits a good description of both rheological and Broadband Dielectric Spectroscopy (BDS) data. The small differences between theory and experiment are attributed to a defect of configuration: the sample is composed by 80% of the isomer cis.

Then, we have studied the different regime in the dynamics as a function of molecular weight. In agreement with other rheological data previously reported, we found two crossovers in the molecular weight dependence of the longest relaxation time. The first, around a molecular weight of 6.5 $\pm$ 0.15 kg/mol, corresponds to the end of the Rouse regime. Above the second at 75 $\pm$ 10 kg/mol we find a power law with exponent 3 as predicted by the De Gennes theory.

PVAc exhibits strong losses due to the segmental dynamics slightly above room temperature. Therefore it will be a good candidate to develop EFM based nano-characterization methods. The static value of the dielectric constant has been measured to 3 and 8 around room temperature and 70^{o}C, respectively. It forms phase separated domains when used has a component in a blend with PS. Preliminary results have shown that for a given temperature, the characteristic time of the α-relaxation (τ_α) measured by BDS is slightly faster for a blend of PVAc/PS than for a bulk of pure PVAc. One possible hypothesis to explain this faster dynamics could be related with the fact that BDS measure dielectric properties macroscopically, over the all sample, including the interfaces' regions between PVAc and PS having a different dynamics. Further research are needed to confirm these results and clearly states, in a quantitative way, about possible interface's effects.

Chapter 3

Electrostatic Force Microscopy, the Equivalent Charge Method and state of the art

Summary

This chapter is of the upmost importance because it details how the quantities measured by Electrostatic Force Microscopy (EFM) in chapters 4 and 5 are related with the dielectric permittivity ϵ of the sample. We will first give some generalities about Atomic and Electrostatic Force Microscopy. Then, we will define the electrostatic force and force gradient and explain how we are able to measure these quantities. In the second section of this chapter, we will detail the numerical simulation of the Equivalent Charge Method (ECM) that allows obtaining the value of the relative dielectric permittivity ϵ_r from the physical quantities measured experimentally. The importance of the other parameters of the experiment (tip radius, thickness of the sample, tip sample distance) and the sensitivity will be discussed. We will report first considerations about how to control the penetration of the field inside the sample.

1 Atomic and Electrostatic Force Microscopy

An Atomic Force Microscope (AFM) is composed of a cantilever with a sharp tip (probe) at its end that is used to scan the specimen surface. Typical geometric parameters of the cantilever are a length of 100 μm, a width of 20-40 μm and a thickness of 1-2 μm. The tip is located at the end of a cone having a length of about 10 μm and a radius variating from 20 to 150 nm (Fig. 3.1). In the dynamic mode, the cantilever (excited by a piezoelectric actuator) is oscil-

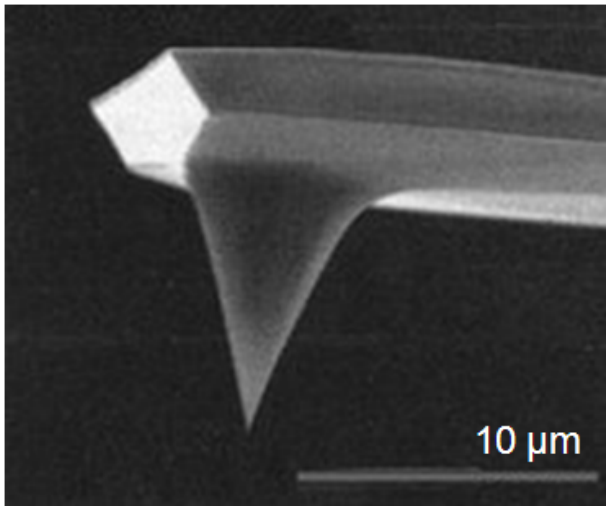

Figure 3.1 : *Typical AFM probe (image obtained by Scanning Electron Microscopy)*

lating at or close to its resonance frequency. The motion of the cantilever is usually measured using optic signals: A laser is reflected at the extremity of the cantilever and then measured by photodiodes. When the tip is brought into proximity of the sample surface, forces between the tip and the sample lead to a deflection of the cantilever. The cantilever can be modelized by a point mass spring system. The stiffness k_c is defined as the coefficient of proportionality between the force and the deflexion. In the absence of external fields, the dominant forces are the long range attractive Van der Waals interactions and the short range repulsive forces. The AFM has two important qualities:
- It permits to probe local nanoscopic properties.
- Its modularity allows creating new modes in order to measure specific properties.

Since the first development of the AFM in the contact mode by Binnig et al [1] in 1986, an impressive number of modes have been developed: lateral force microscopy, force modulation,

phase imaging, magnetic scanning force microscopy, scanning capacitance microscopy... These different modes allow measuring a wide range of properties in different environments (air, liquid, vacuum) making the AFM a commonly used technique in physics, chemistry and biology. Presently, two dynamics modes have emerged to measure the topography of a sample surface: the Amplitude Modulation (AM-AFM) and Frequency Modulation (FM-AFM). In AM-AFM the oscillation amplitude is used as a feedback parameter to measure the topography. Usually the tip is fixed and a piezoelectric actuator allows moving the sample in the x, y and z direction. The image is reconstructed from the z displacement of the piezoelectric necessary to keep constant the amplitude of vibration. In FM-AFM the cantilever is kept oscillating with a constant amplitude by fixing a small resonance frequency shift. This shift depends on the forces acting between tip and sample surface and serves as a feedback parameter for the formation of topographic images. FM-AFM has been developed in order to work under Ultra High Vacuum (UHV) where the quality factor is typically of the order of $Q \sim 10^4$, leading to an excessively long time constant and therefore to a non reasonable time of acquisition of a simple topography. Working with higher harmonics [58] permits to use the AM mode under vacuum, but most of the experiments in the air are still made in the AM mode whereas UHV is performed using FM.

1.1 Oscillation of the cantilever

The cantilever can be considered as a point mass spring oscillator, then the tip motion $z(t)$ can be described by second order differential equation:

$$m\ddot{z} + \frac{m\omega_0}{Q}\dot{z} + k_c\, z = F(z) + F_1\, cos(\omega\, t) \tag{3.1}$$

where F_1 and ω are the amplitude and angular frequency of the driving force. Q, ω_0, k_c and m are the quality factor, angular resonance frequency, stiffness and effective mass of the cantilever-tip system, respectively. F contains the tip surface interaction forces. When the cantilever is freely oscillating (F=0) Eq. 3.1 describes the motion of a force harmonic oscillator with damping. In this case, the solution is well known (see general review about AFM as [59, 60]) and has the form:

$$z = A_c\, cos(\omega\, t - \phi_c) + B\, exp(-t/\tau) cos(\omega_r\, t + \beta) \tag{3.2}$$

where A_c is the amplitude of the cantilever's motion, ϕ_c is the phase difference between the driving force and the cantilever motion. ω_r is the resonance frequency of the cantilever influenced by the damping effect. The first term is a steady solution ad the second term is a transient one. The transient term has exponential decaying time dependence with a constant time $\tau = 2Q/\omega_0$. This time constant could be a significant parameter for a high Q-value system as in vacuum where Q $\simeq$ 50 000 and $\tau \simeq$ 150 ms, leading to a time of acquisition of about six hours for a 256x256 pixels image. When the transient solution fades out, the sinusoidal motion of the cantilever is characterized by:

$$A_c = \frac{F_0}{m\left[(\omega_0^2 - \omega^2)^2 + (\omega_0\, \omega\, /Q)^2\right]^{1/2}} \tag{3.3}$$

$$tan(\phi_c) = \frac{\omega\omega_0}{Q(\omega_0^2 - \omega^2)} \tag{3.4}$$

At the resonance frequency, $A_c(\omega_0) = QF_0/k_c$. The resonance frequency with damping, ω_r is related to the free resonance frequency ω_0 by:

$$\omega_r = \omega_0 \sqrt{1 - \frac{1}{2Q^2}} \tag{3.5}$$

Let's now consider the total force F_T acting on the cantilever. For small displacements with respect to the equilibrium position z_0, F_T can be expressed as:

$$F_T = F_0 - \left(k - \frac{\partial F}{\partial z}\right)_{z_0} (z - z_0) \tag{3.6}$$

Then, Eq. 3.1 describes the motion of a harmonic oscillator with an effective spring constant k_e and resonance frequency defined by:

$$k_e = k_c - \left(\frac{\partial F}{\partial z}\right)_{z_0} \tag{3.7}$$

and

$$\omega_e = \sqrt{\frac{k_e}{m}} \tag{3.8}$$

The resonance frequency of a weakly perturbed harmonic oscillator depends on the force gradient of the interaction. A change Δf_0 in the effective resonance frequency induces a shift of the resonance curve, with a variation of the amplitude and the mechanical phase of the oscillator. The force gradient being positive, it decreases the effective spring constant of the cantilever and the actual resonance frequency. Fig. 3.2 represents the amplitude and phase (A_c,ϕ_c) of the cantilever observed freely or in presence of an attractive force in the case of small displacements.

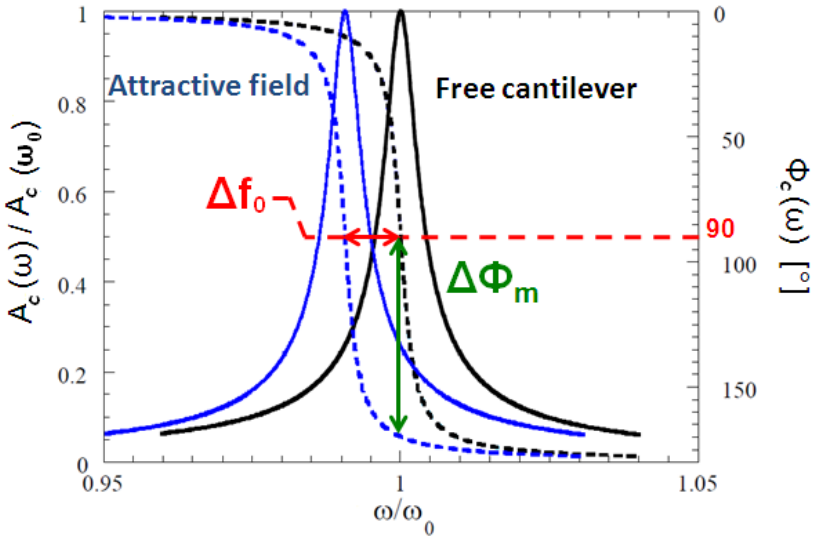

Figure 3.2 : *Amplitude (line) and phase (doted line) of the free cantilever and in presence of an attractive force gradient (curves shifted to lower frequency). Δf_0 and $\Delta\phi_m$ are proportional to the force gradient.*

When the force gradient is small compared to the cantilever spring constant ($\frac{\partial F}{\partial z} \ll k_c$), by developing Eq. 3.8 in Taylor series, it appears that the frequency shift Δf_0 is proportional to the force gradient:

$$\omega_e = \sqrt{\frac{k - \frac{\partial F}{\partial z}}{m}} \tag{3.9}$$

$$\cong \sqrt{\frac{k_c}{m}} + \frac{1}{2}\left(\frac{k_c}{m}\right)^{-1/2}\left(-\frac{1}{m}\right)\frac{\partial F}{\partial z} \tag{3.10}$$

$$\cong \omega_0 - \frac{1}{2}\frac{\partial F}{\partial z} \tag{3.11}$$

$$\omega_e - \omega_0 \cong \Delta\omega_0 = -\frac{\omega_0}{2k_c}\frac{\partial F}{\partial z} \tag{3.12}$$

$$\Delta f_0 \cong -\frac{f_0}{2k_c}\frac{\partial F}{\partial z} \tag{3.13}$$

Moreover, according to reference [58] the mechanical phase shift can be expressed as:

$$\Delta\phi_m \cong -\frac{Q}{k_c}\frac{\partial F}{\partial z} \tag{3.14}$$

We point out that although the force gradients can be detected either by measuring the frequency shifts or by measuring the phase shifts, we always chose in this work the measurement of frequency shifts to avoid the phase' saturation observed at high voltage (>10V).

1.2 Electrostatic force microscopy

a Expression of the force and force gradient in EFM

In EFM, we are always working at a relatively large value of the tip sample distance and there is no repulsive contact force between the tip and the sample. Moreover, van der Walls forces are negligible. Therefore, force between the tip and the sample F is purely electrostatic and can be defined as:

$$F = \frac{1}{2}\frac{\partial C}{\partial z}V^2 \tag{3.15}$$

where V is the the voltage difference between the tip and the sample and C the tip-sample capacitance. When a sinusoidal voltage is applied to the probe (with the sample holder grounded):

$$V^2 = [(V_{DC} - V_{cp}) + V_{AC}\sin(\omega_e t)]^2 \tag{3.16}$$

$$= (V_{DC} - V_{cp})^2 + 2(V_{DC} - V_{cp})V_{AC}\sin(\omega_e t) + V_{AC}^2\sin^2(\omega_e t) \tag{3.17}$$

ω_e is the electrical pulsation of the V_{AC} voltage. V_{cp} is the contact potential difference corresponding to the work function difference of the tip and the sample if the sample is conductive (or semi-conductive). When studying insulator, V_{cp} describe the work function difference of the tip and the conductive sample holder. In the frame of our experiments we did not observed any significant contact potential, thus in what follows we will assume V_{cp}=0. Using the formula of the reduction of the square:

$$V_{AC}^2\sin^2(\omega_e t) = V_{AC}^2\frac{1 - cos(2\,\omega_e\, t)}{2} \tag{3.18}$$

we obtain the expression of the electrostatic force:

$$F = F_{DC} + F_{\omega_e} - F_{2\omega_e} \tag{3.19}$$

with:

$$F_{DC} = \frac{1}{2}\frac{\partial C}{\partial z}\left[V_{DC}^2 + \frac{V_{AC}^2}{2}\right] \tag{3.20}$$

$$F_{\omega_e} = \frac{\partial C}{\partial z} V_{DC}\, V_{AC} \sin(\omega_e t) \tag{3.21}$$

$$F_{2\omega_e} = \frac{1}{4}\frac{\partial C}{\partial z} V_{AC}^2 \cos(2\omega_e t) \tag{3.22}$$

The same kind of expression is obtained for the force gradient G:

$$G = G_{DC} + G_{\omega_e} - G_{2\omega_e} \tag{3.23}$$

with:

$$G_{DC} = \frac{1}{2}\frac{\partial^2 C}{\partial z^2}\left[V_{DC}^2 + \frac{V_{AC}^2}{2}\right] \tag{3.24}$$

$$G_{\omega_e} = \frac{\partial^2 C}{\partial z^2} V_{DC}\, V_{AC} \sin(\omega_e t) \tag{3.25}$$

$$G_{2\omega_e} = \frac{1}{4}\frac{\partial^2 C}{\partial z^2} V_{AC}^2 \cos(2\omega_e t) \tag{3.26}$$

b What we are measuring

Measurements of the force or force gradient in the AM-AFM mode have been realized using the double-pass method (lift-mode) where the topographic information is obtained during the first pass and the electrostatic signals are acquired during the second pass. In the FM-AFM mode, the Phase Locked Loop (PLL) detects the shift in the resonance frequency due to the van der Walls interaction between tip and sample surface. This frequency shift serves as a feedback parameter for the formation of topographic images whereas the frequency shift due to the electrostatic interaction provides information about dielectric properties.

In this study, the raw signal is always the one coming from the photodiode. A_p and ϕ_p are the amplitude and phase of the signal measured by the photodiodes, respectively. Figure 3.3 summarized all the signals measured in EFM. In the next chapters of the thesis, we will distinguish two modes either working with a V_{DC} or V_{AC} voltage.

— **Working with V_{DC}**

When the mechanical excitation is turned off, the amplitude of the signal of the photodiode A_p gives a direct access to the electrostatic force. This signal (in volt) is related with the deflexion of the cantilever (in nm) via a factor of proportionality χ (expressed in nm/V). χ can be measured by realizing a force distance curve on a hard material. Therefore:

$$A_p = \frac{1}{\chi\, k_c} F_{DC} = \frac{1}{2\,\chi\, k_c}\frac{\partial C}{\partial z} V_{DC}^2 \tag{3.27}$$

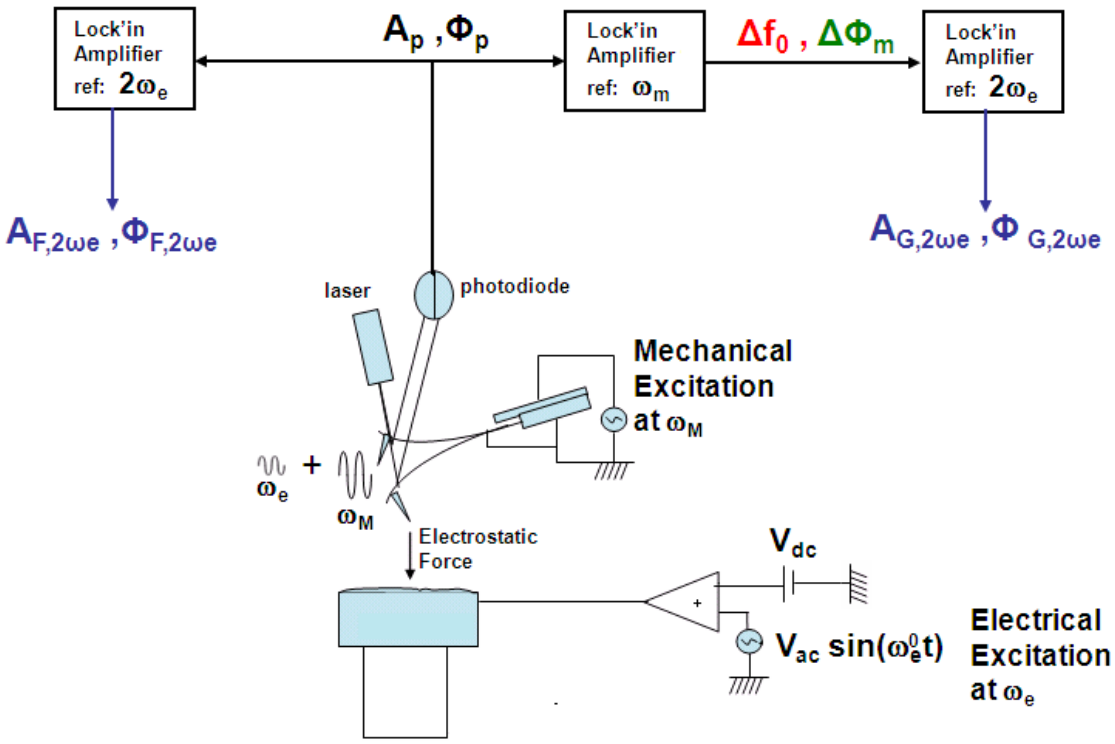

Figure 3.3 : *Schematic Summary of the signals measured in EFM.*

A_p has been used in reference [61] to map quantitatively the dielectric constant of a biological membrane.

The expression of the frequency and phase shift are given by:

$$\Delta f_0 \cong -\frac{f_0}{2k_c}G_{DC} = -\frac{f_0}{4k_c}\frac{\partial^2 C}{\partial z^2}V_{DC}^2 = -\mathbf{a}_{\Delta f_0}(z)V_{DC}^2 \tag{3.28}$$

$$\Delta \phi_m \cong -\frac{Q}{k_c}G_{DC} = -\frac{Q}{2k_c}\frac{\partial^2 C}{\partial z^2}V_{DC}^2 = -\mathbf{a}_{\Delta \phi_m}(z)V_{DC}^2 \tag{3.29}$$

The coefficient $\mathbf{a}_{\Delta f_0}$(z) is of the upmost importance in this work because it will be used in the chapter 3 to determine quantitatively the dielectric constant. The value of ϵ_r will be obtained by fitting $\mathbf{a}_{\Delta f_0}$(z) using the Equivalent Charge Method (see next section).

— **Working with $\mathbf{V}_{AC}$**

Using directly a lock-in amplifier at the electric reference $2\omega_e$ on the signal of the photodiode, we can measure the amplitude $A_{F,2\omega_e}$ and the phase $\Phi_{F,2\omega_e}$ of the $2\omega_e$ component of the force.

$$A_{F,2\omega_e} = \frac{1}{\chi k_c}|F_{2\omega_e}| = \frac{1}{4\chi k_c}\frac{\partial C}{\partial z}V_{AC}^2 \tag{3.30}$$

$A_{F,2\omega_e}$ has been used in reference [62] to measure quantitatively the dielectric constant of thick insulators.

And finally using a lock-in at the electric reference $2\omega_e$ on the frequency shift we can measure amplitude $A_{G,2\omega_e}$ and the phase $\Phi_{G,2\omega}$ of the $2\omega_e$ component of the force gradient.

$$A_{G,2\omega_e} = \frac{1}{\chi k_c}|G_{2\omega_e}| = \frac{1}{4\chi k_c}\frac{\partial^2 C}{\partial z^2}V_{AC}^2 \tag{3.31}$$

The phases $\Phi_{F,2\omega_e}$ and $\Phi_{G,2\omega_e}$ measured while applying a V_{AC} voltage will be used in chapter 4 in order to study the temperature frequency dependance of polymers.

2 The numerical simulation of the Equivalent Charge Method

A number of models describing probe-sample interactions have been proposed in the two last decades. Earlier models treated the probe surface as an equipotential created by a distribution of charges, such as a single point charge [63] or a uniformly charged line [64], and the probe-sample interaction was approximated as the interaction between the assumed charge distribution and its image with respect to the sample surface. Another group of models introduced geometric approximations to the probe shape and solved the probe-sample capacitance problem either by exactly solving the boundary value problem, e.g., the sphere model [65] and the hyperboloid model [66], or by introducing further approximations to the electric field between the probe and the sample [67, 68]. These models provide convenient analytic expressions of the probe-sample interaction; however, more sophisticated models are demanded for studying the lateral variation of the sample surface properties (e.g., topography and trapped charges distribution) or to take into account the presence of a dielectric film of variable thickness.

Let us consider the AFM tip as a cone of height H, half angle θ, with a spherical apex of radius R, attached to the extremity of a cantilever in front of a dielectric medium having a height h and a dielectric constant ϵ_r (Fig. 3.32). The total capacitance $C(z)$ versus the tip-sample distance z is a sum of the apex capacitance $C_{apex}(z)$ (i.e the local capacitance) and the stray capacitance $C_{stray}(z)$, associated with the tip cone and the cantilever contributions. For

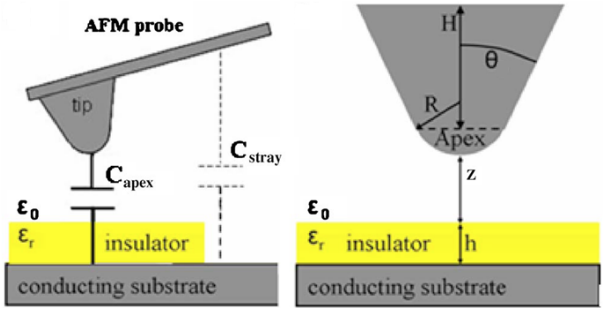

Figure 3.4 : *Schema of the characteristic tip and the dielectric layer [69]*

films thicknesses less than 100 nm we can refer to the model proposed by Fumagalli et al [70]. It can be expressed as:

$$C(z, \epsilon_r, h) = 2\pi\epsilon_0 R\, ln\left(1 + \frac{R(1 - sin(\theta))}{z + h/\epsilon_r}\right) \tag{3.32}$$

By fitting the region where the effect of the local capacitance is negligible, they found a stray capacitance of the linear form $C_{stray} = -bz$. Therefore the stray capacitance does not appear in the expression of $\mathbf{a}_{\Delta f_0}$(z) (which is proportional to the second derivative of the capacitance).

A second family of approaches used numerical methods such as the finite element method [71], the self-consistent integral equation method [72], and the boundary element method [73]. The main advantage of these models is their ability to take into account the exact geometry of the EFM probe, which permits comparison of different probe tip shapes.

We will use here the numerical simulation of the Equivalent Charge Method (ECM)to model the tip sample interaction. The advantage of numerical simulation compared to analytical

expressions is that it permits to work without any restriction on the height of the polymer film. The methodology of ECM is always the same: find the position of different charges that will create the potential researched and then calculate their electrostatic charges using limit conditions. We will first treat the case of a tip in front of a metallic plate, and then we will deduce the force for a system composed by a tip in front of a dielectric layer over a metallic plate.

2.1 Tip over a metallic plate

Before modelling the tip, we will study the simple example of a charge +q, located at (0, a) above a metallic plate grounded at a 0V potential, lying along the x-axis. Deriving the charge distribution on the plate, or the force felt by the point charge by solving general electrostatic equations is not trivial. It is simplified by replacing the metal with a charge, located at (0, -a) and with charge -q. This arrangement will produce the same electric field at any point for which z > 0, and satisfies the boundary condition, that the potential along the plate must be zero. This new setup is depicted in Fig. 3.5

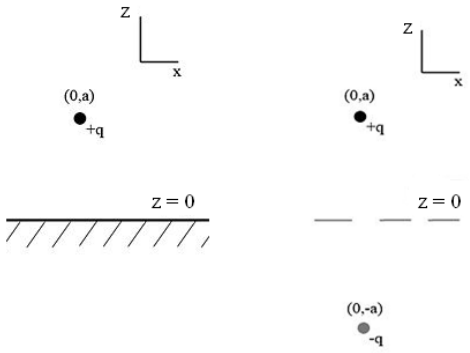

Figure 3.5 : *One charge over a metallic plate (left) and its equivalent in term of ECM (right)*

The case of a system composed by a tip in front of a conductive plane has been treated in [74]. The surface of the tip is at a potential V. The idea of ECM is to find a discrete charge distribution (N_c charge points q_i at a distance r_i on the axis x=0) that will create the desired potential at the surface of the tip. The conductive plane at a zero potential is created by the introduction of an electrostatic image tip with $-q_i$ charges at a distance $-r_i$ on the z axis (Fig. 3.6).

Position and number of the charges and test points have to be chosen with care because the stability of the system of equations that we will obtain depends on these parameters. For the cone, charges are displayed on a geometrical serie, while test points are projected on the tip surface. One test point is intercalated between two projections. For the spherical part, the position of the charges and test points is chosen manually to reproduce the strong curvature of the equipotential where is concentred the most of the interaction.
Test points have to fulfilled two conditions:
- The distance between two successive test points should not be too big to ensure that the potential created follows the surface of the tip.
- If this distance is too small, the matrix describing the system could become singular.

The value of the charges q_i is fixed in such way that the potential V_n calculated in the test point n at the tip surface equals V.

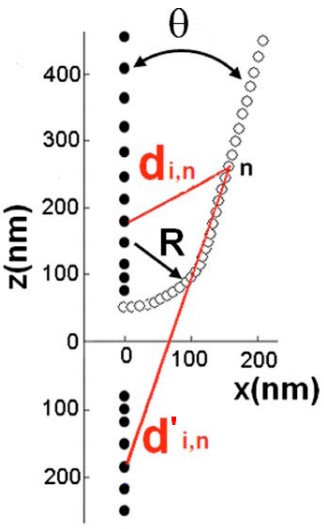

Figure 3.6 : *Distribution of the charges (•z>0), image charges (•z<0)that will create the potential of the tip measured in the test points ∘*

If we introduce

$$C_{i,n} = \frac{1}{d_{i,n}} - \frac{1}{d'_{i,n}} \tag{3.33}$$

where $d_{i,n}$ and $d'_{i,n}$ are the distance between the point n and the effective and image charge i, respectively, we can express the potential Vn as:

$$V_n = \sum_i \frac{C_{i,n}\, q_i}{4\pi\epsilon_0} \tag{3.34}$$

The best value of q_i is obtained using the least mean square method:

$$\frac{\partial}{\partial q_i} \sum_n (V_n - V)^2 = 2 \sum_n \left((V_n - V) \frac{\partial V_n}{\partial q_i} \right) = 0 \tag{3.35}$$

Expliciting the value of V_n and its derivative, we get:

$$\sum_n \left(\sum_i \frac{C_{i,n} q_i}{4\pi\epsilon_0} - V \right) \frac{C_{j,n}}{4\pi\epsilon_0} = 0 \tag{3.36}$$

which can be written as a system of linear equations where nmax is the number of test points and q_i are the variables.

$$\begin{pmatrix} \vdots & & \\ \cdots & \sum_{n=1}^{nmax} C_{i,n} C_{j,n} & \cdots \\ \vdots & & \end{pmatrix} \begin{pmatrix} q_1 \\ \vdots \\ q_i \\ \vdots \\ q_{Nc} \end{pmatrix} = \begin{pmatrix} \vdots \\ 4\pi\epsilon_0 V \sum_{n=1}^{nmax} C_{j,n} \\ \vdots \end{pmatrix} \tag{3.37}$$

We obtain the best value of q_i by solving the linear system of equation 3.37. Knowing the position and the value of the charges q_i we can calculate the force which is the resultant of the interaction of each charge q_i with all the image charges q'_j:

$$F = \frac{1}{4\pi\epsilon_0} \sum_{i=1}^{Nc} \sum_{j=1}^{Nc} \frac{q_i\, q'_j}{d_{i,j}^2} \tag{3.38}$$

2.2 Tip over a dielectric layer plus a metallic plate

a One charge over a semi-infinite dielectric

Before modelling the complete system, we will study the potential created by a charge q_0, located at (0, a) above a semi-infinite dielectric, lying along the x-axis (Fig.3.7). We will demonstrate that the potential created by this charge in the air (z>0) $V_0(P)$ and in the dielectric (z<0) $V_1(Q)$ are given by:

$$V_0(P) = \frac{1}{4\pi\epsilon_0}\left(\frac{q_0}{r_0} + \frac{q_1}{r_1}\right) \tag{3.39}$$

$$V_1(Q) = \frac{1}{4\pi\epsilon_1}\frac{q_2}{r_2} \tag{3.40}$$

Notations are defined on figure 3.7.

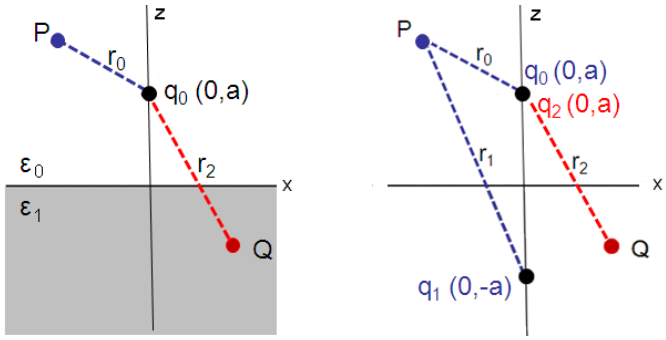

Figure 3.7 : *One charge over a semi-infinite dielectric (left) and its equivalent in term of ECM (right)*

The charge q_1 is the symmetric of q_0 in regard to the x-axis that satisfies limit conditions which are written on the x-axis:

$$V_0 = V_1 \tag{3.41}$$

$$\epsilon_0 \frac{\partial V_0}{\partial z} = \epsilon_1 \frac{\partial V_1}{\partial z} \tag{3.42}$$

Inserting Eq. 3.39 and 3.40 in Eq. 3.41, 3.42 we obtain the value of the charges q_1 and q_2:

$$q_1 = -\left(\frac{\epsilon_1 - \epsilon_0}{\epsilon_0 + \epsilon_1}\right) q_0 \tag{3.43}$$

$$q_2 = \frac{2\epsilon_1}{\epsilon_0 + \epsilon_1} q_0 \tag{3.44}$$

Knowing the position and the value of the charges we can calculate the potential in all the space.

b Charge over a dielectric layer plus a metallic plate

When the system is composed by a tip in front of a dielectric layer plus a conductive plane, simulations are more complicated. This problem has been treated by Saenz et al [75] introducing the Green Function formalism. In our study, we have chosen to follow the early method of Durand [76]. We consider a charge q_0 in the air (dielectric constant taken at ϵ_0) at a distance **a** of a dielectric layer of thickness **h** and dielectric constant ϵ_r over a metallic plate. We note $b = a + h$ the distance between the charge and the metallic plate (Fig.3.8).

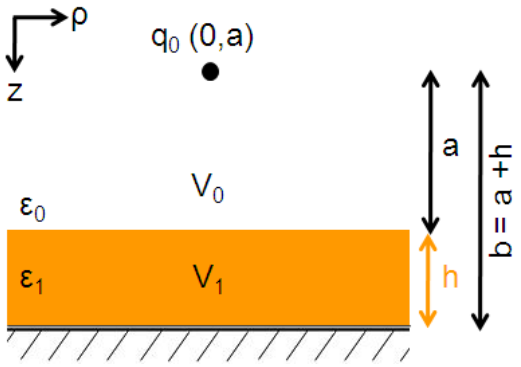

Figure 3.8 : *Schema of one charge over a dielectric layer lying on a metallic plate. Axis are chosen to facilitate calculations.*

In order to calculate the potential at the different interfaces and take into account the symmetry of the problem, we express the potential created by the charge using cylindrical coordinate (ρ, z) and introducing the Bessel function J_0:

$$V = \frac{q}{4\pi\epsilon_0 r} = \frac{q}{4\pi\epsilon_0}\int_0^\infty J_0(m\rho)e^{-m|z|}dm \tag{3.45}$$

This equation satisfies to the Laplace equation for all functions e^{mz}. We would like to have, for each dielectric, solutions of the form:

$$V_0 = \frac{q_0}{4\pi\epsilon_0}\int_0^\infty \left(e^{-m|z|} + A(m)e^{mz}\right) J_0(m\rho)dm \tag{3.46}$$

$$V_1 = \frac{q_0}{4\pi\epsilon_1}\int_0^\infty \left(B(m)e^{-mz} + C(m)e^{mz}\right) J_0(m\rho)dm \tag{3.47}$$

where A(m), B(m) and C(m) are functions to determined. Limit conditions are written as:

$$(V_0 - V_1)_{z=a} = 0 \tag{3.48}$$

$$\left(\epsilon_0\frac{\partial V_0}{\partial z} - \epsilon_1\frac{\partial V_1}{\partial z}\right)_{z=a} = 0 \tag{3.49}$$

$$(V_1)_{z=b} = 0 \tag{3.50}$$

In order to facilitate calculation, we express limit conditions on the z axis ($\rho = 0$):

$$\begin{pmatrix} -\epsilon_1 e^{ma} & \epsilon_0 e^{-ma} & \epsilon_0 e^{ma} \\ e^{ma} & e^{-ma} & -e^{ma} \\ 0 & e^{-mb} & e^{mb} \end{pmatrix} \begin{pmatrix} A \\ B \\ C \end{pmatrix} = \begin{pmatrix} \epsilon_1 e^{-ma} \\ e^{ma} \\ 0 \end{pmatrix} \tag{3.51}$$

Introducing $k_1 = -\frac{\epsilon_1 - \epsilon_0}{\epsilon_1 + \epsilon_0}$ and $h = b - a$ we get:

$$A = \frac{k_1 e^{2ma} - e^{-2mb}}{1 - k_1 e^{2ma}} \tag{3.52}$$

$$B = \frac{1 - k_1}{(1 - k_1)e^{-2mh}} \tag{3.53}$$

$$C = -\frac{(1 - k_1)e^{-2mb}}{1 - k_1 e^{-2mh}} \tag{3.54}$$

We deduce the expression of the potential V_0:

$$V_0 = \frac{q_0}{4\pi\epsilon_0} \int_0^\infty \left(e^{-m|z|} + \frac{k_1 e^{2ma} - e^{-2mb}}{1 - k_1 e^{2ma}} e^{mz} \right) dm \tag{3.55}$$

in which we can calculate the integral [76]:

$$V_0 = \frac{q_0}{4\pi\epsilon_0} \left(\frac{1}{|z|} - \frac{k_1}{z - 2a} + (1 - k_1^2) \sum_0^\infty \frac{k_1^n}{z - 2b - 2nh} \right) \tag{3.56}$$

The potential created in air take into account the source, its image by the dielectric surface and an infinite serie of image charges issue from the reflection on the dielectric and the metallic surface (Fig.3.9).

Using the same method, we get the potential V_1 which is equivalent to the one created by the sum of two infinite series arising from the reflection of the charge q_0 at each interface ((Fig.3.9)):

$$V_1 = \frac{q_0}{4\pi\epsilon_1} \int_0^\infty \left(\frac{1 - k_1}{(1 - k_1)e^{-2mh}} e^{-mz} - \frac{(1 - k_1)e^{-2mb}}{1 - k_1 e^{-2mh}} e^{mz} \right) dm \tag{3.57}$$

$$V_1 = \frac{q_0}{4\pi\epsilon_0} (1 - k_1) \left(\sum_0^\infty \frac{k_1^n}{z + 2nh} + \sum_0^\infty \frac{k_1^n}{z - 2nb - 2ne} \right) \tag{3.58}$$

We are now able to express the potential in any point (ρ,z) created by each charge q_i (0,z_i). To keep coherent notation with previous section, these expression are given for z>0 from the dielectric to the tip. Introducing notations for the different contributions of the image and series of images:

$$D\pm = \frac{1}{\sqrt{\rho^2 + (z \pm z_i)^2}} \tag{3.59}$$

$$A = \sum_{n=0}^\infty \frac{k^n}{\sqrt{\rho^2 + (z + 2(n+1)h + z_i)^2}} \tag{3.60}$$

$$B = \sum_{n=0}^\infty \frac{k^n}{\sqrt{\rho^2 + (z - 2nh - z_i)^2}} \tag{3.61}$$

we obtain the potentials created by the tip:

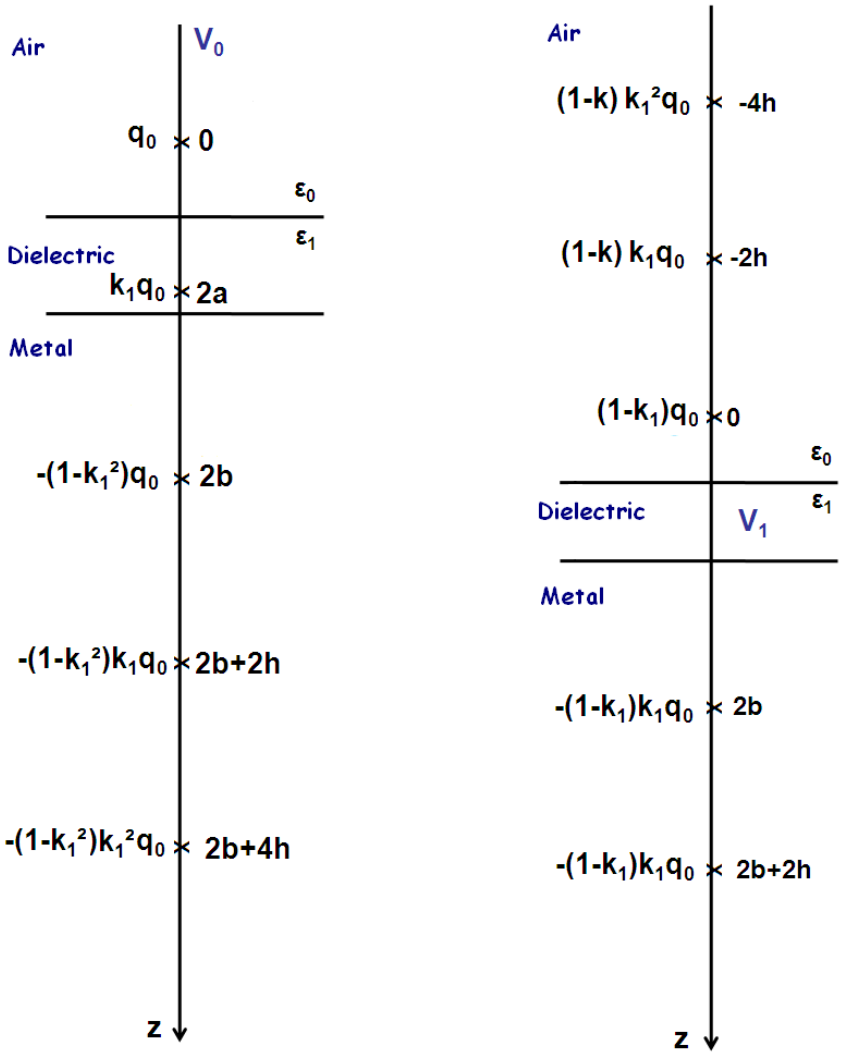

Figure 3.9 : *Series of image creating V_0 in the air (left) and V_1 in the dielectric (right)*

$$V_0 = \sum_i V_0^i = \sum_i \frac{q_i}{4\pi\epsilon_0}(D_+ + kD_-(1-k^2)A \tag{3.62}$$

$$V_1 = \sum_i V_1^i = \sum_i \frac{q_i}{4\pi\epsilon_0}(1-k)(B-A) \tag{3.63}$$

c Tip over a dielectric layer plus a metallic plate

An example of the potential created in the air and in the dielectric by a nanoscopic tip is shown in Fig.3.10.

We are now able to calculate the force (and then the force gradient, capacitance and coefficient $\mathbf{a}_{\Delta f_0}(z)$) of our system:

$$F = \frac{1}{4\pi\epsilon_0}\sum_{i,j}\left(\frac{k_1 q_i q_j}{(z_i+z_j)^2} - q_i q_j(1-k_1^2)\sum_{n=0}^{\infty}\frac{k_1^n}{(z_i+z_j+2(n+1)h)^2}\right) \tag{3.64}$$

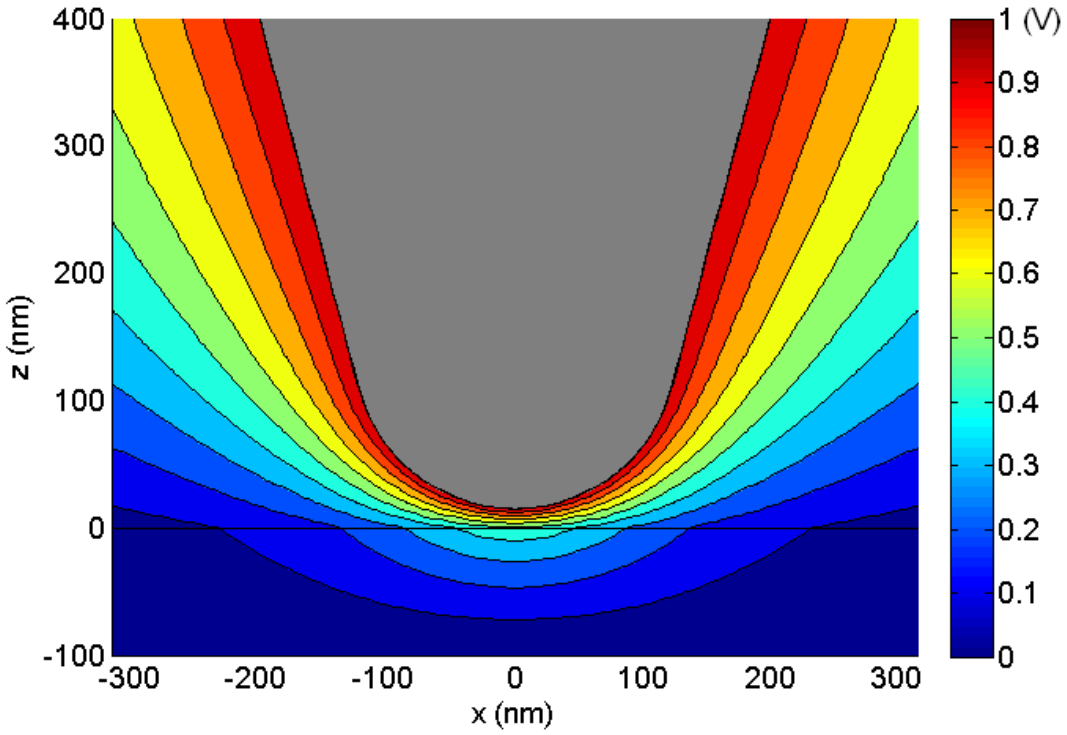

Figure 3.10 : *Potential, created in the air (z>0nm) and in the dielectric (z<0) by a tip (R=130nm, θ=15 $^\circ$) in front of a dielectric layer of height h=100nm with a dielectric constant $\epsilon_r = 4$. The potential is set to 1V at the surface of the tip. The maximum error in one test point is of the order 1/1000.*

2.3 Behavior of the parabolic coefficient

We remind that:

$$\Delta f_0 = -\mathbf{a}_{\Delta f_0}(z) V_{DC}^2 \tag{3.65}$$

$$\mathbf{a}_{\Delta f_0} = \frac{f_0}{4k_c}\frac{\partial^2 C}{\partial z^2} \tag{3.66}$$

$\mathbf{a}_{\Delta f_0}$ is directly measured by EFM at different lift z and then experimental points are fitted to obtain the value of ϵ_r. The best-fitting curves were obtained by the least-squares method and the final uncertainties are calculated including uncertainties of all others parameters involved in the calculations. It is interesting to study the behavior of $\mathbf{a}_{\Delta f_0}$(z) to know what are the best parameters for our experiment. $\mathbf{a}_{\Delta f_0}$ is function of five parameters: z, R, θ, h and ϵ_r.

a Tip parameters: R, θ

As explained above, the first step in the quantitative determination of the dielectric constant is the measurement of the "electrostatic" tip radius over a metallic plate. Therefore, in order to understand the importance of the tip parameters R and θ we simulate the interaction between a tip and a metallic plate. As already mentioned the effect of the cone (θ) is negligible for small distances. For our simulation we took the typical value: θ=15°C. Fig.3.11 represents the shape of $\mathbf{a}_{\Delta f_0}(z)$ for different value of the radius of the tip. We see that for a distance of the lift fixed the value of $\mathbf{a}_{\Delta f_0}$ (the intensity of the signal measured) increases with the radius. The bigger is the radius the stronger is the interaction. However, the spatial resolution decreases (i.e. its

numerical value increases) when the tip radius increases (see reference [77, 78] and chapter 3) and classical EFM tips having a radius of about 20 nm are convenient to perform this study.

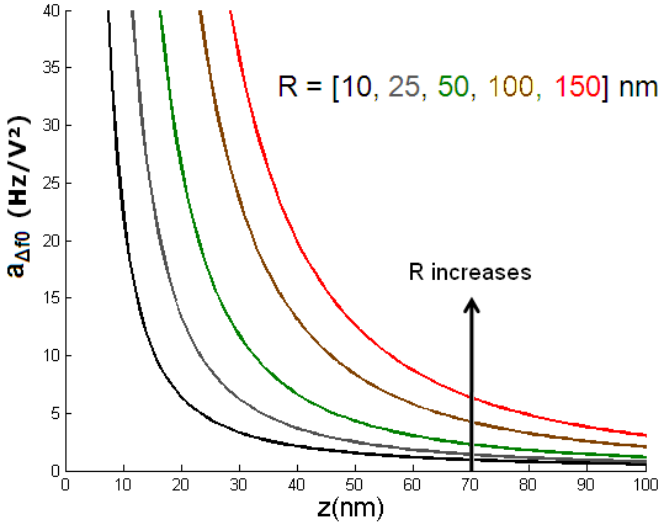

Figure 3.11 : *Behavior of $\mathbf{a}_{\Delta f_0}(z)$ as a function of the radius of the tip. (Simulated over a metallic plate)*

b Sample parameters for the dielectric: h, ϵ_r

The behavior of $\mathbf{a}_{\Delta f_0}$(z) as a function of the height for a given $\epsilon_r = 4$, is represented in Fig. 3.12 a. The strength of the interaction (and so the value of $\mathbf{a}_{\Delta f_0}$(z) at a fixed lift) increases when the height of polymer decreases. The stronger interaction is obtained for the limit case of the nude metallic surface (h=0). Fig. 3.12 b shows the behavior $\mathbf{a}_{\Delta f_0}$(z) as a function of the

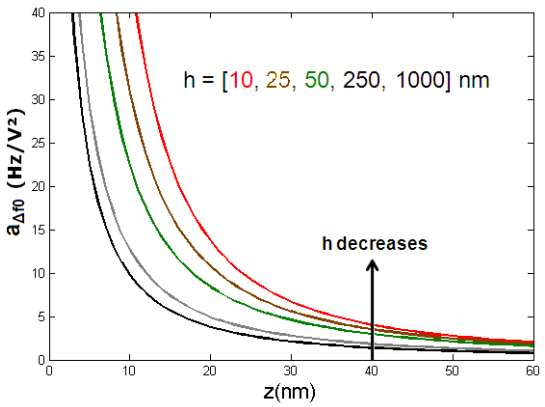

(a) *Behavior of $\mathbf{a}_{\Delta f_0}(z)$ as a function of the thickness of the sample. ($\epsilon_r = 4$)*

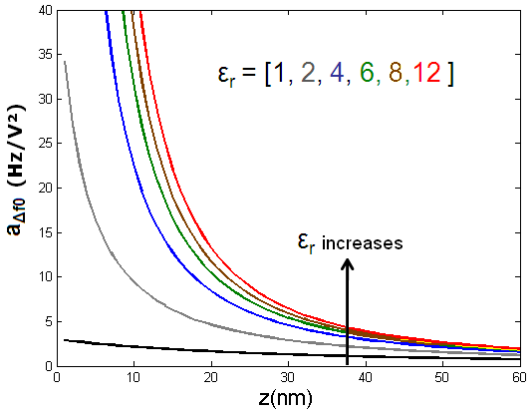

(b) *Behavior of $\mathbf{a}_{\Delta f_0}(z)$ as a function of ϵ_r. (h= 100 nm)*

Figure 3.12

dielectric constant for a given thickness of 100 nm. The strength of the interaction increases with the dielectric constant.

c Sensitivity

We are not only interested by the intensity of the signal but also by the sensitivity S of the method, i.e. its ability to detect a relative change in the coefficient $\mathbf{a}_{\Delta f_0}$ for a given change in ϵ_r:

$$S = \frac{1}{\mathbf{a}_{\Delta f_0}(z)} \frac{\partial \mathbf{a}_{\Delta f_0}(z)}{\partial \epsilon_r} \tag{3.67}$$

As shown in Fig. 3.13, the sensitivity clearly decreases when the dielectric permittivity increases. This point can be a limiting factor for the study of high dielectric permittivity materials ($\epsilon_r > 10$) but not for the study of polymers, for which $2 < \epsilon_r < 10$. One way to increase the sensitivity is to increase the thickness of the sample (Fig. 3.13). As mentioned, the signal will be weaker but this problem could be overcome by increasing the voltage.

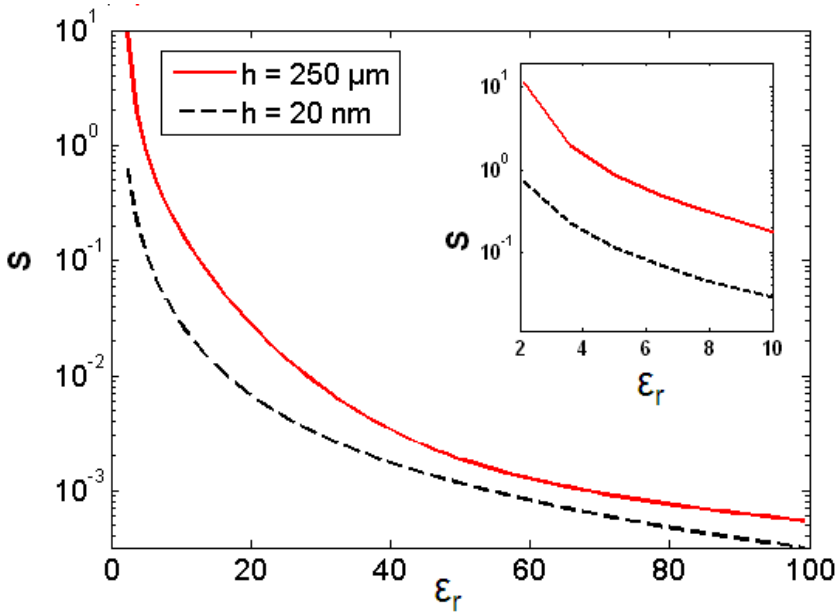

Figure 3.13 : *Sensitivity of the measurement of $\mathbf{a}_{\Delta f_0}(z)$ as a function of ϵ_r (z=20 nm). Inset: zoom on the range of epsilon corresponding to polymers (ϵ_r<10*

2.4 Introduction to the penetration depth of the electric field

The penetration depth is a measure of how deep the electric field penetrates into a material. It can be defined as the depth at which the field inside the material falls to 1/e of the original value at the surface. In the context of this work, we can reformulate the problem of the penetration depth in one question: Are we able to measure the dielectric response of a buried object? The answer depends of the properties of the object and of the geometry of the system. For instance, if you would like to measure the dielectric response of an underneath layer of polymer, the depth penetration would depend on the dielectric constant and thickness of the upper layer. Therefore a full modelization of the system is needed for each particular case.

Studies involving different experimental techniques like BDS [79, 80], fluoresence [81, 82] or Local Dielectric Spectroscopy (see chapter 4 and reference [10,11]) have shown different dynamics between interfaces and bulk. Controlling the penetration depth would allows measuring, on

the same sample and with the same experimental technique, both surface and bulk-like behavior.

— **Few words about Broadband Dielectric Spectroscopy (BDS)**
Experimental BDS samples are modelized as a plate-plate capacitor (see chapter 1). Therefore, the potential lines are perpendicular to the electrodes and the electric field is constant along these lines: BDS measure the dielectric response over the all thickness and we cannot estimate a penetration depth. This problem, in addition to the lack of spatial resolution, makes the study of nano-structured systems always model dependant.

We will now detail a simulation of the penetration of the electric field created by a tip having a radius of 20 nm in a semi-infinite dielectric medium modelized by h=1 μm and $\epsilon_r = 4$.

— **Electrostatic Force Microscopy**
Using the numerical simulation of the ECM, we are able to calculate the potential created in all the space by an AFM tip at a tip-sample distance of 20 nm in front of a dielectric medium (see Fig. 3.10). We numerically select the value of the potential inside the dielectric along the z-axis. As the electric field E is the gradient of the potential, we are able to calculate E(z) along this line. The criterium to define the depth penetration is defined as E(z) = E(0)/e. Fig. 3.14 a represents E(z) for different tip-sample distances (from 20 to 200 nm) measured on the x=0 axis of a 1 μm sample. Solid line represents the thickness where E(z)>E(0)/e whereas dotted line are below the depth penetration. For a classical tip sample distance of 20 nm the penetration depth is of about 40 nm: only the first layers of the sample are probed. It is interesting to note (Fig. 3.14 b) that the penetration depth, p, increases linearly with the tip-sample distance:

$$p \simeq R + z \tag{3.68}$$

Working at a higher value of the tip-sample distance would allow measuring deeper properties in the sample. For a tip-sample of 20 nm, the electrostatic interaction is concentrated over the first 40 nm layer from the interface with the free interface (air or vacuum).

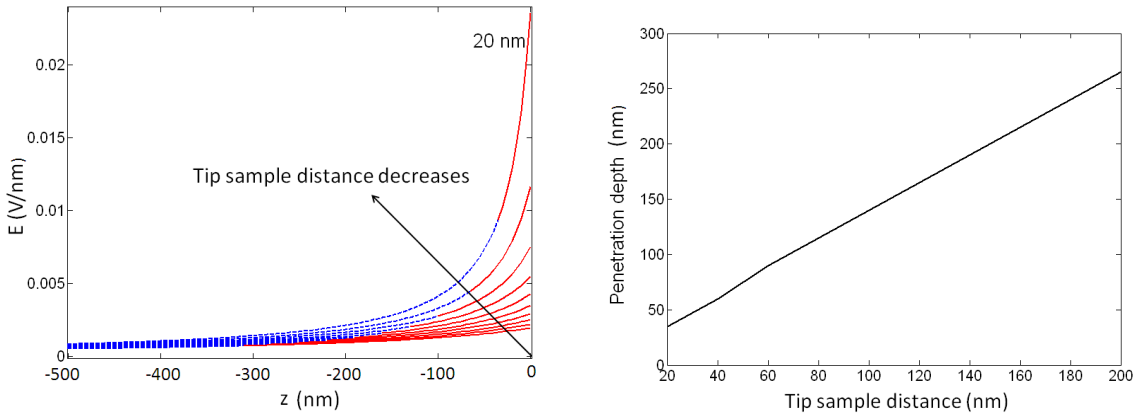

(a) *Electric field inside a 1 μm sample for different tip sample-distances (z=20 to 200 nm, Δz=20 nm)*

(b) *Penetration depth as a function of the tip-sample distance for a thick sample (1 μm)*

Figure 3.14

3 Measuring local dielectric properties: State of the art

The classical way to measure dielectric properties is Broadband Dielectric Spectroscopy (BDS). This technique, based on the measurement of the capacitance of a parallel plate capacitor, presents a lot of advantages: well known geometry, very good temperature stabilization and sensitivity. However, there is no spatial resolution and the measurement of local properties is therefore not possible. In this section, we detail the contributions found in literature to measure locally dielectric properties.

3.1 Capacitance measurements

The first idea to measure local properties was to keep the capacitance measurement used in BDS and reduce the size of the electrode. The expression of the capacitance of a parallel plate partially filled with a dielectric medium of thickness h (see Fig. 3.15) is proportional to the area A of the electrodes:

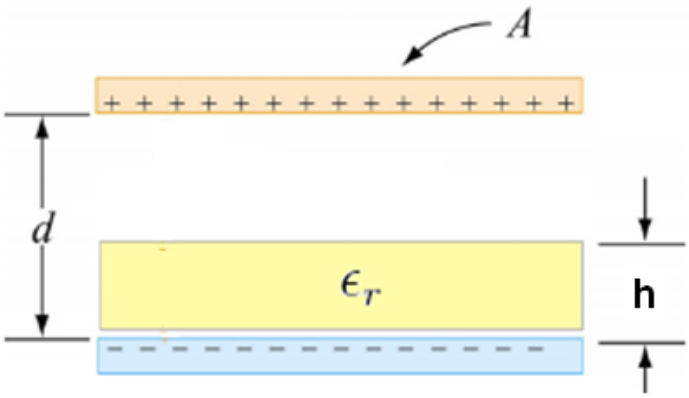

Figure 3.15 : *Schematic representation of a capacitor having a distance d between electrodes of area A, filled with a dielectric of thickness h and dielectric constant ϵ_r.*

$$C = \epsilon_0 \frac{A}{d - h + h/\epsilon_r} \tag{3.69}$$

The main issue to realize local measurements with an electrode having a small area is the detection of low value of the capacitance. Two methods, nanoscale impedance microscopy and nanoscale capacitance microscopy have been developed in this way. The main drawbacks of these methods are the homemade electronics needed to measure extremely low capacitance and the great care to avoid and characterize stray capacitances.

— **Nanoscale impedance microscopy**

The principle of nanoscale impedance microscopy is detailed in reference [83] and [84]. They measured capacitance values in the picofarad ($10^{-12}F$) to femtofarad ($10^{-15}F$) range on a set of square parallel plate capacitors using a homemade nanoscale impedance microscopy (NIM) device. Measurements were realized on totally filled (h=d) metal-insulator-metal sandwiches. The insulator was a glass ceramic (Macor®) having a dielectric constant around 6, a thickness of 1mm and an area of 8*8 μm^2. Measurements of the capacitance have been realized other different kind of sample (square, rectangular, surrounded by guard ring) and experimental results

have been compared to numerical calculations and simple analytical model. Some deviation from Eq. 3.69 were reported: A first term due to edge effects, which cease being negligible when the upper electrode size becomes lower than the insulator thickness (term K_1), and a second due to the existence of a stray capacitance (term K_2) leading to an expression of the modeled capacitance C_m:

$$C_m = \epsilon_0 \epsilon_r ((A/h + PK_1) + K_2) \tag{3.70}$$

where P is the perimeter of the sample. Value of K_1 and K_2 were determined by fitting experimental capacitance versus upper surface curves for different geometry. Then, they have realized a topographical and capacitance image of tiny 8*8 μm^2 capacitor (Fig. 3.16).

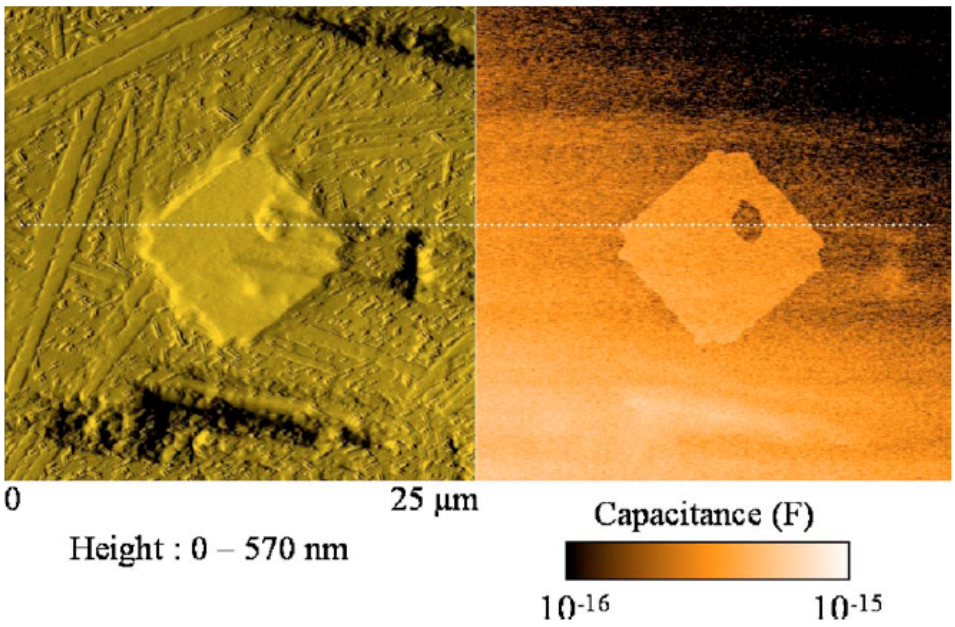

Figure 3.16 : *Topographical (left) and capacitance (right) images, performed in 85 min, with 512*512 image resolution [83]*

— **Nanoscale capacitance microscopy**

Nanoscale capacitance microscopy, also refereed as nanoscale dielectric spectroscopy, has been developed by Gomila *et al* [69,70,85,86]. Using a custom-made current-to-voltage amplifier connected to the AFM tip they reached attofard ($10^{-18}F$) resolution. As previously mentioned, they developed an expression of the capacitance valid for films thicknesses h less than 100 nm [70]:

$$C(z, \epsilon_r, h) = 2\pi\epsilon_0 R\, ln\left(1 + \frac{R(1 - sin(\theta))}{z + h/\epsilon_r}\right) \tag{3.71}$$

The stray capacitance was determined by fitting the curves where the local capacitance is negligible (high value of the tip sample distance) and then subtracted to measurements in order to obtain the tip-sample capacitance ΔC. Using this technique, they first realized capacitance map of a silicon oxide [69]. Then, they used the analytical expression (Eq. 3.71) to fit the capacitance versus tip-sample distance curves in order to get a quantitative value of the dielectric constant of a 1*1 μm^2 SiO_2 squares, ϵ_r=4 (Fig. 3.17). Measurements over gold substrate (h=0)

allowed to fit the radius of the tip.

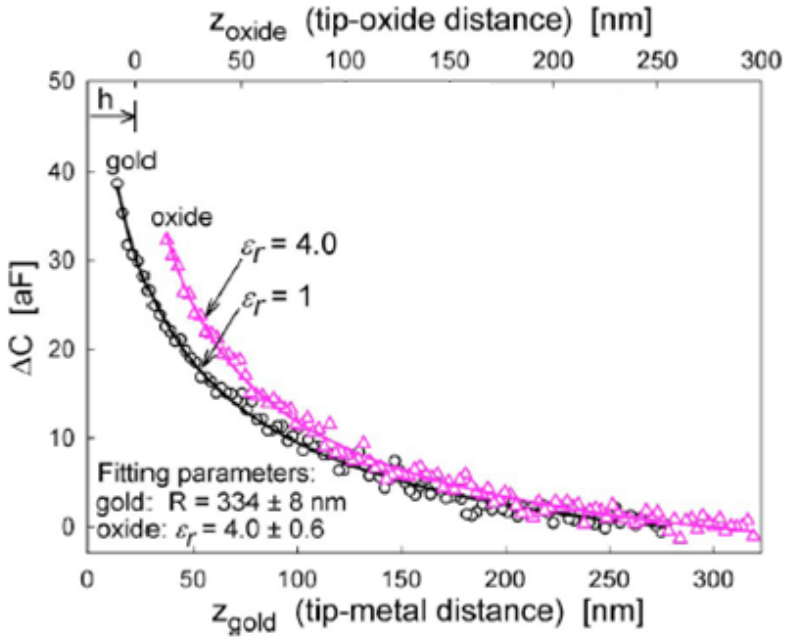

Figure 3.17 : *Measured ΔC vs tip-sample distance taken on a 23-nm-thick SiO2 layer (triangles) and on the gold surface (circles) close to the oxide [85].*

An important step in the development of the nanoscale capacitance microscopy was the transition toward imagery. Using a two pass method, the authors first record the topography and the then measured the capacitance during a second pass at a constant tip-electrode distance. Dielectric constant images are then quantitatively reconstructed by introducing the thickness and local capacitance in Eq. 3.71. [87]. First quantitative maps of the dielectric constant have been obtained on a single-layer biomembrane with a spatial resolution of about 70 nm.

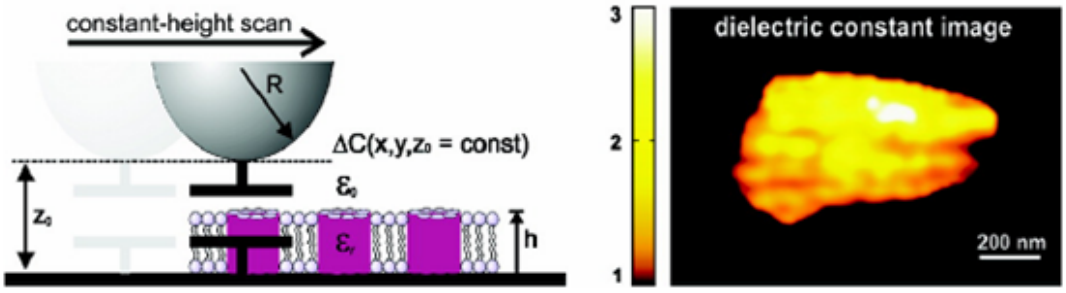

Figure 3.18 : *Left: Schema of the experiment. Right: Quantitative dielectric map of a biomembrane [87]*

3.2 EFM based methods

— Scanning Polarization Force Microscopy

Scanning Polarization Force Microscopy (SPFM) [63, 88] has been the first method (developed in 1995) to qualitatively map dielectric polarization. Using polarization forces they have been able to image liquid films, droplets, and other weakly adsorbed material. The images are obtained by adjusting the separation between the sample and the cantilever such that its bending stays constant while the tip is scanned over the surface. The bias applied is either DC or AC and has a value of few volts. Working with very sharp tip and small tip-sample distances, they reached spatial resolution of about 50 nm horizontally and one angstrom vertically. Fig. 3.19 exemplifies an utilization of SPFM to map the water film due to humidity (average thickness of about 2 Å) covering a mica surface. The two phases are due to a difference in dielectric constants related with a difference in humidity in these domains.

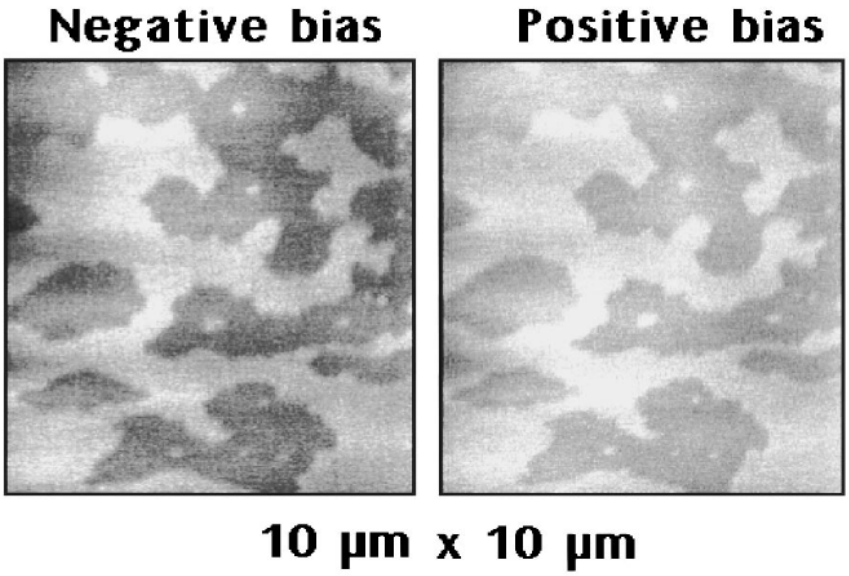

Figure 3.19 : *Images of a water film on mica formed at 40% humidity for both positive and negative bias. Two phases are observed: phase I forms first (light areas) and later, above 25% humidity, phase II (dark areas) forms. The fraction of surface covered by each phase depends on humidity. Phase II has a lower dielectric constant than phase I, which makes its apparent height lower than that of phase I. [88]*

— Quantification of the dielectric constant of heterogeneous blend measuring phase shifts

In 2004, Krayev *et al* realized a study of polymers heterogeneous blend in the form of layer of several microns thickness [89, 90]. The authors showed that an electric contrast could be obtained on EFM phase images and that such a contrast is related to the variations of the relative dielectric permittivity ϵ_r. They quantified the value of ϵ_r in the frame of a simple spherical capacitor model. Unfortunately, this model is appropriate only under certain conditions because it makes the approximation that the thickness of the sample is very large compared to the tip radius and the tip-sample distance. Dielectric constants of two reference polymers ϵ_{r1} and ϵ_{r2} are required to measure a third unknown one (ϵ_{r3}). This value is obtained from the ration of the difference of phase measured between two polymers: $\frac{\Delta\Phi 1-\Delta\Phi 2}{\Delta\Phi 2-\Delta\Phi 3}$ where the only unknown is one of the dielectric constant. Fig. 3.20 represents a 3 dimensional plot (x and y are spatial coordinates and z is the phase shift) of a atactic poly(propylene) (APP), poly(isopropyl acrylate) (PIPA) and poly(octylmethacrylate) (POMA) blend. The matrix is constitued by POMA

having a dielectric constant $\epsilon_{r1} = 3$, peaks are characteristic of PIPA regions (ϵ_{r2} is supposed to be unknown) and holes are APP domains (ϵ_{r3}=2.2). Using these set of data authors find a value of the dielectric constant of PIPA, ϵ_{r2}=4.25, in good agreement with literature.

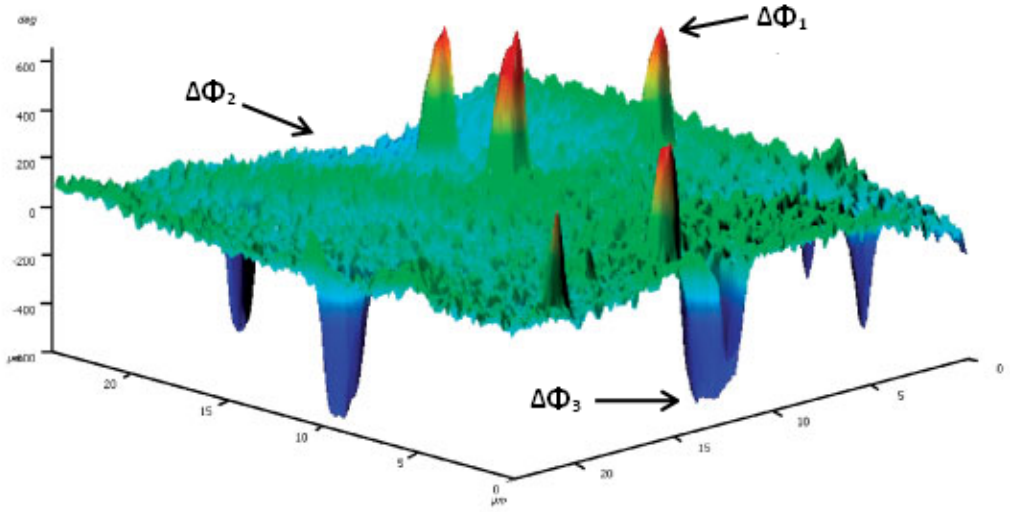

Figure 3.20 : *3 dimensional plot of the phase shift measured over a POMA, PIPA, APP polymer blend. x and y are spatial coordinates (in µm), z is the phase shift (in degree). The matrix is composed by POMA ($\epsilon_{r1} = 3$), peaks by PIPA (ϵ_{r2}=4.25) and holes by APP (ϵ_{r3}=2.2). The dielectric constant of one of the component can be calculated from phase shifts measured on this plot and the value of the dielectric constant of the 2 others components [90].*

— Quantitative dielectric map in the force mode applying a DC bias

In reference [61], Gramse *et al* presented a simple method to measure the static dielec-

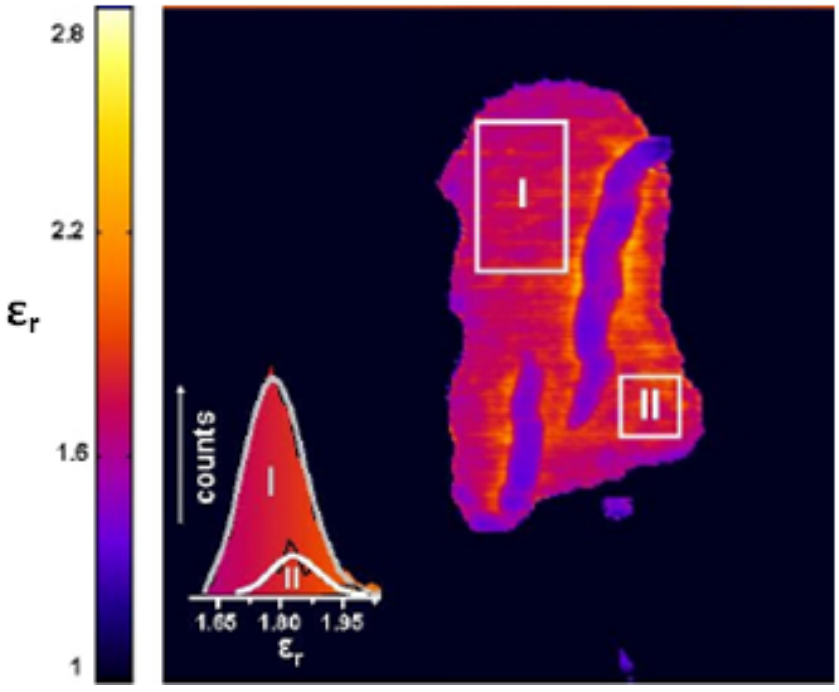

Figure 3.21 : *Dielectric constant map of a purple membrane in the force mode*

tric constant of thin films with a spatial resolution of about 70 nm. The dielectric constant

is extracted from DC electrostatic force (term A_p in Eq. 3.27) measurements with the use of the analytical expression of the capacitance previously reported by the same group (Eq. 3.71). The method is validated on thin silicon dioxide films (8 nm thick, dielectric constant $\epsilon_r \sim 4$) and purple membrane monolayers (6 nm thick, dielectric constant $\epsilon_r \sim 2$), providing results in good agreement with those recently obtained by nanoscale capacitance microscopy using a current-sensing approach. The main advantage of the force detection approach resides in its simplicity and direct application on any commercial atomic force microscope with no need of additional sophisticated electronics. Fig. 3.21 represents the dielectric map of the biological membrane.

— Quantitative measurements in one point, in the force mode applying an AC bias

In reference [62], authors measured the modulus of the the $2\omega_e$ component of the force (term $A_{F,2\omega_e}$ in Eq. 3.30) to quantify the dielectric constant of thick insulators. As the thickness of the samples was superior to 100 nm, they were not able to use the analytical expression of the capacitance (Eq. 3.71) as in their previous publication and chose to work with finite element calculation. The advantage of this technique compared to DC methods is that the lock-in suppresses all the noises that are not at the electrical frequency. As it will be demonstrated using numerical simulation in the Equivalent Charge Method section, working with thick films permit to reach better sensitivity. Fig. 3.22 summarizes the quantification of the dielectric constant of different polymers by fitting the $2\omega_e$ component of the force (i.e. the derivative of the capacitance $\Delta C'$ as a function of the tip-sample distance.

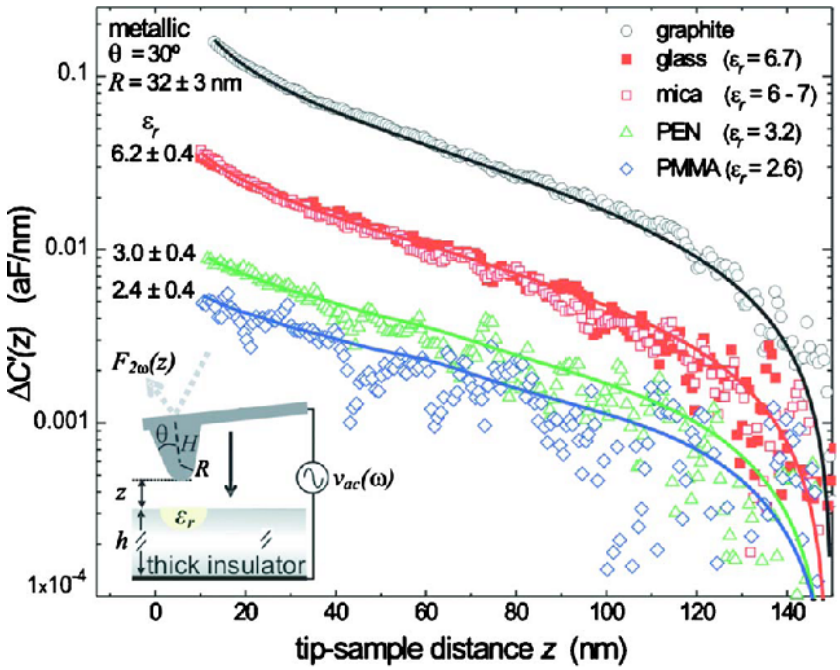

Figure 3.22 : *Quantification of the dielectric constant in the force mode applying an AC bias. Lines are fit of the experimental data by finite element models. Numbers at end of lines are values for simulation with confidence bounds on fit [62]*

— **Local Dielectric Spectroscopy: Measuring frequency dependant properties**

Local Dielectric Spectroscopy [10, 11] has been developed by Crider *et al* under Ultra High Vacuum in the gradient mode. This method will be detailed in the last chapter of this thesis (Measurement of the temperature frequency dependence of the dielectric permittivity at the nanoscale). LDS has been used in reference [91] to study how relaxation dynamics of a poly(vinyl-acetate) ultra-thin film is influenced by inorganic nano-inclusions of a layered silicate (montmorillonite). Dielectric loss spectra are measured by electrostatic force microscopy in the frequency-modulation mode in ambient air. Spectral changes in both shape and relaxation time are evidenced across the boundary between pure polymer and montmorillonite sheets. Dielectric loss imaging is also performed, evidencing spatial variations of dielectric properties near to nanostructures with nanometer scale resolution.

3.3 Timeline summary

1995: Scanning Polarization Force Microscopy: First qualitative images of dielectric polarization. Salmeron *et al* [63, 88]

2004: Quantification of the dielectric constant of polymers by measuring phase shifts. The dielectric constant of two references polymers are needed to measured a third one. Krayev *et al* [89, 90]

2005: Nanoscale Impedance Microscopy (NIM): Femtofarad (10^{-15}) resolution reached for capacitance images . Schneegans *et al* [83, 84]

2006: Nanoscale Capacitance Microscopy (NCM): Attofarad (10^{-18}) resolution reached for capacitance images . Gomila *et al* [69]

2007 (July): Local Dielectric Spectroscopy (LDS) developed under Ultra High Vacuum in the gradient mode: Frequency dependence of the dielectric losses of PVAc measured in one point. Israeloff *et al* [10, 11].

2007 (December): Dielectric constant measured in one point using NCM. Gomila *et al* [85]

2009 (March): Dielectric map of a biomembrane using NCM. Gomila *et al* [87]

2009 (July): Quantitative measurement in one point using the DC component of the force gradient (Chapter 4 of this thesis). Riedel *et al* [8]

2009 (September): Dielectric map of a biomembrane measuring the DC component of the force. Gomila *et al* [87]

2010 (January): Quantitative mapping of a nanostructured PS/PVAc polymer film using the DC component of the force gradient. (Chapter 4 of this thesis). Riedel *et al* [9]

2010 (May): Mapping of the dielectric losses of a PS/PVAc polymer film using LDS in the gradient mode. Riedel *et al* [9].

2010 (May): LDS of a PVAc film with inclusion of layered silicate. Massimiliano *et al* [91].

2010 (May): Quantitative measurement in one point using the modulus of the 2ω component of the force. Gomila *et al* [62]

2010 : Mapping of the dielectric losses of a nanostructured PS/PVAc polymer film using LDS in the force mode under ambient condition. (Chapter 5 of this thesis).

Conclusion on the generalities about EFM and the ECM

We have introduced the two dynamics modes that allows measuring topography with an AFM: the Amplitude Modulation (AM-AFM) and Frequency Modulation (FM-AFM). In AM-AFM the oscillation amplitude is used as a feedback parameter to measure the topography whereas in FM-AFM the cantilever is kept oscillating with a constant amplitude by fixing a small resonance frequency shift. AM-AFM and FM-AFM are usually realized under ambient condition and vacuum, respectively. These two modes permits to measure signals related with the electrostatic interaction during a scan at a given value of the tip-sample distance (EFM). The amplitude of the signal of the photodiode and the frequency shift can be related to the electrostatic force and force gradient, respectively.

The frequency shift as a function of the V_{DC} voltage curves exhibit a parabolic dependence:

$$\Delta f_0 \cong -\frac{f_0}{2k_c} G_{DC} = -\frac{f_0}{4k_c} \frac{\partial^2 C}{\partial z^2} V_{DC}^2 = -\mathbf{a}_{\Delta f_0}(z) V_{DC}^2$$

The ECM permits to calculate the parabolic coefficient $\mathbf{a}_{\Delta f_0}$ as a function of all the parameters of the experiment: tip-sample distance, thickness, radius of the tip and dielectric constant. In chapter 4, we will detail how the fit of $\mathbf{a}_{\Delta f_0}(z)$ allows obtaining a quantitative value of ϵ_r. The highest sensitivity of the method is obtained for small dielectric constant and thick sample. The simulated penetration depth of the electrostatic field inside the dielectric increases almost linearly with the tip-sample distance. For the classical condition of a tip having a 20 nm radius at a 20 nm distance of a dielectric, the electrostatic interaction is concentrated over the first 40 nm layer at the free interface (air or vacuum).

Working with a V_{AC} voltage at a ω_e frequency, it is possible to measure the phase shift of the $2\omega_e$ component of the force or force gradient using a lock-in. In chapter 5, we will use this quantity to study the temperature-frequency dependence of dielectric losses.

Chapter 4

Quantitative measurement of the static dielectric permittivity at the nanoscale

Summary

The aim of this chapter is to present two methods to measure quantitatively the low frequency limit, or static, dielectric permittivity ϵ_r. The first permits to obtain a value in one point while the second allows a quantitative mapping of the dielectric constant. We remind that (see previous chapter):

$$\Delta f_0 \cong -\frac{f_0}{4k_c}\frac{\partial^2 C}{\partial z^2}V_{DC}^2 = \mathbf{a}_{\Delta f_0}(z)V_{DC}^2 \tag{4.1}$$

Both methods are based on the measurement of the coefficient $\mathbf{a}_{\Delta f_0}(z)$ via the detection of the frequency shift while applying a V_{DC} voltage. The value of ϵ_r is then obtained using the numerical simulation of the Equivalent Charge Method (ECM). We will first introduce the preliminary common steps to these two methods. Then we will presents values of the dielectric constant measured in one point for a silicon dioxide and two polymer films of Poly(vinyl acetate) (PVAc) and Polystyrene (PS) at different temperatures. Finally, we will detail how we have been able to extend this method in order to obtain a quantitative dielectric map of a nano-structured polymer film composed by a matrix of PS with inclusions of PVAc.

1 Preliminary common steps

Experiments were realized under room condition in the AM-AFM mode with a Veeco Enviroscope™ equipped with a Lakeshore temperature controller. The free oscillating frequency f_0 was measured using the generic frequency sweep. The stiffness k_c was calculated using the so-called thermal tune method [92] based on the thermal noise measurement. The thickness of the sample h was measured by recording a topography in the tapping mode®over a cut in the sample. Frequency shifts were recorded using the double pass method.

1.1 The double pass method

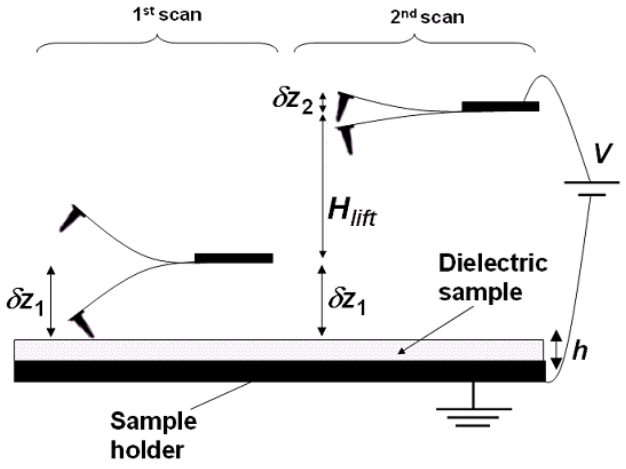

Figure 4.1 : *Principle of the double pass method. During the first scan topography is acquired. The tip is then retracted by a constant height H_{lift} and amplitude is reduced by a factor of about 3. During the second scan, a voltage V is applied on the tip and force or force gradient are detected.*

In the double-pass method (also called lift-mode) the topographic information is recorded during a first pass and the electrostatic signals are acquired during a second pass (Fig 4.1). During the second pass, the tip is retracted from the surface morphology by a constant height

H_{lift}, also called "lift height", and the amplitude of the tip vibration δz is reduced in order to stay in the linear regime (amplitude $\ll$ tip-sample distance). Typically, we divide the tapping amplitude by a factor 3. While the voltage V is applied to the tip (with the sample holder grounded) the electric force or force gradient is detected. As shown in Fig. 4.1 during the first scan, the average tip-sample distance z_1 is approximately equal to the oscillation amplitude ($z_1 \cong \delta z_1$). During the second scan, the distance is the sum of the first scan amplitude δz_1 and the lift height H_{lift} ($z_2 \cong \delta z_1 + H_{lift}$) and the cantilever oscillates with an amplitude of δz_2. This method has the key advantage to avoid any coupling between structural and dielectric informations, and to allow setting optimized conditions for electric measurements (linear regime).

1.2 Determination of the actual tip-sample distance

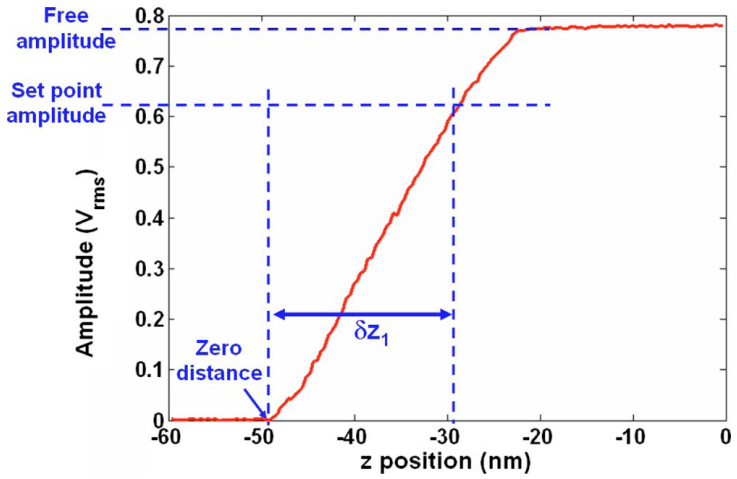

Figure 4.2 : *Typical amplitude-distance curve recorded on a stiff sample. The first scan amplitude δz_1 is equal to the difference between the z-position corresponding to the set point amplitude and the zero distance.*

The value of δz_1 ($\delta z_1 \simeq 20$ nm)is obtained by recording an amplitude-distance curve. A typical experimental curve is shown in Fig. 4.2; the slope of this curve gives the correspondence between the photodetector rms voltage and the real amplitude. Indeed, if there is no indentation of the tip into the sample, we can consider that amplitude is roughly equivalent to the distance. The zero distance corresponds to the point where amplitude becomes null. The tip-sample distance is calculated as the difference between the z-position of the actuator corresponding to the amplitude set point and the z-position corresponding to the zero distance. During the record of the amplitude-distance curve, the tip can be destroyed. We thus recommend to do it at the end of the experiments. Consequently, the adjustable parameter is the lift height. It can vary from positive to negative values, the minimum value corresponding to the height where the tip is in the contact with the sample.

1.3 Determination of the tip radius

This part of the experiment has to be performed on a conductive sample or substrate $h = 0$. The aim of this step is to extract the actual equivalent value of the tip radius R. $\Delta f_0(V_{DC})$ curves are recorded at several lift heights H_{lift}. A parabolic fit allows to extract the experimental coefficients $\mathbf{a}_{\Delta f_0}$ according to the real tip-sample distance. A value of the radius R is then obtained by fitting the $\mathbf{a}_{\Delta f_0}(z)$ curve with expression 4.1 in which the tip-sample capacitance is

calculated using the equivalent charge model (see previous chapter) without taking into account the insulating layer.

2 Measurement in one point

The protocol for the measurement of the dielectric constant ϵ_r in one point is similar to the one to determine the tip radius. The experiment is now preformed with a thin insulating layer of the material under study deposited on the conductive substrate. $\Delta f_0(V_{DC})$ curves are recorded at different lift heights H_{lift} and they are then analyzed in order to extract experimental coefficients $\mathbf{a}_{\Delta f_0}(z)$ for each lift height. Once R and h are known from previous experiments, we can fit the $\mathbf{a}_{\Delta f_0}(z)$ curve using expression 4.1 in which the capacitance is calculated by ECM, thereby we obtain the value of the dielectric permittivity ϵ_r.

2.1 Silicon oxide

a Sample preparation: Focused Ion Beam method

SiO_2 oxide has been provided by the The Nanotechnology Platform at the Parc Científic de Barcelona (PCB, Barcelona Science Park) using Focused Ion Beam (FIB). María Jesús López Bosque is acknowledged for the sample preparation and interesting discussions. FIB uses a gallium ion beam for localized ion etching of materials and also for localized depositions of distinct materials. The instrument allows the visualization and in situ control of the processes made using the dual beam facility, which combines the ion beam with an electron beam. Both beams are convergent at the same point, and form an angle of 52º. It is possible to make maskless ion etching and reactive ion etching of materials, and deposition of thin metal films (Pt and W) and thin insulating films (SiO_2). The technique also allows the deposition of 3D structures with a precision within a few tens of nanometers (30 nm). The apparatus is a Strata DB235 made by FEI Company. Our samples are similar to those studied by Fumagalli et al. [85]. They are composed of squares of 1μm side deposited on a gold layer. The average thickness of the SiO_2 layers was measured around 12 nm.

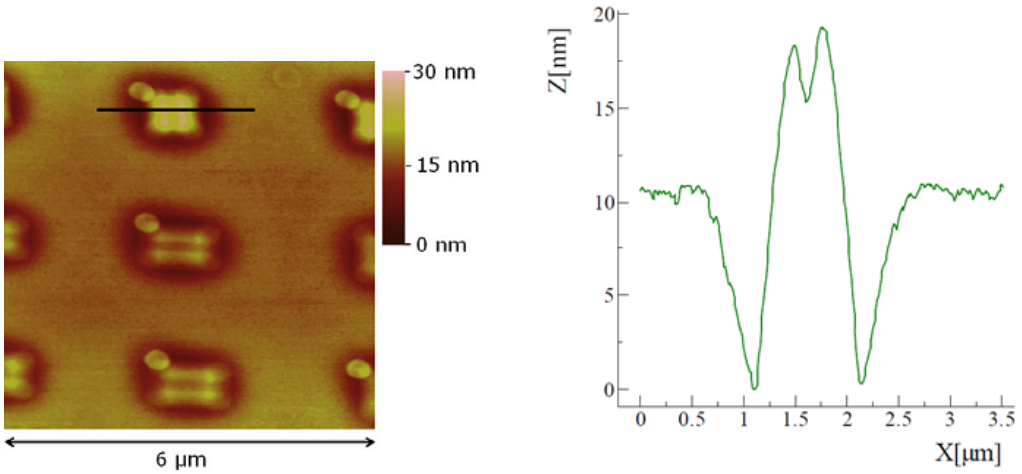

Figure 4.3 : *Topography of the Silicon Oxide sample measured by AFM*

b Results

Experiments were realized with a conductive diamond coated tips Nanosensors™ , CDT-FMR having a free oscillating frequency f_0=103 kHz and a stiffness k_c=5.9 N m^{-1}. In Fig. 4.4 a), we show the $\Delta f_0(V_{DC})$ curve obtained on the gold conductive sample in comparison with the curve obtained on the insulating oxide layer. Both curves were acquired at the same tip-sample distance z=31 nm. We observed that the parabolic profile in the presence of the oxide layer tends "to open" what is revealing a reduction in the local capacitance in accordance with Eq. 4.1. By fitting these curves using a parabolic function, we obtained $\mathbf{a}_{\Delta f_0}$ =31.7 Hz/V^2 for gold and $\mathbf{a}_{\Delta f_0}$ =27.8 Hz/V^2 for SiO2. In Fig. 4.4 a), we present the parabolic coefficients $\mathbf{a}_{\Delta f_0}$ as a function of the real tip-sample distance obtained on gold and SiO_2. The fit on gold allows to estimate the value of the effective radius of the tip R=105 nm in this case. Then, we calculated the value of the dielectric permittivity of the insulating layer by fitting the points obtained on SiO_2. We found $\epsilon_r = 4.5 \pm 1.1$, which is in agreement with the value obtained by Fumagalli et al. [85] on the same type of sample.

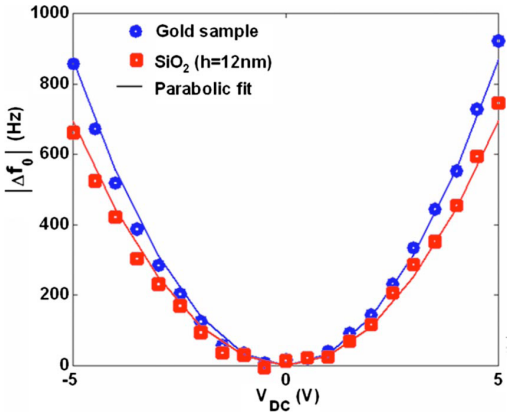

(a) *Parabolic profiles of $\Delta f_0(V_{DC})$ curves measured on a conductive gold sample (circles) and a SiO_2 /gold sample (squares) with h_{SiO_2}=12 nm.*

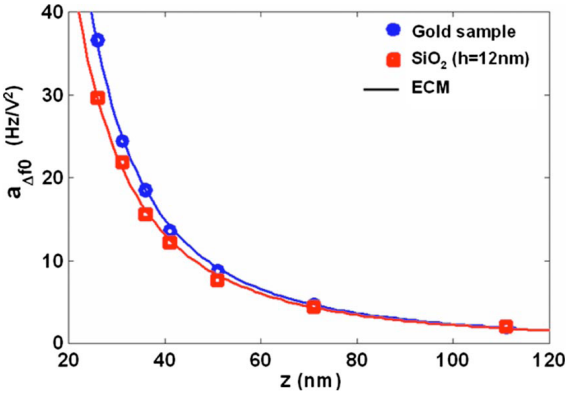

(b) *$\mathbf{a}_{\Delta f_0}(z)$ curves measured on a conductive gold sample (circles) and a SiO2 /gold sample (squares). Fits of the data by the ECM gives value of R = 105 ± 4 nm (Gold) and ϵ_r = 4.5 ± 1.1 (Oxide)*

Figure 4.4 : *Determination of the dielectric constant of silicon oxide at nanoscale*

2.2 PVAc & PS polymer films

a Sample preparation: Spin coating

Two polymer films of PVAc and PS have been prepared by spin coating. This simple process permits to obtain flat nanometric films. A solution of polymer in solvent is dropped on a substrate which is rotating at high speed in order to spread the fluid by centrifugal force. Rotation is continued for some time, with fluid being spun off the edges of the substrate, until the desired film thickness is achieved. The solvent is usually volatile, providing an instantaneous evaporation. As related in reference [93] the concentration of the polymer influences more the thickness than the speed rotation. We found in a rude approximation a linear relation between the thickness of the film and the concentration of polymer in solvent having a coefficient of about 60 nm/% for a rotational speed of 3000 round per minute (rpm). In order to measure precisely the thickness of the film we cut the polymer film with a sharp tool and measure the topography using the AFM.

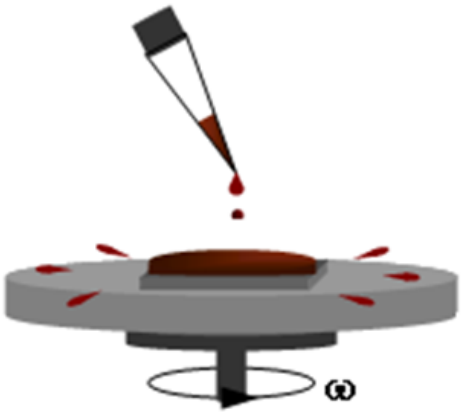

(a) *Schematic representation of the spin coating*

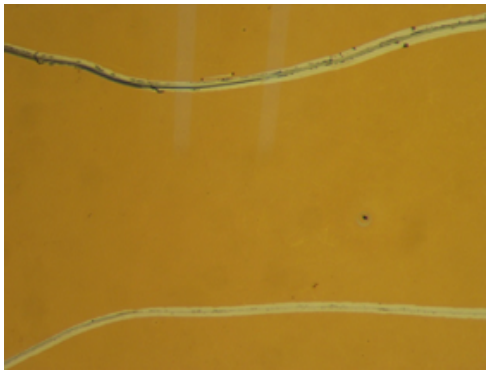

(b) *Resulting polymer film and cuts permitting to measure the height of the film. The black line indicates that the cut has removed the gold.*

Figure 4.5 : *Spin coating of polymer films*

b Results

The second series of experiments was performed on two ultra-thin polymer films. PS (weight average molecular weight M_w = 70950 g/mol) and PVAc (M_w = 83000 g/mol) were chosen because both their dielectric strength and their temperature dependence are very different for these two polymers. Additionally, the dielectric responses of both polymers have been previously well characterized in the literature [22, 27, 94] and in chapter 1. Samples were prepared by spin coating starting from solutions at 1% (w/w) in toluene. The substrate was composed of a fine gold layer deposited on a glass plate. The small percentage of polymer in solution was selected in order to obtain films with a thickness of about 50nm according to ref [93]. We used in this case standard EFM cantilevers (Nanosensors EFM) having a free oscillating frequency f_0 = 71.42 kHz and a stiffness k_c = 4.4 N.m$^-$1. The experiments were performed on neat PS and PVAc films at room temperature and at 70°C (Fig. 4.6). The measured thicknesses of the films were 50 ± 2 nm for PS and 50 ± 3 nm for PVAc at both room temperature and 70°C. The accuracy of our measurements does not allow detecting any thermal expansion. The experimental parabolic coefficients $\mathbf{a}_{\Delta f_0}(z)$ obtained for PS are shown in Fig. 4.6 a). Measurements at room temperature and at 70°C are very close indicating a weak temperature dependence of the dielectric permittivity as expected for this polymer. In addition, there is a big difference between the curves measured on gold and PS.We obtained the value of the tip radius R = 32 ± 2 nm and the dielectric permittivity of PS at 22°C and 70°C : 2.2 ± 0.2 and 2.6 ± 0.3. The experimental parabolic coefficients obtained for PVAc are shown in Fig. 4.6 b). We can note a significant difference between measurements realized at room temperature and at 70°C, i.e. below and above the glass transition temperature, Tg. At 70°C, the PVAc curve approaches the gold curve indicating an important increase of ϵ_r. By applying ECM, we obtained 2.9 ± 0.3 and 8.2 ± 1 for PVAc. The estimated values for PS and PVAc are in good agreement with the macroscopic ones reported in chapter 1 and reference [22, 27, 94]. The variation observed in the dielectric permittivity of PVAc is related with its strong dipole moment and the fact that PVAc crossed the glass transition temperature at around 38°C increasing the chain mobility and therefore the dielectric permittivity. Opposite, PS has a weak dipole moment and its T_g is around 105°C; therefore, a little or negligible variation of the dielectric permittivity is expected in this case.

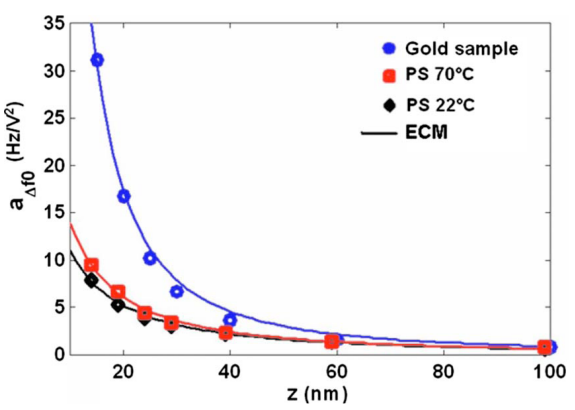

(a) $a_{\Delta f_0}(z)$ *curves obtained on a 50±2 nm PS thin film at 22°C (diamond) and 70°C (squares) in comparison with the curve obtained on a gold sample (circles). The tip radius is measured at* $R = 32 \pm 2$ *nm. Fitting PVAc parabolic coefficients using ECM, we obtained* $\epsilon_r = 2.2 \pm 0.2$ *at 22°C and* $\epsilon_r = 2.6 \pm 0.3$ *at 70°C.*

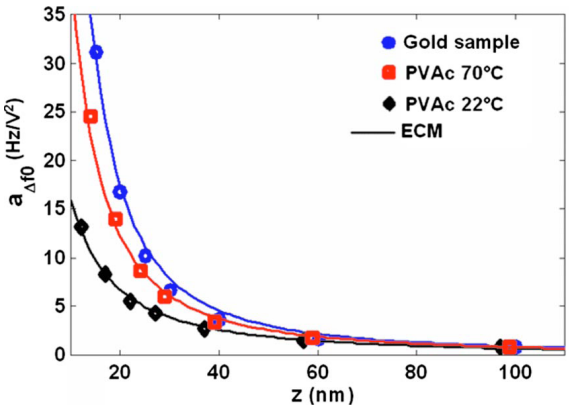

(b) $a_{\Delta f_0}(z)$ *curves obtained on a 50±2 nm PVAc thin film at 22°C (diamond) and 70°C (squares) in comparison with the curve obtained on a gold sample (circles). The tip radius is measured at* $R = 32 \pm 2$ *nm. Fitting PVAc parabolic coefficients using ECM, we obtained* $\epsilon_r = 2.9 \pm 0.3$ *at 22°C and* $\epsilon_r = 8.2 \pm 1$ *at 70°C.*

Figure 4.6 : *Determination of the dielectric constant of ultrathin PVAc and PS films at the nanoscale*

3 Mapping of the dielectric constant of a nanostructured PS/PVAc film

The second step of this work was to study the morphology and dielectric properties of an immiscible blend of PS and PVAc. The sample film was prepared from a solution of the polymers (1% w/w in toluene with 75% PS w/w and 25% w/w PVAc). The solution was subsequently spin coated on a conductive gold substrate at 3000 rpm. The film exhibits a nodular morphology of PVAc in a continuum phase of PS (Fig 4.7). The nodules of PVAc have a mean height measured by AFM around 50 nm and the PS has a homogeneous thickness t_0 of around 27 nm. At room temperature both polymers present similar dielectric permittivity, but they are substantially different above 50 °C providing a good dielectric contrast. Experiments were

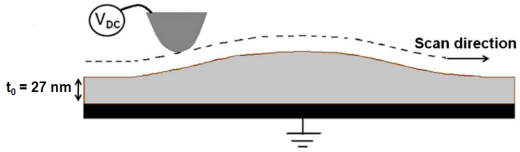

(a) *Typical topographic profile of PVAc islands in a PS matrix. Both tip and polymer film are represented at the same scale. The dash line represents the tip motion during the second scan.*

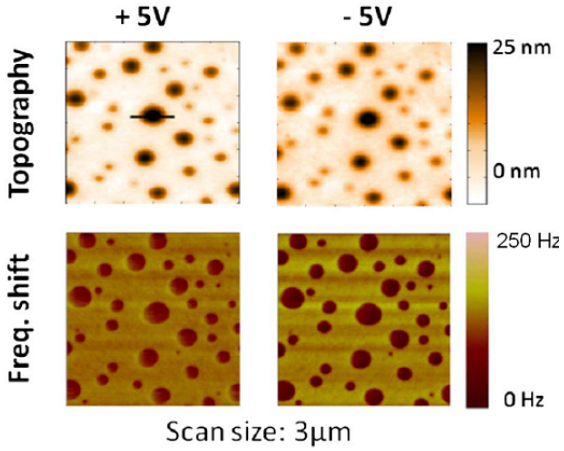

(b) *Topography and frequency shift measured by the double pass method at +5 and -5 V on the PVAc/PS films. The black line corresponds to the profile appearing in a)*

Figure 4.7

carried out with a standard Pt-Ir coated tip (Nanosensors EFM). The cantilever free resonance frequency was $f_0 = 70.13$ kHz and the stiffness $k_c = 4.5$ N m^{-1} The tip radius was measured at R = 19 ± 2 nm. In order to preserve the tip from wear, all the experiments were carried out in a very soft tapping mode. When recording the topography signal, during the first scan, the tip was carefully maintained in a light attractive regime (negative mechanical phase shift of the cantilever oscillation). We checked that after several series of measurements the tip radius did not increase significantly, as expected for EFM polymer characterization.

Frequency shifts were measured by means of the succession of two double pass scans at a fixed value of the tip-sample distance, $z_0 = 18 \pm 2$ nm, and applying two different voltages of +5 and -5 V (Fig. 4.7 b)). When the surface is characterized by a zero contact potential, only a single double pass scan is necessary to implement our method. However, we recommend doing two double pass scans in order to verify the good accuracy of the measurements and to check the symmetry of the parabola with respect to the 0 V axis. We note that the applied DC voltage can influence the bending of the cantilever and hence can induce notable variations of the tip-sample distance. In our experiments, we estimate a 2 nN maximum force acting on the cantilever, giving a precision of the tip-sample distance of $\sim 2\%$. In the present study, due to the absence of free charges, the frequency shift at a zero voltage is found to be nearly

null in the scanned area. In order to ensure that the two frequency shifts correspond to the same sample point, the topography of the two images at different biases should be as similar as possible (Fig. 4.7 b)). However, working at 70 °C a non-negligible drift is observed. Translation effects have been numerically corrected by the introduction of a correlation function. Note that, as the height is an important parameter to calculate ϵ_r, images have to be properly flattened using only the topography information from the PS matrix. Using these two measurements and assuming a zero-frequency shift for a zero voltage applied, we can calculate the coefficient $\mathbf{a}_{\Delta f_0}$ at each point of the topographic image.

Figures 4.8 a) and 4.8 b) present the topography and the corresponding map of the coefficient $\mathbf{a}_{\Delta f_0}$, respectively. The height of the polymer h is equal to the topography measured in Fig. 4.8 a) plus the homogeneous thickness of the matrix: h = t_0 + t.

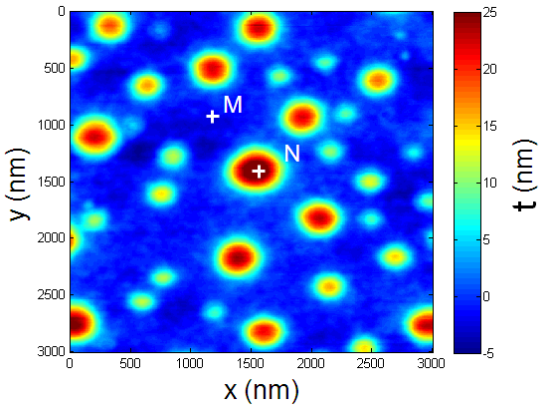

(a) *Topography of the PVAc/PS film.*

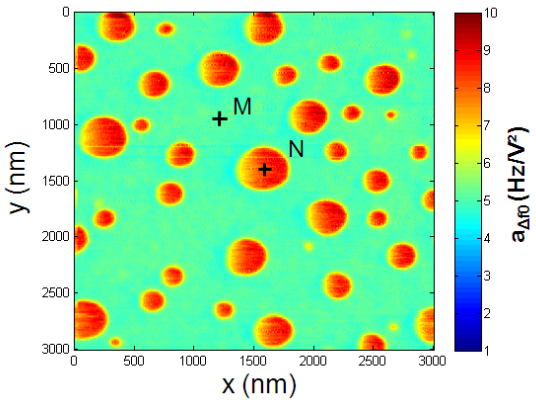

(b) *Corresponding map of the coefficient $\mathbf{a}_{\Delta f_0}$. Values of t and $\mathbf{a}_{\Delta f_0}$ at points M (PS matrix) and N (PVAc nodule) have been reported in Fig. 4.9 where they have been interpolated with ECM simulated curves in order to extract the corresponding value of ϵ_r*

Figure 4.8

In the general case, in order to take into account the nonzero surface potential potential V_{cp}, a third image has to be recorded at another applied voltage (for example, at 0 V). A map of the parabolic coefficient $\mathbf{a}_{\Delta f_0}$ could be obtained from frequency shift images using the equation $\Delta f = \mathbf{a}_{\Delta f_0}(V_{DC} - V_{cp})^2$.

Using the ECM, we are able to calculate $\mathbf{a}_{\Delta f_0}(h, \epsilon_r)$ (Fig. 4.9). After successive interpolation, we can obtain the value of ϵ_r in each point of the image (Fig. 4.10). As an example, points M (PS) and N (PVAc) in Figs. 4.9 and 4.8 are characterized by h(M) = 27 ± 2 nm, $\mathbf{a}_{\Delta f_0}$ = 5.2 ± 0.3 Hz/V^2 and h(N) = 50 ± 2 nm, $\mathbf{a}_{\Delta f_0}$ = 7.8 0.7 Hz/V^2, respectively. After successive interpolations between different $\mathbf{a}_{\Delta f_0}(h, \epsilon_r)$ curves, we found ϵ_r = 2.3 ± 0.3 for PS and ϵ_r = 7.5 ± 1 for PVAc, values in agreement with the ones previously reported and literature [22, 27, 94].

Fig. 4.10a) shows a quantitative map of the dielectric constant of the PVAc/PS film at the nanoscale. The small asymmetry observed on the islands of PVAc (on the x axis) is most likely attributed to the scanning process (only retrace signal was recorded). We estimate an upper limit of the spatial resolution Δ x around ≃ 30 nm, which corresponds to half the distance necessary to achieve the transition between the dielectric level of the island of PVAc and the

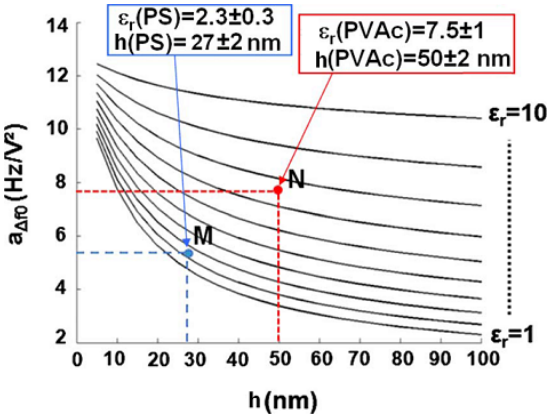

Figure 4.9 : *Numerical simulations based on ECM of the curves $\boldsymbol{a}_{\Delta f_0}(h, \epsilon_r)$, where h is the sample thickness and ϵ_r is the relative dielectric permittivity, for a tip radius R = 19 nm and a tip-sample distance z_0 = 18 nm. M(h,$\boldsymbol{a}_{\Delta f_0}$) and N($h$,$\boldsymbol{a}_{\Delta f_0}$) are typical points obtained from AFM topography and EFM images (Fig. 4.8), respectively, on the PS matrix and the PVAc nodules of the studied polymer blend thin film. ϵ_r can be deduced by interpolating these points with simulated curves.*

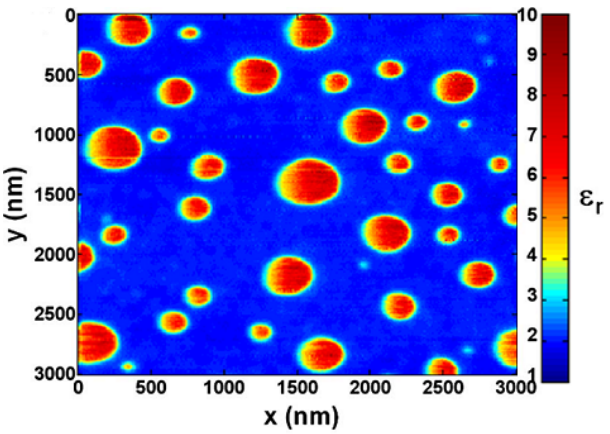

(a) *Map of the dielectric constant of the PVAc/PS film obtained by processing images shown in Fig. 4.8.*

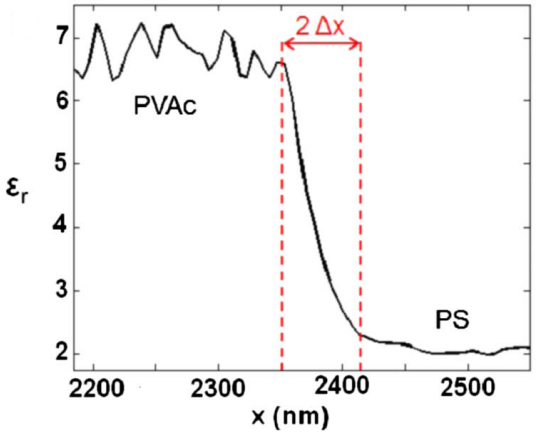

(b) *Typical profile of the dielectric permittivity across the PVAc/PS interface.*

Figure 4.10 : *Map of the dielectric constant of a nanostructured PS/PVAc film*

matrix of PS (Fig. 4.10b)). This value is in good agreement with the theoretical one calculated on the basis of the tip-sample electrostatic interaction [77, 78]: $\Delta x = (Rz_0)^{1/2} \simeq 20$ nm. This result shows that PS and PVAc are immiscible at scale equal or lower than 30 nm. The direct confrontation of the topography with the dielectric map (Fig. 4.8a)) and (Fig. 4.10a)) points out that small satellite nodules (around 20 nm) are detected in the dielectric map and not in the topography, thus showing the high sensitivity of this method.

Conclusion on quantitative measurement of the static dielectric permittivity at the nanoscale

We have developed a method that permits to measure quantitatively the static dielectric permittivity ϵ_r at the nanoscale. The measurement is based on the detection of the parabolic coefficient of the frequency versus voltage curves, $\mathbf{a}_{\Delta f_0}$ using EFM. $\mathbf{a}_{\Delta f_0}$ is function of the tip-radius, tip-sample distance, thickness and dielectric constant of the sample. A preliminary step is needed to determine the geometrical parameters of the system before quantifying the dielectric constant. The thickness is measured from a topography of the sample and the actual tip-sample distance from an amplitude distance curve. The ECM permits to calculate $\mathbf{a}_{\Delta f_0}$ as a function of all parameters. The fit of $\mathbf{a}_{\Delta f_0}(z)$ over a metallic surface permits to measure the tip-radius. Once these parameters have been determined, the method permits either a quantification of ϵ_r from measurement in one point or a mapping of dielectric constant at the nanoscale.

The quantitative value of ϵ_r in one point is obtained by fitting the experimental $\mathbf{a}_{\Delta f_0}(z)$ points measured over the dielectric. The first measurement has been realized on a silicon oxide, well characterized at both macro and nanoscale by other methods. We found a value of $\epsilon_r = 4.5 \pm 1.1$ in good agreement with literature. We have then measured the dielectric constant of thin (thickness around 50 nm) PVAc and PS polymer films at different temperatures. The value here summarized are in accord with the macroscopic ones previously reported in this manuscript and in the literature.

Sample	PS		PVAc	
ε_r	T=22°C	T=70°C	T=22°C	T=70°C
	2.2 ± 0.2	2.6 ± 0.3	2.9 ± 0.3	8.2 ± 1

The variation observed in the dielectric permittivity of PVAc is related with its strong dipole moment and the fact that PVAc crossed the glass transition temperature at around 38°C increasing the chain mobility and therefore the dielectric permittivity. Opposite, PS has a weak dipole moment and its T_g is around 105°C; therefore, a little or negligible variation of the dielectric permittivity is expected in this case.

The method has then been extended to obtain a quantitative map of the dielectric constant. By mapping the sample at 3 different voltages (-5V, 0V and 5V) we have been able to obtain a map of $\mathbf{a}_{\Delta f_0}$. A modification of the numerical script previously used allows a quantification of the dielectric constant from the topography and $\mathbf{a}_{\Delta f_0}$ maps. Measurements carried on a nanostructured PS/PVAc film gives values in good agreement with both macroscopic and "in one point" measurement. The spatial resolution has been measured to 40 nm, a value close to the theoretical limit. This method can be used with any standard AFM in ambient condition.

Chapter 5

Measurement of the frequency dependence of the dielectric permittivity at the nanoscale

Summary

In this chapter, we present two methods to measure the temperature frequency dependence of the dielectric permittivity. In the gradient mode the signal measured is the mechanical frequency shift, in the force mode the signal is the amplitude of vibration and comes directly from the photodiodes. Both methods are based on the detection of the phase shift in the 2 ω component between the signal measured and the electrical excitation ($\Phi_{2\omega e}$). Force and force gradient being a function of the dielectric permittivity, any measurable dielectric losses in the material will be detected as a phase shift. This phase shift is related with the well-known loss angle $\tan(\delta)$ measured by Broadband Dielectric Spectroscopy (BDS); but has still not been quantified at this day. We will present two experiments:
- The frequency sweep in one point that permits to access to the frequency dependence the dielectric permittivity.
- An imagery mode at a given frequency that allows mapping the dynamics with dielectric compositional contrast.
The interest of this Local Dielectric Spectroscopy (LDS) is its spatial resolution and penetration depth of few tens of nanometers that would permits to measure difference between bulk and local dynamics. The experimental protocol will be detailed in the "FM-EFM measurements in the gradient mode" section. Then we will present results obtained on a model nano-structured polymer film composed by a matrix of PS with inclusion of PVAc. In the "AM-EFM measurements in the force mode", we will introduce a multi-frequency study of the same kind of nano-structred film before comparing the dynamics measured at macroscopic scale using BDS with the ones measured in a pure PVAc film and in the nano-structured system. The effects of the experimental parameters (thickness, tip-sample distance) on the shape of the difference of phase will be discussed.

1 FM-EFM measurements in the gradient mode

Experiments were carried out by FM-EFM under Ultra High Vacuum (UHV) with a variable temperature stage (RHK UHV 350). The temperature was measured with a small thermocouple clamped to the sample surface. A classical EFM conducting cantilever with 25 nm tip radius was used. In FM-EFM, the cantilever is oscillated at its resonance frequency, $f_0 = 70$ kHz, and the resonance frequency shift Δf_0, due to tip-sample interaction forces, is detected with very high resolution using a Nanosurf Easy Phase Locked Loop (PLL) detector. This parameter is used as a feedback for controlling the tip-sample distance z. Additional signals are those measured as a result of the electrodynamics interaction between the conducting tip and the polymer sample. The 2 ω_e component of the force gradient can be detected via the frequency shift of the cantilever by using a lock-in amplifier (Stanford Research SR-830).

1.1 Experimental protocol

The principle of the frequency sweep is detailed in reference [10, 11]. It consists in recording the phase in one point at different frequencies and constant temperatures. During the acquisition of the dielectric spectrum, the feedback of the PLL detector (typically $\Delta f_0 = 15$ Hz) was turned off in order to avoid any coupling with the corresponding electrical frequency. We apply a $V_{AC} = V_0 sin(\omega_e t)$ voltage at different frequencies varying from 0.1 to 120 Hz. We mention the fact that the frequency range is limited at low frequencies by the time of acquisition and at high frequencies by the bandwidth of the microscope's electronics. The detector introduces an intrinsic reponse in the signal. A preliminary step consists in measuring this reference phase in the $V_{2\omega_e}$ over a metallic substrate or any material without any measurable dielectric relaxation (Fig. 5.1). The difference between this reference phase and the phase measured in the

experiments, $\Delta\Phi_{G,2\omega e}$, is used to characterize the dielectric dissipation. During the relaxation, due to the loss of energy to align the dipoles in the field, a peak is observed in $\Delta\Phi_{G,2\omega e}$. An

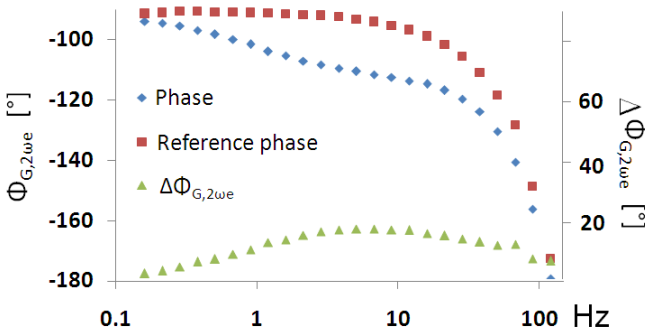

Figure 5.1 : *Measurement of the reference phase (over a metallic or a glassy substrate) the phase measured over the polymer (here PVAc) and* $\Delta\Phi_{G,2\omega e}$

example is shown in Fig. 5.1 where are represented the reference phase Φ_{ref}, the phase measured over a film of PVAc and the resulting $\Delta\Phi_{G,2\omega e}$.
From the measurement of $\Delta\Phi_{G,2\omega e}$, we can define V' and V", related with the real and imaginary part of the dielectric permittivity:

$$V' \propto A(\omega)/A_{ref}(\omega)(\cos(\Delta\Phi_{G,2\omega e}) \tag{5.1}$$
$$V'' \propto A(\omega)/A_{ref}(\omega)\sin(\Delta\Phi_{G,2\omega e}) \tag{5.2}$$

where $A(\omega)$ and $A_{ref}(\omega)$ are the amplitude recorded over the sample and the reference, respectively. These two quantities are similar to ϵ' and ϵ" measured by BDS (Fig. 5.2) and a model is needed to get quantified values. In this context, we have chosen to work with the physical measurable quantity $\Delta\Phi_{G,2\omega e}$.

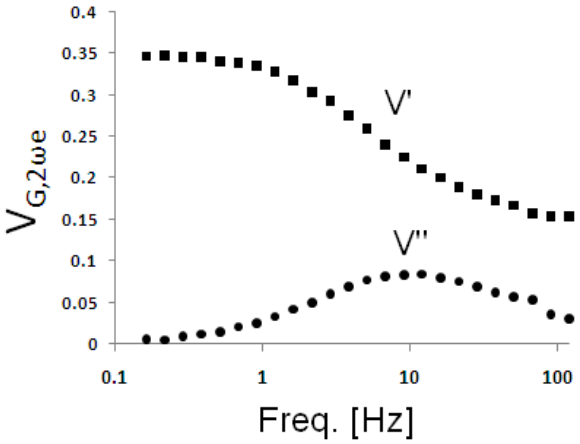

Figure 5.2 : *Real (V', square) and imaginary (V", circle) part of the dielectric response measured by Local Dielectric Spectroscopy*

1.2 Temperature-frequency dependence of a PS/PVAc film in the gradient force

We have chosen to study the same kind of PS/PVAc polymer film used in chapter 3. The topography is still characterized by a 25 nm thick matrix with island-like features having an average diameter of about 500 nm and a maximum height of about 25 nm above the reference level of the matrix (Fig. 5.3). In the investigated range of frequency (0.1 - 120 Hz) we expect to detect the dielectric alpha-relaxation of PVAc slightly above its glass transition temperature: $T_g \simeq 38$°C. Therefore we have explored the temperature range between 25°C and 50°C in order to follow the evolution of this dynamic process. The T_g of PS being $\simeq$105°C, no measurable relaxation is expected in our range of temperature and frequency. As mentioned in chapter 2 and 4, these two polymers are immiscible, even at the nanoscale and form phase separated domains. Fig. 5.4 shows $\Delta\Phi_{G,2\omega e}$ over an island at different temperatures. The fitting lines

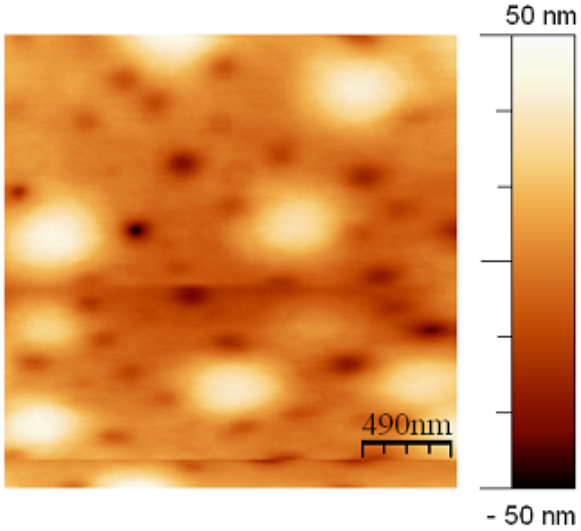

Figure 5.3 : *Topography of the thin PS/PVAc polymer film. The thickness of the matrix is approximately 25 nm, whereas islands rise to 50nm from the substrate.*

were obtained using a Kohlrausch-Williams-Watts response function ($exp(-t/\tau)^\beta$ see Eq. 1.50) as a convenient way to describe the experimental results. Maximum value of $\Delta\Phi_{G,2\omega e}$ and shape parameter (β=0.42) were fixed by fitting the data measured at 40°C. Keeping these parameters constant and using only a free timescale parameter we obtained a rather satisfactory description of the data, ie, the shape of the peak does not depend on temperature within the uncertainties. Measurements at the same temperatures have been performed over the matrix and the response (not shown) is always flat ($\Delta\Phi_{G,2\omega e} < 0.1°$). Therefore, the frequency spectrum permits to characterize locally the dynamical properties of the sample, which shows that the matrix is composed of PS whereas islands are dynamic domains of PVAc, in agreement with Fig. 4.10. The second experiment involved scanning the sample surface while a 50 Hz V_{AC} is applied to the tip. In order to keep a constant tip-sample distance, the feedback of the PLL is used during the scan. Fig. 5.5 presents images of $\Delta\Phi_{G,2\omega e}$ recorded at different temperatures. All images have been offset to the same phase-shift color scale using WSxM [95]. The phase recorded on the flat matrix areas is always near 0, as expected for PS. On the other hand all values measured on the PVAc islands are, within experimental errors, the same as those measured using the frequency sweep in one single point at 50 Hz (Fig. 5.4). At 25°C, the image is homogeneous: there is no dielectric relaxation occurring in the islands of PVAc. This demonstrates that this method is only sensitive to dipolar relaxation and not topographical effects. When the temperature is

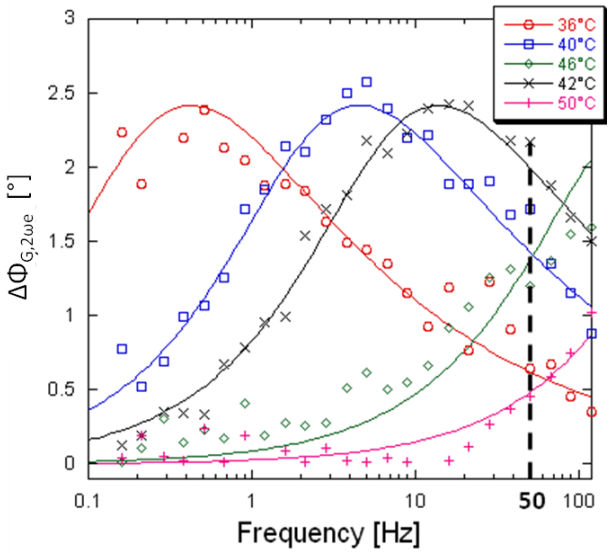

Figure 5.4 : *Phase shift measured as a function of the frequency over an island of PVAc. Statistical error is 0.25 for $f > 1$Hz and 0.35 for $f < 1$ Hz. Lines are fits derived from a KWW model with amplitude and shape parameters fixed for all curves. The dashed line indicates the imaging frequency at 50 Hz of Fig 5.5.*

increased to 36°C we begin to see a strong contrast in the images as the high frequency wing of the dielectric loss peak starts to contribute at 50 Hz in the PVAc regions. The maximum contrast is found at 42°C. Further increasing the temperature reduces the contrast as the loss peak shifts to higher frequencies and only the lower frequency contributions are detected. As the shape of the relaxation does not depend significantly on temperature, the contrast observed is only attributed to the passage of dynamics associated with the alpha-relaxation through our measurement window. Fig. 5.6 shows the profile of the phase recorded at 42°C across the interface between a PVAc island and the PS matrix (as shown in Fig. 5.5). We can estimate an upper limit of the spatial resolution (corresponding to half of the distance necessary to achieve the transition between the dielectric level of PVAc and PS) Δx around $\simeq$ 40 nm. This corresponds to the state-of-the-art resolution in EFM imaging when using standard probes, and it is also close to the theoretical resolution under our working conditions [77, 78].

Values of $\Delta\Phi_{G,2\omega e}$ measured by frequency sweep (Fig. 5.4) and using a profile (Fig. 5.6) are in good agreement:

T [°C]	36	40	42	46	50
$\Delta\Phi_{G,2\omega e}$ **Freq. Sweep** [°]	0.6	1.7	2.2	1.2	0.5
$\Delta\Phi_{G,2\omega e}$ **Profile** [°]	0.7	1.8	2.6	1.5	0.5

Table 5.1 : *Comparison of $\Delta\Phi_{G,2\omega e}$ measured by frequency sweep in one single point and extracted from an image profile. Statical error is measured to 0.25°*

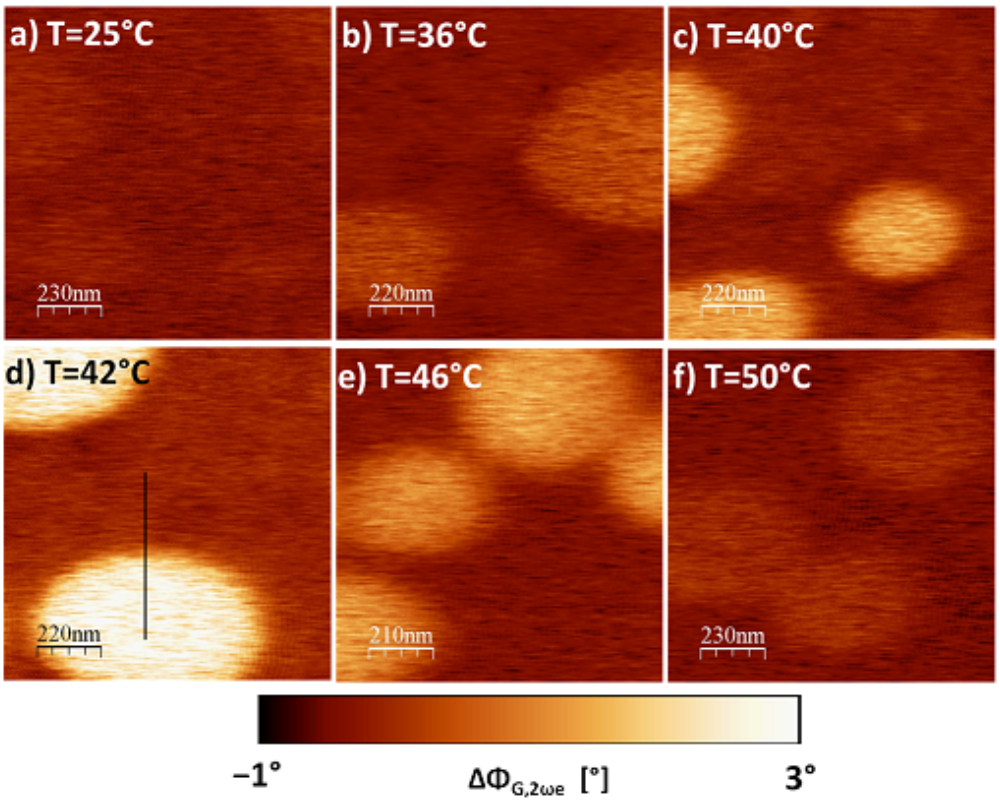

Figure 5.5 : *Image of the phase shift recorded at 50 Hz on a PS/PVAc film at various temperatures. Brighter areas correspond to higher losses, indicative of segmental relaxation on ∼ 3 ms time scales in PVAc. The profile recorded on the black line at 42°C is shown on Fig. 5.6.*

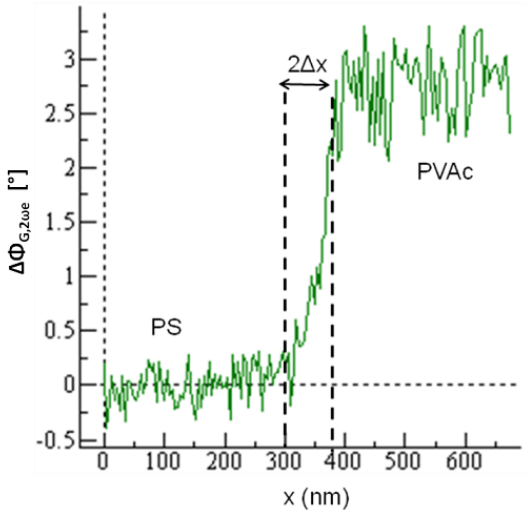

Figure 5.6 : *Profile of the phase shift recorded at 50 Hz and 42° (as shown in Fig. 5.5 d). The phase jump at the PS/PVAc boundary gives an estimated lateral resolution, $\Delta x \sim 40$ nm. The value of the phase shift is measured around 2.6°*

2 AM-EFM measurements in the force mode

In this section we present results obtained using AM-EFM. In this mode we have been working directly with the amplitude of vibration, in the force mode. These observations are of great relevance because they demonstrate for the first time that FM-EFM and vacuum are not necessary to measure the dynamic dielectric response. This is particularly important to study bio-materials. Such studies can be implemented using standard commercial devices under ambient conditions. Measurements have been realized with a Veeco Multimode V SPM and the temperature was set by a Thermal Application Controller (TAC). The holder was a classical EFM holder (that does not permits to regulate the temperature) and the temperature has been measured afterward by a small thermocouple clamped on a reference sample. Temperatures set to the TAC have been corrected into nominal temperatures actually measured by the thermocouple. The protocol is the same than the one explained in previous section: The difference between a reference phase measured on a sample having no dielectric response and the phase measured over the polymer $\Delta\Phi_{F,2\omega e}$ is used to characterize the material. In a first time, we have chosen to study the same kind of nanostructured PS/PVAc film. Then we will present results obtained on a poly(methyl methacrylate) (PMMA) film before discussing the shape of $\Delta\Phi_{F,2\omega e}$ as a function of the experimental parameters.

2.1 Temperature-frequency dependence of a PS/PVAc film in the force mode

Images recorded by the nanoscope software on the external channel coming from the lockin are presented in volts. The first step is to convert these volts into degrees. The reference phase measured on a conductive material when detecting the force has the same shape than the one measured previously in the gradient mode (Fig. 5.1). In order to calculate the factor of conversion from the lock-in to the nanoscope, we have plotted the signal in volt given by the nanoscope software as a function of the degree printed by the lockin while recording a reference phase (Fig. 5.7). Images have subsequently been rescaled in degree using WSXm [95].

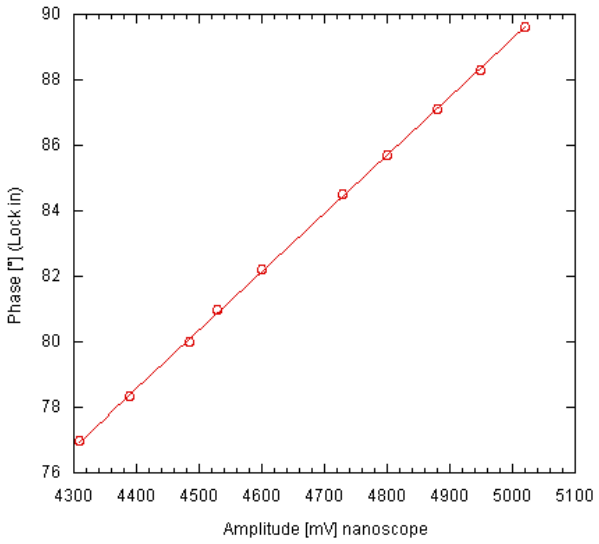

Figure 5.7 : *The conversion factor from the lock-in to the nanoscope controller is measured to 18°/V.*

We have realized maps of $\Delta\Phi_{F,2\omega e}$ over the same kind of PS/PVAc sample previously presented, having a thickness of about 250 nm. Fig. 5.8 presents maps recorded at different

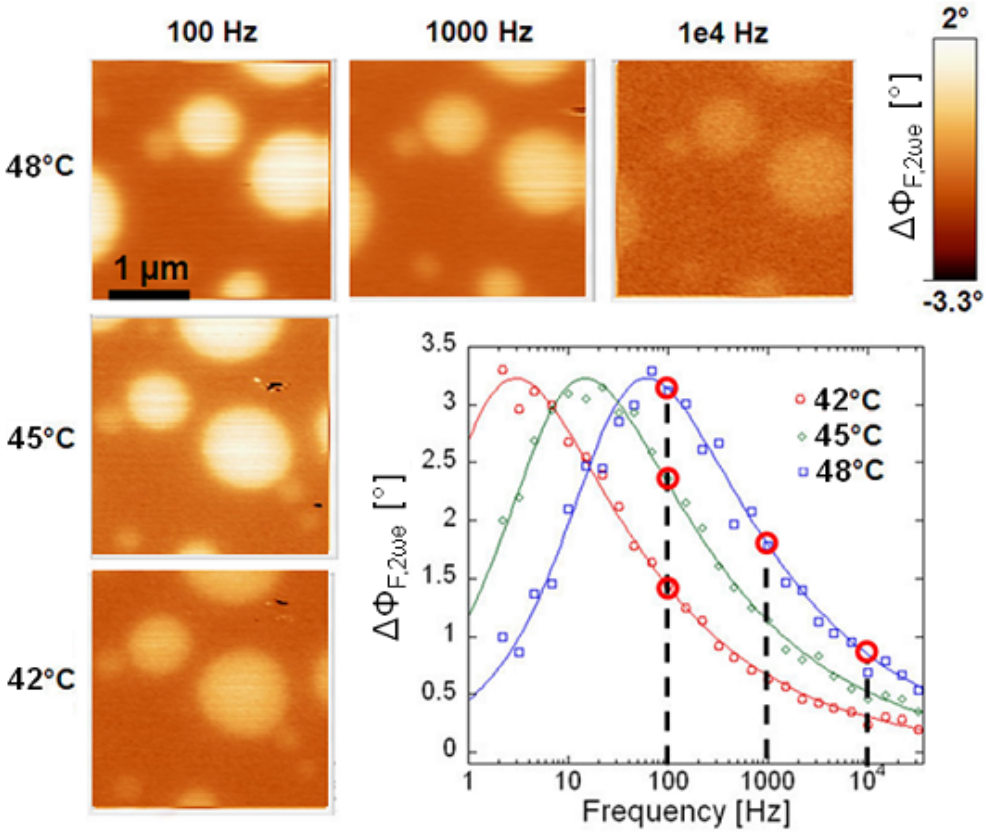

Figure 5.8 : *AM-EFM images of $\Delta\Phi_{F,2\omega e}$ recorded on a thin PS / PVAc blend sample. In line, images at a fixed temperature and at different frequencies. In column, images at a fixed frequency and different temperatures. Values of frequencies and temperature are in good agreement with single point measurements on PVAc shown in the inset. A maximum of contrast is obtained when crossing the alpha-relaxation of PVAc.*

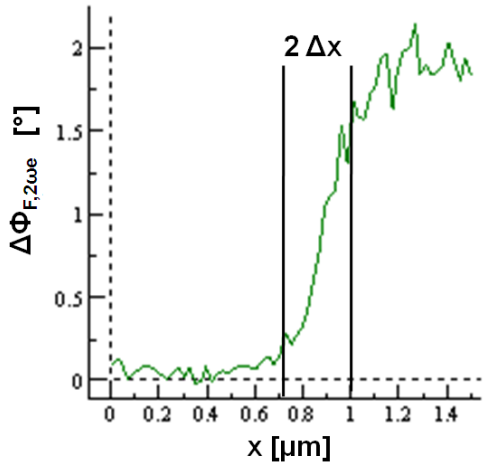

Figure 5.9 : *Profile of the phase shift recorded at 100 Hz and 48°C. The phase jump at the PS/PVAc boundary gives an estimated lateral resolution, $\Delta x \sim 150$ nm.*

temperatures and frequencies. The images are in good agreement with the frequency sweep measured in one point (inset). The high frequency limit is around 35 kHz, value close to the half of the resonance frequency. As we are working on the 2 ω component, this number tends to show that the high frequency limit is fixed by the mechanical resonance frequency.

Fig. 5.9 represents the profile recorded at 48°C and 100 Hz. The lateral resolution is measured around 150 nm. According to theoretical work [78] the ratio between the lateral resolution in force and gradient mode would be close to 1.4. As the aim of this measurement was not to be quantitative we did not measure the radius of the tip or the tip-sample distance. Just as the case of the gradient mode, we hope to reach lateral resolution close to theoretical limits. In order to get a proper comparison, measurements should be repeated in the very same experimental conditions.

In chapter 1, we have constated (Fig. 2.8) that the dynamics in the blend of PVAc/PS was slightly faster and broader than in the pure bulk of PVAc. This phenomena could be attributed to compositional heterogeneities, interface's effects. In Fig. 5.10 we constat that within the uncertainty of our measurement, the dynamics is the same in a pure PVAc film than the one measured in an island of PVAc. The thicknesses of the films were of about 250 nm and the temperature close to 48°C. Although preliminary, this result tends to show the that the local dynamics inside PVAc domains is not affected by the matrix of PS.

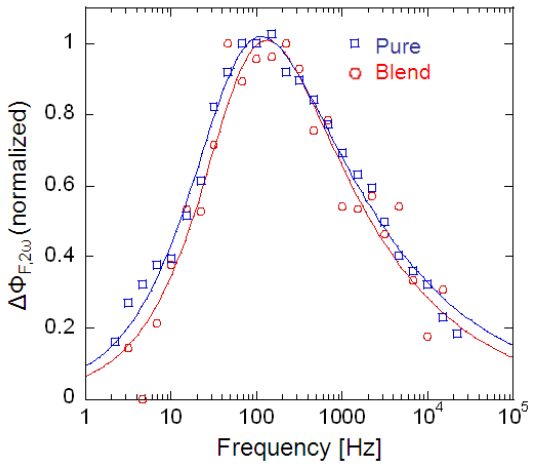

Figure 5.10 : *Comparison of the dynamics measured locally by LDS in a pure PVAc film and in an island of the blend with PS. The dynamics are measured at the same timescale, within uncertainties.*

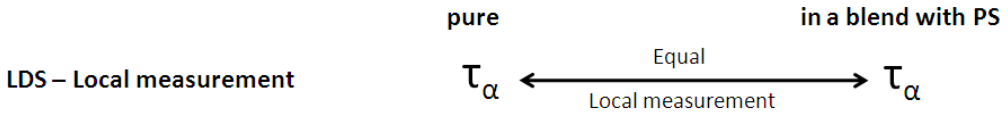

Figure 5.11 : *Schematic comparison of the relaxation time measured by LDS for PVAc pure and in a blend with PS. For a given temperature, the same timescale is measured locally in the pure PVAc film than in a domain of PVAc surrounded by the matrix of PS.*

Fig. 5.12 is a relaxation map of PVAc measured locally by LDS and macroscopically by BDS. The plot presents the frequency of the peak in $\tan(\delta)$ and $\Delta\Phi_{F,2\omega e}$. We have to take a great care

while comparing the relaxation time measured by these two different techniques. BDS probe the dynamics macroscopically over the all sample whereas LDS mainly probe the first layer (of about 40 nm) at the free interface. We will assume that the temperature measured on the thermocouple clamped at the surface of the sample is representative of the actual temperature where the dynamics is probe in the sample. Finally, the last hypothesis needed to make a comparison is that for a same system, i.e. the same dynamics probe, BDS and LDS would measure the same relaxation time. Fig. 5.12 shows, in agreement with [11], that the local dynamics is faster than the bulk one. These results could be interpreted as a speeding up in the α-relaxation time related with a small decrease in the dynamical T_g at the near surface of polymer films [11]. This decrease in T_g at the free interface of a thin polymer film has also been measured by fluorescence [96], and neutron reflectivity [97]. It has also been shown using Brillouin light scattering [98], that the T_g of a polymer film decreases with thickness. This phenomena has been attributed to unambiguous effect of the free surface on T_g of thin polymer film [98].

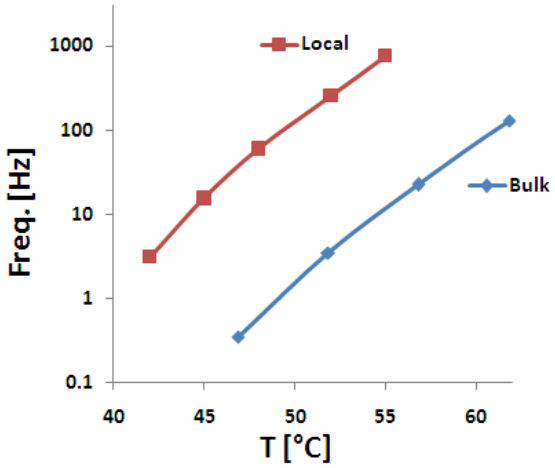

Figure 5.12 : *Relaxation map of PVAc measured locally by LDS and macroscopically BDS. The local relaxation is faster than the one measured in the bulk.*

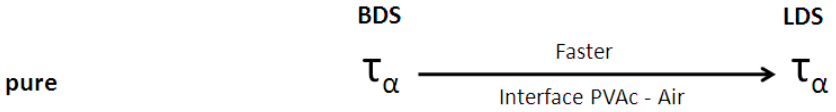

Figure 5.13 : *Schematic comparison of the relaxation time measured on a pure PVAc film by LDS and BDS. For a given temperature, the dynamics measured by LDS is faster than the bulk one measured by BDS. One possible hypothesis could be related with a decrease in T_g at the free interface.*

2.2 Qualitative shape analysis: Influence of the thickness and the tip sample distance

— One example: PMMA

As already mentioned in the introduction of this chapter, the difference of phase $\Delta\Phi_{F,2\omega e}$ has not yet been quantified. Therefore the comparison between frequency spectra of the dielectric losses measured macroscopically and at the nanoscale can only be qualitative. The β-relaxation of poly(methyl methacrylate)(PMMA) is interesting because it occurs slightly above room temperature in our range of frequency and the intensity of the dielectric losses increases with temperature. Therefore, we have studied and compared this relaxation measured by BDS and LDS around the same timescales (Fig. 5.14). We see that LDS permits to detect the increase in the maximum intensity of $\Delta\Phi_{F,2\omega e}$ in agreement with BDS measurements. Therefore LDS allows measuring the same relative variation in the intesity of dielectric losses. We will then study the influence of the different parameters of the experiment on the shape of $\Delta\Phi_{F,2\omega e}$.

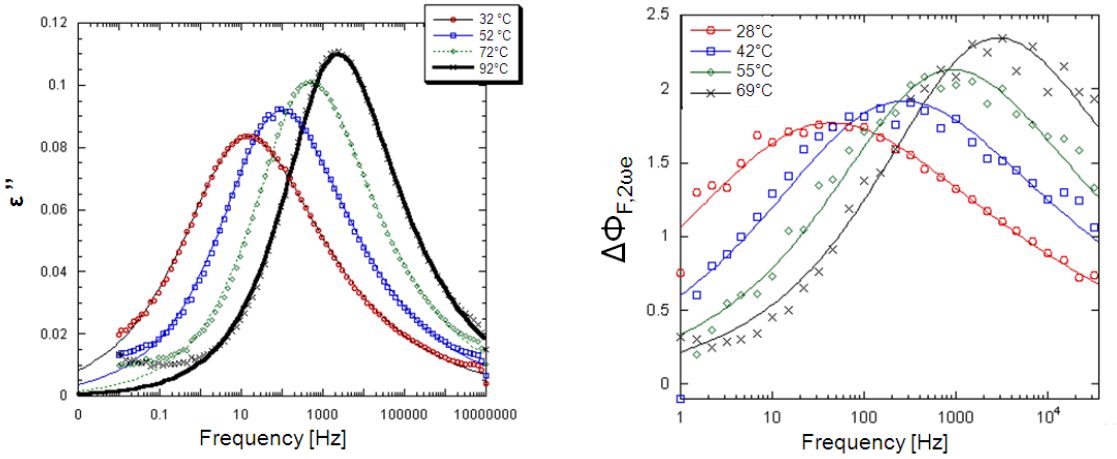

(a) *β-relaxation of PMMA measured by BDS* **(b)** *β-relaxation of PMMA measured by LDS*

Figure 5.14 : *β-relaxation of PMMA measured by BDS and LDS. The increase in the maximum intensity of the relaxation with temperature is detected by both methods.*

— Influence of the thickness and tip sample distance on $\Delta\Phi_{F,2\omega e}$

We will now study the effect of the different parameters on the shape of $\Delta\Phi_{F,2\omega e}$. The first thing is that the measurement is non voltage dependant. Increasing the voltage will induce a stronger deflexion of the cantilever in the force mode and a stronger frequency shift in the gradient mode but it will not affect the difference of phase between these quantities and the electrical oscillation. Fig. 5.15 represents the effect of the thickness of the sample and the lift height (i.e. the lift input in the electronic) on the shape of $\Delta\Phi_{F,2\omega e}$. Measurements have been realized on PVAc samples at 48°C. As mentioned in the section about the Equivalent Charge Method of the Chapter 2, when the thickness decreases, the intensity of the interaction is stronger but the sensitivity of the method decreases. This phenomena is attributed to the stronger contribution to the metallic counter-electrode and can be seen in Fig. 5.15a. Therefore the measurements of the relaxation in ultrathin polymer film is very challenging, in this particular experimental condition we have not been able to measure the relaxation in 70nm thin polymer film. For a fixed thickness, we found that when we are close to the sample the near surface of the sample is strongly polarized leading to high value of the maximum of the relaxation. While increasing the lift height (i.e. the tip-sample distance) the sample is less polarized and therefore the relative

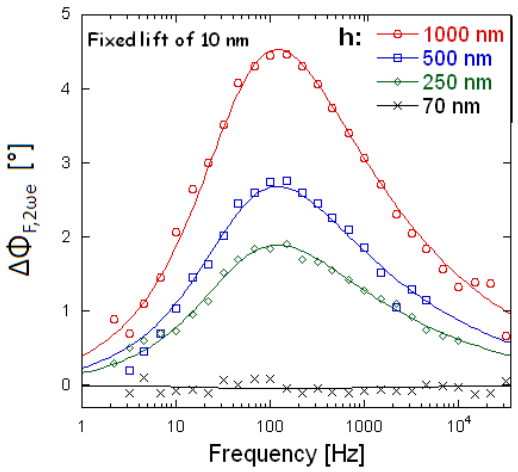

(a) *Effect of the thickness on the shape of* $\Delta\Phi_{F,2\omega e}$*. The intensity of the losses increases with the thickness.*

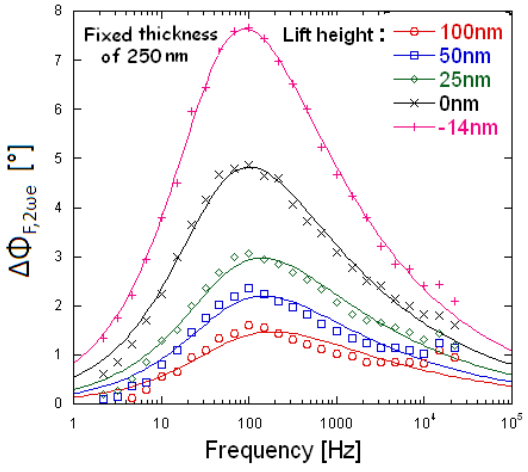

(b) *Effect of the lift height on the shape of* $\Delta\Phi_{F,2\omega e}$*. The intensity of the losses decreases with the lift.*

Figure 5.15

intensity of the dielectric losses decreases Fig. (5.15a). Best working conditions are close to a thick sample. Work toward an absolute quantification is in progress.

Conclusion on the temperature frequency dependence

We have developed two methods to measure locally the frequency dependance of the dielectric permittivity. The first permits to measure the frequency spectrum of the dielectric losses whereas the second allows a mapping of these losses at a given frequency. These two methods can either be achieved by measuring the phase shift in the $2\omega_e$ electrical component of the force or the force gradient. Table 5.2 summarizes the experimental spatial resolution and high frequency limit reached using these two methods. Theoretically, the spatial resolution in the force mode is only slightly higher than the one obtained in the gradient mode. In order to get a proper comparison, measurements should be made with the very same experimental conditions.

	Spatial resolution (nm)	High frequency limit (Hz)
Gradient	40	1e2
Force	150	1e4

Table 5.2 : *Comparison of the spatial resolution and high frequency limit measured experimentally for the force and force gradient mode*

These methods have been used to measure the α-relaxation of PVAc at the nanoscale. Measurements of the frequency spectrum by LDS have shown a faster local dynamics. This phenomena could be related to a decrease in T_g due the influence of the free interface [11,96–98]. *A contrario* to macroscopic measurements, no differences have been found between the dynamics measured by LDS in an island of PVAc surrounded by a matrix of PS and in a pure PVAc sample. This results indicates that our measurement is local and that the matrix of PS does not affect the dynamics of PVAc at the center of the island. Further research are needed to clearly states about interface's effects.

Measurements have not yet been quantified in term of dielectric permittivity but first experiments performed on PMMA shown that LDS permits to measure a relative variation of $\Delta\Phi_{2\omega e}$. Best experimental conditions maximizing the value of the $\Delta\Phi_{2\omega e}$ are a thick sample and a small tip-sample distance.

An important point has been to implement these measurement in the AM mode, under ambient condition, with a non-modified commercial AFM. This simple setup would allow working with bio-materials opening the way of the the study of soft hydrated materials such as proteins, and cell membranes, and investigate processes such as membrane potential formation, action potential propagation, or ion membrane transport [99].

Recent studies [96] have shown that the T_g dynamics (measured by fluorescence) of PS nanolayers and nanodomains can be dramatically tuned (and even slaved) by the dynamics of neighboring immiscible polymers. By using different polymer underlayers, the T_gs of ultrathin PS surface layers span a 100 K temperature range, with related effects occurring in nanoblends. These results show that the cooperative glass transition dynamics in nanoconfined polymer can be coupled to the dynamics of neighboring immiscible polymer domains over many tens of nanometer length scales. Measuring this coupled dynamics using LDS would be of the upmost interest.

Conclusion

The aim of this work was to study dielectric and mechanical properties of polymers at macro and nanoscale. We have chosen to study the relaxations of two polymers: Polyisoprene (PI) and Poly(vynil acetate) (PVAc).

Due to dipolar moment parallel to the chain backbone, PI exhibit a whole chain dielectric relaxation. This so-called normal mode can either be described by the Rouse or reptational tube theory for unantengled and entangled polymers respectively. We have chosen to work with PI samples having a molecular weight variating between 1 and 320 kg/mol in order to cover the range of applications of these two regimes. The first step of the work on PI was to study the Rouse model, well known since the fifties to describe rather correctly the whole chain dynamics of polymers in solution in a theta-solvent. Using rheology, we have measured the molecular weight of entanglement M_e=9 kg/mol and chosen to study how the Rouse model could describe the normal mode response of a sample having a molecular weight of 2700 g/mol. Even if the Rouse model has been intensively investigated by different experimental techniques this study is still challenging because for unentangled polymer, contributions of the α-relaxation (a fast segmental relaxation related to dipolar component perpendicular to the chain backbone) overlap significantly with the whole chain dynamics. By decorelating the effect of the α-relaxation on the normal mode and introducing polydispersity, we showed that the Rouse model permits a good description of both rheological and Broadband Dielectric Spectroscopy (BDS) data. The small differences between theory and experiment are attributed to a defect of configuration: the sample is composed by 80% of the isomer cis.

Then, we have studied the different regime in the dynamics as a function of molecular weight. In agreement with other rheological data previously reported, we found two crossovers in the molecular weight dependence of the longest relaxation time. The first, around a molecular weight of 6.5 $\pm$ 0.15 kg/mol, corresponds to the end of the Rouse regime. Above the second at 100 $\pm$ 50 kg/mol we find a power law with exponent 3 as predicted by the De Gennes theory. The current sensitivity of the methods developed to measure the local dielectric response by EFM did not allowed measuring the rather weak ($\Delta\epsilon \sim 0.05$) relaxation of PI.

PVAc exhibits strong ($\Delta\epsilon \sim 5$) dielectric losses (related with the segmental relaxation) slightly above room temperature and have been a good candidate to develop EFM based nanocharacterization methods. Using BDS, we have first measured its static value of the dielectric constant at 22°C, ϵ_r=3, and 70°C ϵ_r=8. Then by measuring the dielectric frequency spectrum, we have constated that the response of a blend of PVAc / PS is similar to the one measured in the pure component (indicating a phase separation) but slightly shifted to higher frequencies and broadened. One possible hypothesis to explain this phenomena would be that BDS measure dielectric properties over the all sample, including interface's regions between PVAc and PS having a different dynamics.

We have then developed and implement two EFM based methods to measure and image

quantitatively the relative dielectric constant and the temperature-frequency dependance of dielectric losses.

The first method developed to measure dielectric properties at the nanoscale was based on the measurement of the force gradient between a tip and a grounded polymer while applying a V_{DC} voltage. The numerical simulation of the Equivalent Charge Method permits a quantification of the dielectric constant. The method has first been developed to measure the dielectric constant in one point before being extended to a quantitative mapping of heterogeneous component. Measurements made in one point on PVAc and values obtained from a quantitative mapping of the dielectric constant of a nano-structured PVAc / PS are in good agreement with the one previously measured macroscopically by BDS. The spatial resolution of 40 nm is close to the theoretical limit.

The second methods permit to measure the frequency dependance of polymers. First developed by Crider *et al* [10], Local Dielectric Spectroscopy (LDS) permitted to measure in one point the dielectric losses as a function of the frequency via the detection of the force gradient under Ultra High Vacuum (UHV). We have extended this technique to map the dielectric losses at a given frequency. We have demonstrate that LDS could be achieved under ambient condition and by detecting the force between the tip and the sample. Measurements of the frequency spectrum showed that the α-relaxation of PVAc measured locally at the free surface by LDS is faster than the one measured in bulk by BDS. This phenomena could be related to a decrease in T_g due the influence of the free interface [11, 96–98]. *A contrario* to macroscopic measurements, no differences have been found between the dynamics measured by LDS in an island of PVAc surrounded by a matrix of PS and in a pure PVAc sample. This results indicates that our measurement is local and that the matrix of PS does not interferes with the dynamics of PVAc at the center of the island. Further research to unambiguously state about the interface's effects on polymer dynamics would be of the upmost interest. As mentioned few years ago by Pierre-Gilles de Gennes [100], further experiments should not aim at the determination of a single T_g, but at a distribution of T_gs. Concrete other applications of this method would be the study of bio-materials or coupled polymer dynamics in nano-domains [96].

Bibliography

[1] G. Binnig, C. F. Quate and C. Gerber: "Atomic force microscope" *Physical Review Letters* 56(9) p. 930 (**1986**).

[2] C. Rivetti, M. Guthold and C. Bustamante: "Wrapping of dna around the e.coli rna polymerase open promoter complex" *EMBO J* 18(16) p. 4464–4475 (**1999**).

[3] Y. Sugimoto, P. Pou, M. Abe, P. Jelinek, R. Perez, S. Morita and O. Custance: "Chemical identification of individual surface atoms by atomic force microscopy" *Nature* 446(7131) p. 64–67 (**2007**).

[4] O. Custance, R. Perez and S. Morita: "Atomic force microscopy as a tool for atom manipulation" *Nat Nano* 4(12) p. 803–810 (**2009**).

[5] C. Riedel, A. Alegria, P. Tordjeman and J. Colmenero: "Rouse-model-based description of the dielectric relaxation of nonentangled linear 1,4-cis-polyisoprene" *Macromolecules* 42(21) p. 8492–8499 (**2009**).

[6] C. Riedel, A. Alegria, P. Tordjeman and J. Colmenero: "High and low molecular weight crossovers in the longest relaxation time dependence of linear cis-1,4 polyisoprene by dielectric relaxations" *Rheologica Acta* 49(5) p. 507–512 (**2010**).

[7] C. Riedel, R. Arinero, P. Tordjeman, M. Ramonda, G. Leveque, G. A. Schwartz, D. G. de Oteyza, A. Alegria and J. Colmenero: "Dielectric properties of thin insulating layers measured by electrostatic force microscopy" *Eur. Phys. J. Appl. Phys.* 50(1) p. 10501 (**2010**).

[8] C. Riedel, R. Arinero, T. Ph, M. Ramonda, G. Leveque, G. A. Schwartz, D. G. d. Oteyza, A. Alegria and J. Colmenero: "Determination of the nanoscale dielectric constant by means of a double pass method using electrostatic force microscopy" *Journal of Applied Physics* 106(2) p. 024315 (**2009**).

[9] C. Riedel, R. Arinero, P. Tordjeman, G. Leveque, G. A. Schwartz, A. Alegria and J. Colmenero: "Nanodielectric mapping of a model polystyrene-poly(vinyl acetate) blend by electrostatic force microscopy" *Physical Review E* 81(1) p. 010801 (**2010**).

[10] P. S. Crider, M. R. Majewski, Z. Jingyun, H. Oukris and N. E. Israeloff: "Local dielectric spectroscopy of polymer films" *Applied Physics Letters* 91(1) p. 013102 (**2007**).

[11] P. S. Crider, M. R. Majewski, Z. Jingyun, H. Oukris and N. E. Israeloff: "Local dielectric spectroscopy of near-surface glassy polymer dynamics" *The Journal of Chemical Physics* 128(4) p. 044908 (**2008**).

[12] C. Riedel, R. Sweeney, N. E. Israeloff, R. Arinero, G. A. Schwartz, A. Alegria, T. Ph and J. Colmenero: "Imaging dielectric relaxation in nanostructured polymers by frequency modulation electrostatic force microscopy" *Applied Physics Letters* 96(21) p. 213110 (**2010**).

[13] M. Rubinstein and R. H. Colby: *Polymer Physics* (Oxford University, New York, **2003**).

[14] D. Richter, M.Monkenbusch, A. Arbe and J. Colmenero: *Neutron Spin Echo in Polymer Systems* (Springer, Berlin, **2005**).

[15] P. G. de Gennes: *Scaling Concepts in Polymer Physics* (Cornell University Press, Ithaca and London, **1979**).

[16] M. Doi and S. F. Edwards: *The theory of polymer dynamics* (Clarendon, Oxford, **1988**).

[17] P. E. Rouse: "A theory for the linear elasticity properties of dilute solutions of coiling polymers" *The Journal of Chemical Physics* 21(7) (**1953**).

[18] J. Padding: *Computer Simulation of Entanglements in Viscoelastic Polymer Melts* Phd Thesis, (**2003**).

[19] T. C. B. McLeish: "Tube theory of entangled polymer dynamics" *Advances in Physics* 51(6) p. 1379 (**2002**).

[20] J. L. Viovy, M. Rubinstein and R. H. Colby: "Constraint release in polymer melts: tube reorganization versus tube dilation" *Macromolecules* 24(12) p. 3587–3596 (**2002**).

[21] J. D. Ferry: *Viscoelastic Properties of Polymers* (Oxford University Press, New York, **1995**).

[22] N. McCrum, E. Read and G. Williams: *Anelastic and Dielectric Effects in Polymeric Solids* (Wiley, London, **1967**).

[23] F. Kohlrausch: *Pogg. Ann. Phys.* 119(352) p. 7306 (**1863**).

[24] G. Williams and D. C. Watts: *Trans. Faraday Soc.* 66(80) (**1970**).

[25] F. Kremer and A. Schonals: *Broadband Dielectric Spectroscopy* (Springer, Berlin, **2003**).

[26] S. Havriliak and S. Negami: "A complex plane representation of dielectric and mechanical relaxation processes in some polymers" *Polymer* 8 p. 161–210 (**1967**).

[27] T. Madhusudan, A. Angel and C. Juan: "Heterogeneous dynamics of poly(vinyl acetate) far above t[sub g]: A combined study by dielectric spectroscopy and quasielastic neutron scattering" *The Journal of Chemical Physics* 122(24) p. 244909 (**2005**).

[28] H. Vogel: *Phys Z* 22 p. 645 (**1921**).

[29] G. Fulcher: *Journal of American Society* 8(339) (**1925**).

[30] M. L. Williams, R. F. Landel and J. D. Ferry: "Mechanical properties of substances of high molecular weight in amorphous polymers and other glass-forming liquids" *Journal of American Chemical Society* 77(19) p. 3701–3707 (**1995**).

[31] W. Stockmayer: "Dielectric disperson in solutions of flexible polymers" *Pure Applied Chemesitry* p. 539 (**1967**).

[32] "Ta instrument dsc q series manual" *http://www.tainstruments.com/dsc* .

[33] K. Xi and S. Krause: "Droplet deformation and structure formation in two-phase polymer/polymer/toluene mixtures in an electric field" *Macromolecules* 31(12) p. 3974–3984 (**1998**).

[34] M. M. Kumali: *Master thesis' report: Electrostatic force microscopy based approach to study the local dielectric permittivity of polymeric materials* (**2010**).

[35] D. Cangialosi, A. Alegria and J. Colmenero: "Route to calculate the length scale for the glass transition in polymers" *Physical Review E* 76(1) p. 011514 (**2007**).

[36] T. Inoue, T. Uematsu and K. Osaki: "The significance of the rouse segment: Its concentration dependence" *Macromolecules* 35(3) p. 820–826 (**2002**).

[37] I. Yasuo, A. Keiichiro and K. Tadao: "Further investigation of the dielectric normal mode process in undiluted cis-polyisoprene with narrow distribution of molecular weight" *The Journal of Chemical Physics* 89(12) p. 7585–7592 (**1988**).

[38] K. Adachi and Kotak: "Dielectric normal mode relaxation" *Progress in polymer science* 18(3) p. 585 (**1993**).

[39] W. Hiroshi: "Dielectric relaxation of type-a polymers in melts and solutions" *Macromolecular Rapid Communications* 22(3) p. 127–175 (**2001**).

[40] H. Watanabe, Y. Matsumiya and T. Inoue: "Dielectric and viscoelastic relaxation of highly entangled star polyisoprene: Quantitative test of tube dilation model" *Macromolecules* 35(6) p. 2339–2357 (**2002**).

[41] M. Doxastakis, D. N. Theodorou, G. Fytas, F. Kremer, R. Faller, F. Muller-Plathe and N. Hadjichristidis: "Chain and local dynamics of polyisoprene as probed by experiments and computer simulations" *The Journal of Chemical Physics* 119(13) p. 6883–6894 (**2003**).

[42] H. Watanabe, T. Sawada and Y. Matsumiya: "Constraint release in star/star blends and partial tube dilation in monodisperse star systems" *Macromolecules* 39(7) p. 2553–2561.

[43] A. E. Likhtman and T. C. B. McLeish: "Quantitative theory for linear dynamics of linear entangled polymers" *Macromolecules* 35(16) p. 6332–6343 (**2002**).

[44] L. J. Fetters, D. J. Lohse, D. Richter, T. A. Witten and A. Zirkel: "Connection between polymer molecular weight, density, chain dimensions, and melt viscoelastic properties" *Macromolecules* 27(17) p. 4639–4647 (**1994**).

[45] A. Schoenhals: "Relation between main and normal mode relaxations for polyisoprene studied by dielectric spectroscopy" *Macromolecules* 26(6) p. 1309–1312 (**1993**).

[46] K. Adachi, H. Yoshida, F. Fukui and T. Kotaka: "Comparison of dielectric and viscoelastic relaxation spectra of polyisoprene" *Macromolecules* 23(12) p. 3138–3144 (**1990**).

[47] T. Inoue, T. Uematsu and K. Osaki: "The significance of the rouse segment: Its concentration dependence" *Macromolecules* 35(3) p. 820–826 (**2002**).

[48] T. P. Lodge and T. C. B. McLeish: "Self-concentrations and effective glass transition temperatures in polymer blends" *Macromolecules* 33(14) p. 5278–5284 (**2000**).

[49] M. Brodeck, F. Alvarez, A. Arbe, F. Juranyi, T. Unruh, O. Holderer, J. Colmenero and D. Richter: "Study of the dynamics of poly(ethylene oxide) by combining molecular dynamic simulations and neutron scattering experiments" *The Journal of Chemical Physics* 130(9) p. 094908 (**2009**).

[50] R. Lund, S. Plaza-Garcia, A. Alegria, J. Colmenero, J. Janoski, S. R. Chowdhury and R. P. Quirk: "Polymer dynamics of well-defined, chain-end-functionalized polystyrenes by dielectric spectroscopy" *Macromolecules* 42(22) p. 8875–8881 (**2009**).

[51] D. Richter, M. Monkenbusch, J. Allgeier, A. Arbe, J. Colmenero, B. Farago, Y. C. Bae and R. Faust: "From rouse dynamics to local relaxation: A neutron spin echo study on polyisobutylene melts" *The Journal of Chemical Physics* 111(13) p. 6107–6120 (**1999**).

[52] G. E. Logotheti and D. N. Theodorou: "Segmental and chain dynamics of isotactic polypropylene melts" *Macromolecules* 40(6) p. 2235–2245 (**2007**).

[53] H. Watanabe, H. Yamada and O. Urakawa: "Dielectric relaxation of dipole-inverted cis-polyisoprene solutions" *Macromolecules* 28(19) p. 6443–6453 (**1995**).

[54] M. Abdel-Goad, W. Pyckhout-Hintzen, S. Kahle, J. Allgaier, D. Richter and L. J. Fetters: "Rheological properties of 1,4-polyisoprene over a large molecular weight range" *Macromolecules* 37(21) p. 8135–8144 (**2004**).

[55] D. Boese and F. Kremer: "Molecular dynamics in bulk cis-polyisoprene as studied by dielectric spectroscopy" *Macromolecules* 23(3) p. 829–835 (**1990**).

[56] Y. Ding and A. P. Sokolov: "Breakdown of time temperature superposition principle and universality of chain dynamics in polymers" *Macromolecules* 39(9) p. 3322–3326 (**2006**).

[57] H. Watanabe, Y. Matsumiya and T. Inoue: "Dielectric and viscoelastic relaxation of highly entangled star polyisoprene: Quantitative test of tube dilation model" *Macromolecules* 35(6) p. 2339–2357 (**2002**).

[58] L. Portes, P. Girard, R. Arinero and M. Ramonda: "Force gradient detection under vacuum on the basis of a double pass method" *Review of Scientific Instruments* 77(9) p. 096101 (**2006**).

[59] S. Yongho and J. Wonho: "Atomic force microscopy and spectroscopy" *Reports on Progress in Physics* (1) p. 016101 (**2008**).

[60] R. Garcia and R. Perez: "Dynamic atomic force microscopy methods" *Surface Science Reports* 47(6-8) p. 197–301 (**2002**).

[61] G. Gramse, J. Casuso, J. Toset, L. Fumagalli and G. Gomila: "Quantitative dielectric constant measurement of thin films by dc electrostatic force microscopy" *Nanotechnology* 20(39) p. 395702 (**2009**).

[62] L. Fumagalli, G. Gramse, D. Esteban-Ferrer, M. A. Edwards and G. Gomila: "Quantifying the dielectric constant of thick insulators using electrostatic force microscopy" *Applied Physics Letters* 96(18) p. 183107 (**2010**).

[63] J. Hu, X. D. Xiao, D. F. Ogletree and M. Salmeron: "Imaging the condensation and evaporation of molecularly thin films of water with nanometer resolution" *Science* 268(5208) p. 267–269 (**1995**).

[64] H. Huang Wen, A. M. Baro and J. J. Saenz: "Electrostatic and contact forces in force microscopy" *Proceedings of the 5th ICSTMS* 9 p. 1323–1328 (**2001**).

[65] B. D. Terris, J. E. Stern, D. Rugar and H. J. Mamin: "Contact electrification using force microscopy" *Physical Review Letters* 63(24) p. 2669 (**1989**).

[66] P. Li-Hong, E. S. Thomas, J. P. Vallorie, H. C. Paul and M. M. Nicholas: "Three-dimensional electrostatic potential, and potential-energy barrier, near a tip-base junction" *Applied Physics Letters* 65(17) p. 2151–2153 (**1994**).

[67] S. Hudlet, M. S. Jean, C. Guthmann and J. Berger: "Evaluation of the capacitive force between an atomic force microscopy tip and a metallic surface" *The European Physical Journal B - Condensed Matter and Complex Systems* 2(1) (**1998**).

[68] J. Colchero, A. Gil and A. M. Baro: "Resolution enhancement and improved data interpretation in electrostatic force microscopy" *Physical Review B* 64(24) p. 245403 (**2001**).

[69] L. Fumagalli, G. Ferrari, M. Sampietro, I. Casuso, E. Mart, nez, J. Samitier and G. Gomila: "Nanoscale capacitance imaging with attofarad resolution using ac current sensing atomic force microscopy" *Nanotechnology* (18) p. 4581 (**2006**).

[70] G. Gomila, J. Toset and L. Fumagalli: "Nanoscale capacitance microscopy of thin dielectric films" *Journal of Applied Physics* 104(2) p. 024315 (**2008**).

[71] S. Belaidi, F. Lebon, P. Girard, G. Leveque and S. Pagano: "Finite element simulations of the resolution in electrostatic force microscopy" *Applied Physics A: Materials Science and Processing* 66(0) p. S239–S243 (**1998**).

[72] Z. Li, B. Gu and G. Yang: "Scanning-electrostatic-force microscopy: Self-consistent method for mesoscopic surface structures" *Physical Review B* 57(15) p. 9225 (**1998**).

[73] E. Strassburg, A. Boag and Y. Rosenwaks: "Reconstruction of electrostatic force microscopy images" *Review of Scientific Instruments* 76(8) p. 083705–5 (**2005**).

[74] S. Belaidi, P. Girard and G. Leveque: "Electrostatic forces acting on the tip in atomic force microscopy: Modelization and comparison with analytic expressions" *Journal of Applied Physics* 81(3) p. 1023–1030 (**1997**).

[75] G. M. Sacha, E. Sahagun and J. J. Saenz: "A method for calculating capacitances and electrostatic forces in atomic force microscopy" *Journal of Applied Physics* 101(2) p. 024310 (**2007**).

[76] E. Durand: *Electrostatique, tomes III* (Masson, **1966**).

[77] S. Gomez-Monivas, L. S. Froufe-Perez, A. J. Caamano and J. J. Saenz: "Electrostatic forces between sharp tips and metallic and dielectric samples" *Applied Physics Letters* 79(24) p. 4048–4050 (**2001**).

[78] B. Bhushan and H. Fuchs: *Applied Scanning Probe Methods II* (Springer, New York, **2003**).

[79] A. Serghei, M. Tress and F. Kremer: "Confinement effects on the relaxation time distribution of the dynamic glass transition in ultrathin polymer films" *Macromolecules* 39(26) p. 9385–9387 (**2006**).

[80] S. Napolitano, V. Lupascu and M. Wubbenhorst: "Temperature dependence of the deviations from bulk behavior in ultrathin polymer films" *Macromolecules* 41(4) p. 1061–1063 (**2008**).

[81] C. B. Roth, K. L. McNerny, W. F. Jager and J. M. Torkelson: "Eliminating the enhanced mobility at the free surface of polystyrene: Fluorescence studies of the glass transition temperature in thin bilayer films of immiscible polymers" *Macromolecules* 40(7) p. 2568–2574 (**2007**).

[82] C. B. Roth and J. M. Torkelson: "Selectively probing the glass transition temperature in multilayer polymer films: Equivalence of block copolymers and multilayer films of different homopolymers" *Macromolecules* 40(9) p. 3328–3336 (**2007**).

[83] S. Olivier, C. Pascal, H. Frederic and M. Rene: "Capacitance measurements on small parallel plate capacitors using nanoscale impedance microscopy" *Applied Physics Letters* 90(4) p. 043116 (**2007**).

[84] H. Frederic, C. Pascal, S. Olivier, M. Rene and B. Lionel: "Simultaneous resistance and capacitance cartography by conducting probe atomic force microscopy in contact mode" *Applied Physics Letters* 86(12) p. 123103 (**2005**).

[85] L. Fumagalli, G. Ferrari, M. Sampietro and G. Gomila: "Dielectric-constant measurement of thin insulating films at low frequency by nanoscale capacitance microscopy" *Applied Physics Letters* 91(24) p. 243110 (**2007**).

[86] C. Ignacio, F. Laura, G. Gabriel and P. Esteve: "Nondestructive thickness measurement of biological layers at the nanoscale by simultaneous topography and capacitance imaging" *Applied Physics Letters* 91(6) p. 063111 (**2007**).

[87] L. Fumagalli, G. Ferrari, M. Sampietro and G. Gomila: "Quantitative nanoscale dielectric microscopy of single-layer supported biomembranes" *Nano Letters* 9(4) p. 1604–1608 (**2009**).

[88] H. Jun, X. Xu-Dong and S. Miquel: "Scanning polarization force microscopy: A technique for imaging liquids and weakly adsorbed layers" *Applied Physics Letters* 67(4) p. 476–478 (**1995**).

[89] A. V. Krayev and R. V. Talroze: "Electric force microscopy of dielectric heterogeneous polymer blends" *Polymer* 45(24) p. 8195–8200 (**2004**).

[90] A. V. Krayev, G. A. Shandryuk, L. N. Grigorov and R. V. Talroze: "Quantitative analysis of dielectric constants from efm images of multicomponent polymer blends" *Macromolecular Chemistry and Physics* 207(11) p. 966–969 (**2006**).

[91] L. Massimiliano, P. Daniele, N. Kim Hung, C. Simone, L. Mauro and R. Pierangelo: "Local dielectric spectroscopy of nanocomposite materials interfaces" 28 p. C4D11–C4D17 (**2010**).

[92] L. H. Jeffrey and B. John: "Calibration of atomic-force microscope tips" *Review of Scientific Instruments* 64(7) p. 1868–1873 (**1993**).

[93] D. Hall, P. Underhill and J. Torkelson: "Spin coating of thin and ultrathin polymer films" *Polymer Engineering and Science* 38(12) p. 2039–2045 (**1998**).

[94] G. A. Schwartz, J. Colmenero and A. Alegria: "Dielectric study of the segmental relaxation of low and high molecular weight polystyrenes under hydrostatic pressure" *Journal of Non-Crystalline Solids* 353(47-51) p. 4298–4302 (**2007**).

[95] I. Horcas, R. Fernandez, J. M. Gomez-Rodriguez, J. Colchero, J. Gomez-Herrero and A. M. Baro: "Wsxm: A software for scanning probe microscopy and a tool for nanotechnology" *Review of Scientific Instruments* 78(1) p. 013705.

[96] S. Kim, K. Roth, R. Priestley, R. Sandoval, M. Mok, L. Broadbelt and J. Torkelson: "Tuning the glass transition temperature by 100 k in nanostructured heterogeneous polymers" *Submitted in science* (**2010**).

[97] K. Kawashima, R. Inoue, T. Kanaya, K. Matsuba, G Nishida and M. Hino: "Distribution of glass transition temperature tg in a polymer thin film by neutron reflectivity" *Journal of Physics: Conference Series* 184 p. 012004 (**2009**).

[98] J. A. Forrest, K. Dalnoki-Veress, J. R. Stevens and J. R. Dutcher: "Effect of free surfaces on the glass transition temperature of thin polymer films" *Physical Review Letters* 77(10) p. 2002 (**1996**).

[99] J. Malmivuo and J. R. Plonsey: *Biolectromagnetism: Principles and Applications of Bioelectric and Biomagnetic Field* (John Wiley, New York, **1980**).

[100] P. G. d. Gennes: "Glass transitions in thin polymer films" *Eur. Phys. J. E* 2(3) p. 201–205 (**2000**).

List of figures

Dielectric and mechanical properties of polymers at macro and nanoscale.

Abstract: The idea was first to understand the physical theories that describe the dynamics of linear polymers at the macroscopic scale. Rouse and the reptational tube theory describe the large scale dynamics of unentangled and entangled polymers respectively. Using Broadband Dielectric Spectroscopy (BDS) and rheology we have studied the different transition between these two regimes. Avoiding the segmental relaxation contribution and introducing a distribution in the molecular weight we have been able to perform a detailed comparison of the Rouse model with dielectric and rheological data. Effects of entanglement on dielectric spectra have been discussed. BDS and rheology are commonly used techniques to measure dielectric and mechanical properties but they do not have spatial resolution. Therefore the study of the local dynamics or heterogeneous system is always model dependant. We have developed EFM-based methods in order to study this local dynamics. Using the numerical simulation of the Equivalent Charge Method, the value of the static dielectric permittivity has been quantified from the measurement of the force gradient created by a Vdc potential between a tip and a grounded dielectric. This method allows a quantitative mapping of dielectric properties with a 40 nm spatial resolution and is therefore suitable for the study of nano-defined domains. The electrical phase shift in the 2ω component of the force gradient created by Vac voltage is related with dielectric losses. We have developed a method to image the temperature-frequency dependence of the dielectric losses. These methods would allow the study of soft matter or biological phenomena at the local scale.

Key words : Polymer, Soft matter, Dielectric, Mechanical, Dynamics, Rouse, De Gennes, Entanglement, AFM, EFM.

Propriétés diélectrique et mécanique des polymères aux échelles macro et nanoscopique.

Résumé : Le but de cette thèse était tout d'abord d'étudier les théories physiques qui décrivent la dynamique des polymères à l'échelle macroscopique. Le modèle de Rouse et la théorie d'enchevêtrement de P-G. de Gennes décrivent la dynamique des polymères non enchevêtrés et enchevêtrés, respectivement. Nous avons étudié les différentes transitions entre ces deux régimes en utilisant deux techniques expérimentales : Spéctroscopie dielectrique large bande et rhéologie. Un test complet du modèle de Rouse à été effectué en comparant les prédictions de ce modèle pour la dépendance en fréquence de la permittivité diélectrique et du module de cisaillement aux données expérimentales. Les effets d'enchevêtrement sur les spectres diélectriques ont été discutés. Nous avons ensuite développés des méthodes basées sur la microscopie à force électrostatique afin d'étudier les propriétés diélectriques locales. En utilisant une simulation numérique basée sur la Méthode des Charges Equivalentes, nous avons quantifié la constante diélectrique à partir de la mesure du gradient de force crée par un potentiel statique entre une pointe et un diélectrique. Cette méthode permet d'imager la constante diélectrique avec une résolution spatial de 40 nm. Le retard de phase de la composante en 2ω de la force ou du gradient de force crée par un voltage alternatif est relié aux pertes diélectriques. Nous avons développé un mode d'imagerie des pertes diélectriques. Cette méthode simple pourrait être appliqué en biologie ou matière molle en générale afin d'étudier des variations locales de constantes dielectriques.

Mots clés : Polymère, Matière molle, Diélectrique, Mécanique, Dynamique, Rouse, De Gennes, Enchevêtrement, AFM, EFM.

Clément Riedel

Institut d'Électronique du Sud, UMR 5214
Université Montpellier 2 – CC082, Place Eugène Bataillon, 34095 Montpellier Cedex 5

Donostia Internationl Physics Center
UPV / EHU – Paseo Manuel de Lardizabal, 4, 20018 Donostia - San Sebastian, Spain